This is to certify that the
dissertation entitled

EARLY EVENTS IN PROTEIN FOLDING
INVESTIGATED THROUGH
ULTRARAPID MICROFLUIDIC MIXING

presented by

Steven Andrew Waldauer

has been accepted towards fulfillment
of the requirements for the

Ph.D. degree in Physics and Astronomy

Major Professor's Signature

12/21/09

Date

ABSTRACT

EARLY EVENTS IN PROTEIN FOLDING
INVESTIGATED THROUGH ULTRARAPID MICROFLUIDIC MIXING

By

Steven Andrew Waldauer

How a protein folds from a random coil to its native state is one of the most fundamental questions in biophysics. By observing the earliest folding events, it may be possible to gain a better understanding of the entire folding trajectory. Until recently, there has been a gap between the longest possible folding simulations and the earliest possible experimental measurement due to an inherent unobservable dead time. We present an ultrarapid microfluidic mixer with no unobservable dead time and a mixing time more than 500 times shorter than the dead time of the previous state of the art instrument.

We investigated the earliest events in the folding of protein L, and found complexity in a process originally thought to be a simple two-state folder. The experiments performed in a UV fluorescence ultrarapid microfluidic mixer uncovered early kinetics including a 4 μs rise and 43 μs decay in overall tryptophan fluorescence that were entirely within the dead time of earlier stopped-flow experiments.

We measured the time evolution of the diffusion-limited rate of unfolded protein L less than 300 μs after being allowed to start to refold. Using this rate along with a new distance probability distribution produced through hundreds of thousands of MD simulations, we found the intramolecular diffusion coefficient decreases by an astounding 550 fold from when the protein is fully denatured to when it is in folding conditions.

To my parents, Marcy and Marc

ACKNOWLEDGMENTS

I would like to thank my advisor, Lisa Lapidus, for her guidance and patience over the last three years. Her enthusiasm for experimental biophysics is contagious. I am especially grateful for the opportunity she has given me to work on such an ambitious project.

I would not have been able to accomplish any of these projects without the assistance of Terry Ball, who has produced almost all of the protein samples I've measured. His expertise in mutagenesis, protein expression and purification, and what at times seem to be virtually all other aspects of biochemistry, is incredible.

None of the microfabrication would have been possible without the seemingly limitless support of Avinash Kane, Shuhuai Yao and Olgica Bakajin at Lawrence Livermore National Lab, Tom Lee and Joe Zendejas at the UCLA Nanolab, Baokang Bi here at MSU and countless others at each of those facilities.

I would like to thank my entire extended family and especially my Mom and Dad, and my brothers, Jonathan and Alex. Your support and encouragement has made this whole thing possible. Also Cary, Denise, Callie and Casey for their generous hospitality.

Thanks also to:

The members of my group, Stephen, Yujie, Vijay, Eric, Mike, Li, Terry and Lisa (again). Thank you for your help and friendship and for making our lab a fun place to do research.

Tom Palazzolo and the rest of the guys in the machine shop. Your exemplary craftsmanship made my work much easier. I am always in awe of what you guys can do.

Lastly, all of the good friends I have made out here at Michigan State University.

TABLE OF CONTENTS

LIST OF TABLES

LIST OF FIGURES

Images in this dissertation are presented in color.

1. Introduction

1.1 Protein Folding

Proteins are a family of biological macromolecules. They are long polymer chains made of amino acids and each protein has a unique 3D structure and function determined by its amino acid sequence. Proteins are responsible for the vast majority of physiological processes, such as catalyzing reactions, providing cellular scaffolding, intra- and intercellular signaling, and locomotion.

The 3D structure of a protein can be determined experimentally through a variety of different experimental methods, the most common being nuclear magnetic resonance (NMR) and X-ray scattering from a protein crystal. These experiments can yield the coordinates of every atom in the protein structure to ≥ 0.25 Å. The all-atom structure of different proteins reveal a series of different elements found in most protein structures. These elements, such as a hairpin bend, alpha helix or beta sheet make up the secondary structure of the protein and the arrangement of these elements make up the tertiary structure.

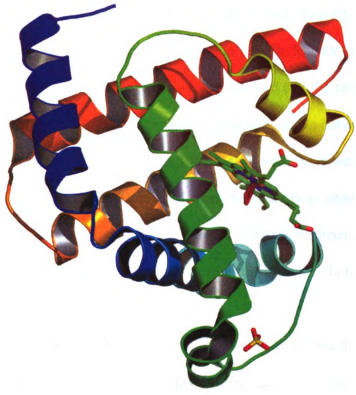

Figure 1.1.1 A cartoon showing the protein structure of Myoglobin, which was the first protein structure determined from X-ray scattering off of a crystallized protein (*1*). The coiled ribbon elements are α-helices. Image is taken from Wikimedia Commons[1], which was made from the structure 1MBO at the Proteins Database (pdb.org).

Proteins are made inside the cell by the ribosome (itself a molecular machine made of proteins and RNA) according to their primary structure, but there is no specialized mechanism to shape the protein into its native conformation. An essential question is how does a protein fold into its native conformation, starting from an unfolded state.

Most proteins fold into their native conformation spontaneously without any assistance from other mechanisms within the cell (although there are mechanisms that

[1] http://upload.wikimedia.org/wikipedia/commons/6/60/Myoglobin.png

assist folding, most of these are passive and generic processes). In early experiments, it was found that it is possible or denature (or unfold), a protein. Mirsky and Anson found as early as 1929 that this process was actually reversible and that the renatured protein was indistinguishable from the original protein (*2*) (the connection between denaturing and folding was made many years later). By 1961 the connection between the structure and function of a protein was well established when Anfinsen et al. observed the refolding of ribonuclease and showed that as the concentration of denaturant decreased, the enzymatic activity as measured against RNA (the substrate for ribonuclease) increased (*3*).

Anfinsen first proposed a thermodynamic explanation, stating that the free energy of the protein is at a minimum when in its native folded state (*4*). However, this does not explain the process of how a protein starting in a random, unfolded conformation is able to fold to its native state. There have been a number of theoretical frameworks seeking to explain the protein folding kinetics process (*5*). These explanations include spin-glass theory (*6*), nucleation-condensation (*7*), folding pathways (*8*), and energy landscapes (*9-14*). None of these theories are exactly predictive and none have yet been able to determine the structure and the folding trajectory for a protein *a priori*, starting in a random conformation based only on the protein sequence. There have been molecular dynamics (MD) simulations that have folded small proteins such as the villin headpiece *ab initio* (*15*) although the folding timescales can be off by three orders of magnitude (*16*).

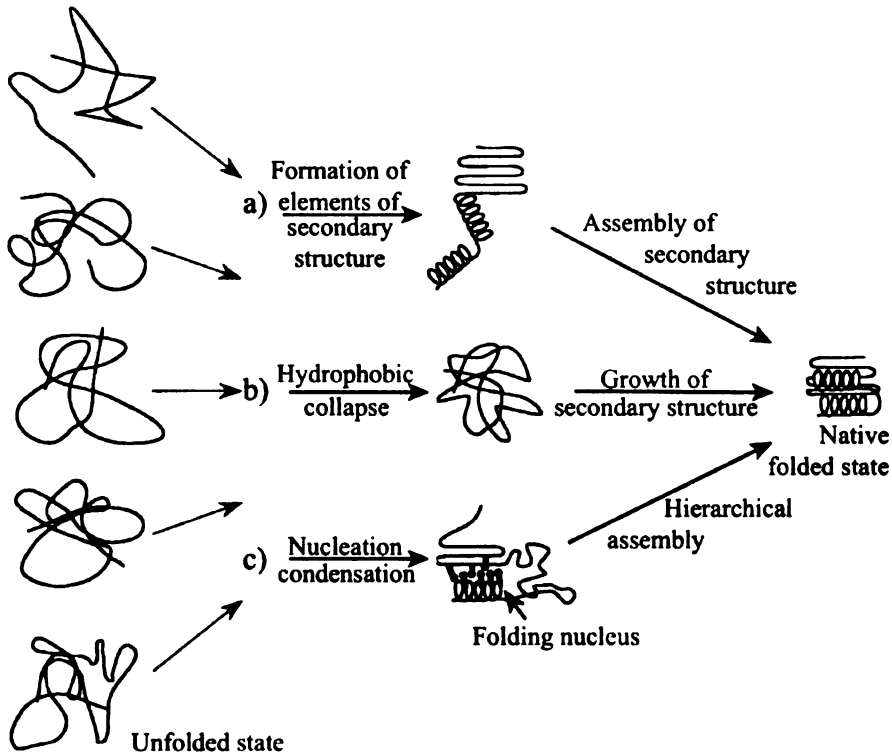

Figure 1.1.2 Three different theoretical protein-folding mechanisms. a) Framework model in which elemental parts of secondary structure form before any tertiary structure, which then pack tightly into the native conformation. b) Hydrophobic collapse framework predicts that the protein will first collapse into a molten globule phase driven by hydrophobic interactions, following which native contacts will form producing the native state. c) Nucleation-condensation predicts that a folding nucleus forms initially and then catalyzes further folding to the native state. Illustration from ref (*17*).

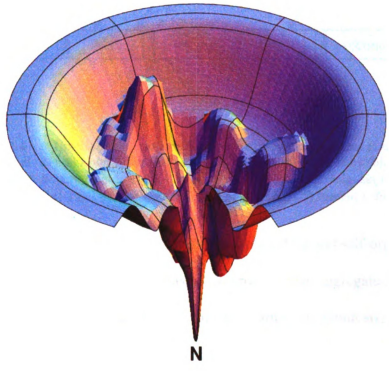

Figure 1.1.3 A folding energy landscape (*10*). At the center of the free energy landscape lies lowest point which represents the native conformation. The radial distance from the center represents an arbitrary reaction coordinate such as the radius of gyration. A protein starts with a random conformation at the far edge of the folding landscape with a high free energy. As the protein folds, it falls inward towards the native state. There are a number of different paths towards the native state. Local minima may temporarily trap the protein and act as intermediate states. Image taken from the Dill group website[2]

Proteins fold over a large range of timescales, from the order of microseconds to hundreds of seconds (*18-20*). This, along with the incredibly large number of free variables, makes finding an encompassing theory to predict how a protein will fold from any given amino-acid sequence difficult. However, even without an all-encompassing theory (which may not be possible), there is much useful information that can be learned from current theory and ongoing simulations and experiments.

---

[2] http://www.dillgroup.ucsf.edu/dl_images/funnel/bumpyBowl.tiff

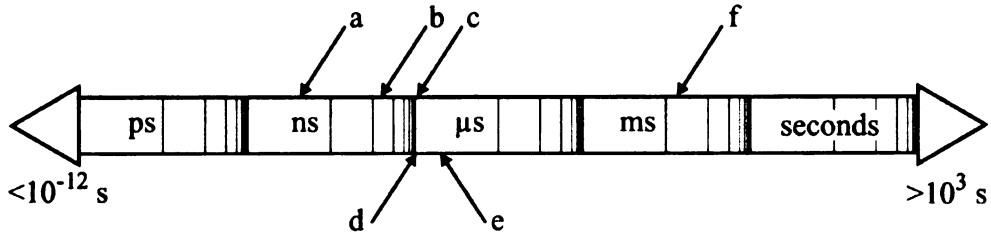

Figure 1.1.4 Timeline comparing different protein folding processes as described in Eaton et al (*21*). a) Loop formation occurs ~ 7 – 90 ns. b) An α-helix folds in 400 – 800 ns. c) A β-hairpin folds in 0.8 – 13 μs. d) A 100 residue protein can fold in no faster than 1 μs. e) The villin headpiece folds in 4.3 μs (*20*). f) Protein L folds in 36 ms (*21*).

Protein folding is one of the most basic examples of natural self-organization. When proteins fail to fold properly, the misfolded proteins may aggregate and cause diseases such as prion disease (e.g. spongiform encephalitis), amyloidosis, Huntington's chorea and Alzheimer's disease (*22*). As the theory and simulations using the growing experimental data improve, it is becoming increasingly likely that scientists will be able to understand and better treat these diseases. One of the consequences of the folding energy landscape theory, as shown in Figure 1.1.3, is that the way a protein folds is path dependant. This makes the earliest folding events very important since they have such a large influence on the path through the landscape that is chosen.

There are a number of probes available for protein folding experiments, such as nuclear magnetic resonance (NMR), small angle X-ray scattering (SAXS) and a variety of different optical measurements. The available probes can be classified into two different categories, local and structural probes, although many of the probes can actually do both. Circular dichroism (CD) is an example of a structural probe. A CD signal can give information on the protein's secondary structure – such as the beta sheet content of a

protein in solution. Likewise, SAXS can give only general information about the protein such as its radius of gyration R_G.

Local probes, on the other hand, yield information about the local environment of a specific region of the protein, often determined through use of a labeled marker. NMR experiments give immense amounts of local information through the use of isotope labeling and NMR can even be used to determine very close to all-atom structural information for small proteins.

It is important to note that in folding kinetics experiments there is an important constraint on the class of available probes: they must be able to measure the system in real time. This means that the time of a particular folding event and the time a measurement is taken after the initiation of folding must be one-to-one. For a folding process, the probe must be able to take fast individual measurements over the course of the entire observation period. This is different from many other types of kinetics experiments where measured observables taken over long timescales can yield information about much faster processes. For example the very fast orientational diffusion time of bulk water (~ 2.3 ps) was originally determined by measuring the much slower NMR T_1 relaxation time (0.45 s), which was known theoretically to have an inverse relationship with the reorientation time (*23, 24*). Because there is no accepted folding framework, or even known assumptions about the folding of almost any protein, it is not possible to infer fast processes, such as the lifetime of a short-lived folding intermediate, from a slower probe measuring longer time observables.

1.2 UV Tryptophan Fluorescence

One of the most effective and fastest probes of protein folding is optical or UV spectroscopy. There are three different naturally occurring photoactive amino acids, tryptophan (Trp/W), tyrosine (Tyr/Y) and phenylalanine (Phe/F). Of the three, the indole group found in tryptophan residues is the dominant source of UV absorbance and emission in proteins. Unfortunately, the vibrational structure of the indole group is far less understood than the electronic structure of benzene derivatives like those found in Phe or Tyr. Although the quantum yield and lifetime of Trp and Tyr are similar, the tyrosine spectrum is only useful to analyze proteins that are free of tryptophan residues. When both tryptophan and tyrosine are present, the tyrosine spectrum will be difficult to observe due to (1) low extinction, (2) substantial quenching, and (3) tyrosine-tryptophan excitation energy transfer (*25*).

Table 1.2.1 Fluorescence parameters of aromatic amino acids in water at neutral pH (*25*)

Species	λ^{em}_{max} (nm)	λ^{ex} (nm)	Band width (nm)	Quantum yield	Lifetime (ns)
Phenylalanine	282	260	-	0.02	6.8
Tyrosine	304	275	34	0.14	3.6
Tryptophan	353	295	60	0.13	3.1 (mean)

Tryptophan is one of the rarer amino acids, naturally occurring in proteins about 1.3 times per 100 residues (*26*). This means that for most small and medium sized proteins there may be zero to three or four tryptophan residues and usually it is possible to mutate the protein such that it contains a single tryptophan, without drastically

changing the folding properties. As such, the fluorescence from a single tryptophan residue can be an effective local probe and can yield significant information in two different ways. First, the tryptophan fluorescence emission spectrum is greatly affected by the solvent exposure of the residue. As a result, a solvent exposed tryptophan, such as one found in an entirely denatured protein, may have a spectrum maximum red-shift of up to 40 – 50 nm in comparison to the same tryptophan buried in the hydrophobic core of a folded protein (*25, 27, 28*).

The overall tryptophan fluorescence intensity is different between a folded and unfolded protein, even for proteins containing multiple tryptophan residues. This makes the overall intensity a second effective way to observe protein folding. However, there is no consistency between different proteins as to whether the folded or unfolded state has higher fluorescence intensity, even when taking into account the location of the tryptophan in the folded protein structure. Lakowicz gives a few different factors to explain the variability of the fluorescence lifetimes and quantum yields in different proteins (*27*). They are:

- quenching by proton transfer from nearby charged amino acids groups,
- quenching by electron acceptors such as protonated carboxyl groups,
- electron transfer quenching by disulfides and amides,
- electron transfer quenching by peptide bonds in the protein backbone, and
- resonance energy transfer among the tryptophan residues.

Because of these effects, the total fluorescence acts more as a general folding probe than as a local probe. It is also therefore standard procedure to measure the fluorescence spectra of the folded and unfolded proteins in equilibrium before any

folding measurements are performed, in order to ascertain whether the overall intensity will increase or decrease during folding.

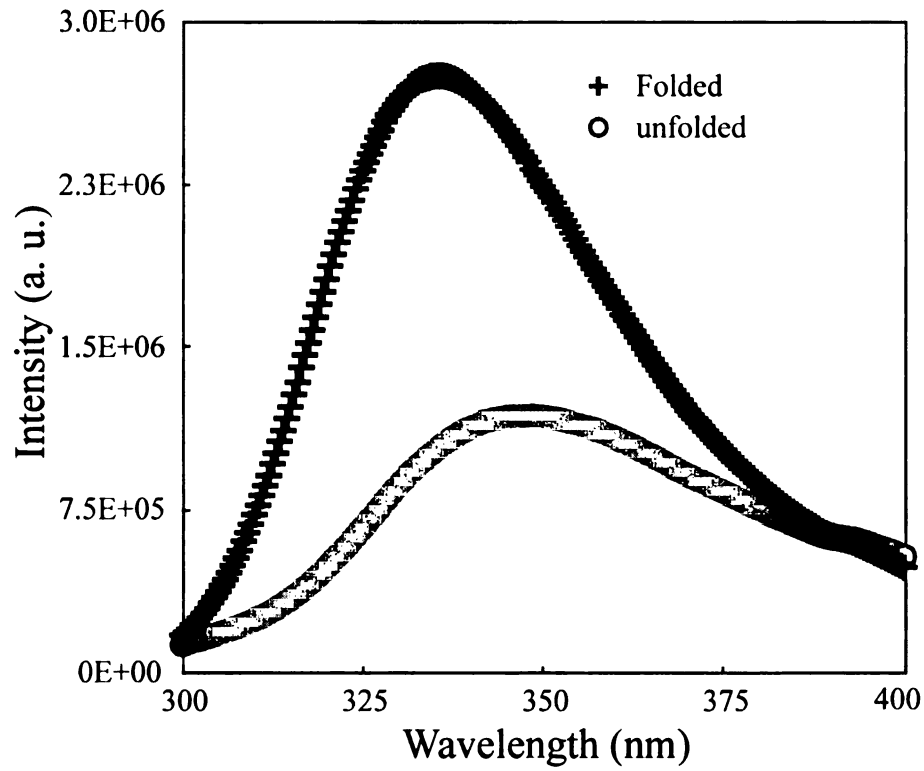

Figure 1.2.1 Fluorescence emission spectra of a single tryptophan mutant of protein L. Note that the overall intensity greatly increases when the protein is folded, and the spectrum is blue shifted because the tryptophan residue becomes hydrophobically buried.

1.3 Tryptophan-Cysteine Contact Quenching

One of the most pertinent processes in protein folding is the formation of native intramolecular contact between residues that are distal in sequence. Lapidus et al. were able to measure the rate of intramolecular contact formation directly using a technique called tryptophan-cysteine contact quenching (*29*). The method utilizes another unique property of tryptophan besides its fluorescence – the relatively long lifetime of its excited triplet state. In the absence of any quenchers, the triplet lifetime can be more than ~ 40

μs. Even more important is that different amino acid residues quench the triplet state differently. The most efficient quencher, by a factor of ~ 400 × greater than all the others (besides tryptophan itself), is a cysteine residue. By placing single tryptophan and cysteine residues on a peptide chain and observing the triplet state it is possible to determine the intramolecular contact rate.

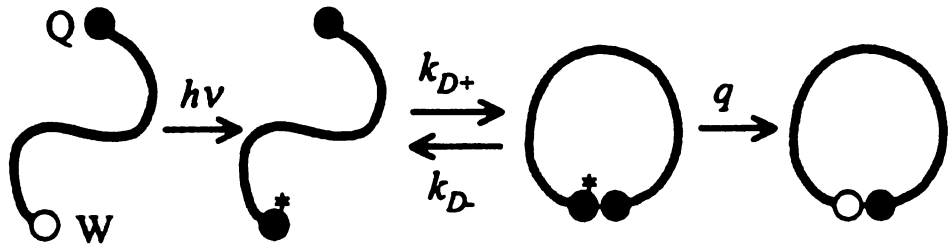

Figure 1.3.1 This cartoon illustrates how to determine the contact rate between two ends of a polypeptide chain. At one end a tryptophan residue (W) is excited to the triplet state. As the peptide diffuses freely, the tryptophan end can come in contact with a cysteine residue (Q) at the other end of the chain. During the interval, when the two ends are in contact, the cysteine may quench the triplet with a total probability dependent on the quenching rate (q), the diffusive pair contact rate (k_{D+}) and the diffusive dissociation rate (k_{D-}) (*29*).

In the simplest case, a peptide is constructed such that there is a tryptophan on one end and a cysteine on the other (as shown in Figure 1.3.1). To obtain the contact rates we consider the quenching to occur in a two-step process: first, through diffusion, the ends must come into close proximity forming a tryptophan-cysteine contact pair; and secondly, the triplet is quenched irreversibly by the cysteine through electron transfer. This can be described by the simple equation:

$$A \underset{k_{D-}}{\overset{k_{D+}}{\rightleftharpoons}} B \xrightarrow{q} C \quad , \tag{1.1}$$

where A, B, and C, are the three different populations and k_{D+} and k_{D-} are the diffusion rates for contact pair production and dissociation and q is the quenching rate for cysteine.

Assuming the population of *B* doesn't change over time, the observed quenching rate for this system can be derived using elementary chemical reaction equations (*30*) as:

$$k_{obs} = q\frac{k_{D+}}{k_{D-} + q}, \qquad (1.2)$$

Lapidus et al. investigated the distance dependence of the contact quenching mechanism in depth by embedding a low concentration of tryptophan in room-temperature trehalose glass containing a high concentration of cysteine (*31*). Since in this system diffusion is almost negligible, it was relatively straightforward to determine the distance dependence of any quenching by determining the tryptophan-cysteine distance distribution from their relative concentrations and the assumption that the molecules are randomly distributed. They found that the cysteine must come within ~ 1 Å of van der Waals contact (4 Å) with the tryptophan for quenching to take place. The quenching rate $q(r)$ falls off as $q_0 \exp[-\beta (r - a_0)]$, where r is the separation and a_0 is the distance of closest approach. They found experimentally that $q_0 = 4.2$ ns^{-1}, $\beta = 4$ Å^{-1}, and $a_0 = 4$ Å.

Equation 1.2 can be rewritten as:

$$\frac{1}{k_{obs}} = \frac{1}{qK} + \frac{1}{k_{D+}} = \frac{1}{k_R(T)} + \frac{1}{k_{D+}(T,\eta)}, \qquad (1.3)$$

where K is defined as k_{D+}/k_{D-}. The reaction-limited rate k_R (qK) corresponds to the situation in which diffusion is fast enough ($k_{D-} \gg q$) that the equilibrium end-to-end distance distribution is maintained at every instance. In this case, the two ends of the chain come into contact and break contact many times before quenching occurs. The diffusion-limited rate k_{D+} ($q \gg k_{D-}$) occurs when the quenching rate is fast enough that

any time the two ends come into contact the triplet is always quenched and the observed rate corresponds directly to the rate for the formation of contact pairs (*32, 33*). Previous studies established that in unstructured peptides, the diffusion and quenching rates are comparable (*29*). Therefore, one can find the reaction-limited rate by plotting $1/k_{obs}$ versus solution viscosity; the y-intercept will be $1/k_R$ and the slope is assumed to be $1/\eta k_{D+}$. Lapidus et al. (*32*) have shown empirically, the rate k_R is modeled as:

$$k_R = k_{R0} \exp\left(\frac{E_0 (T - T_0)}{RTT_0}\right) , \tag{1.4}$$

where T is the absolute temperature and T_0 is 273 K and k_{R0} and E_0 are fitting parameters (*32*).

Assuming k_{D+} is inversely proportional to viscosity but also depends on temperature, it is modeled as:

$$k_{D+} = \frac{k_{D+0} T}{\eta T_0} \exp\left(\gamma (T - T_0)\right) , \tag{1.5}$$

where k_{D+0} and γ are fitting parameters.

Although unphysical, it is possible to derive equation 1.3 exactly without the assumption that the population of Trp-Cys pairs is not increasing or decreasing with time. This assumption is valid because the population of Trp-Cys pairs should have reached equilibrium (as defined by the bidirectional arrows in the original equation) and there is no physical mechanism for this population to act differently from a transient population. In this case, equation 1.3 would be written as:

$$\frac{1}{k_{obs}} = \frac{1}{qK} + \frac{1}{k_{D+}} + \frac{1}{q}. \tag{1.6}$$

And the reaction-limited rate can be rewritten as:

$$k_R = \frac{qK}{1+K}. \tag{1.7}$$

Where k_R is still not dependent on viscosity and in the case where $K \ll 1$, $k_R \approx qK$, which is identical to the definition described earlier.

Szabo, Schulten and Schulten (SSS) Theory

SSS theory assumes intramolecular motion can be modeled as diffusion on a 1D potential that is defined by the equilibrium distribution of pairwise distances, such as the Trp-Cys distance, *r*. The reaction-limited rate is then a convolution of the distance dependent quenching rate $q(r)$, and the distance distribution $P(r)$, such that:

$$k_R = \int_a^\infty q(r)P(r)dr\ , \tag{1.8}$$

where *a* is the closest allowed distance between the Trp and Cys and is typically defined as 4 Å.

The diffusion-limited rate can also be determined through SSS theory using the same distance probability distribution and rate can be written as such (*34*):

$$\frac{1}{k_{D+}} = \int_a^{l_c} (D(x)P(x))^{-1} \left[\int_x^{l_c} P(y)dy\right]^2 dx\ , \tag{1.9}$$

where l_c is the contour length of the chain, which for a polypeptide, l_c = 0.38 nm × number of peptide bonds (*32*). D is the effective diffusion coefficient and is an approximate analytical solution to the 1D diffusion model of Szabo, Schulten, and Schulten in the case where the reaction is distance-dependent. Lapidus et al. tested these equations (1.8 and 1.9) numerically by comparing their values for the reaction-limited and diffusion-limited rates with those calculated directly from the Smoluchowski diffusion equation on a 1D potential (the potential defined as $U(r) = -\ln(P(r)/k_BT)$ using a probability distance distribution for a wormlike chain model. They found the difference between in k_R between the two calculated values to be about 6% and 2 – 12% for k_{D+}. Therefore the only free parameters are D and $P(r)$ and much work has been concentrated on finding physically realistic methods to determine $P(r)$.

Buscaglia et al. have shown that using a wormlike chain model with an excluded volume can produce probability distributions that can be used to calculate theoretical observables that are very close to those measured experimentally (*33*). In this model, the peptide chain is given an intrinsic stiffness, characterized by a persistence length l_p. To include excluded volume effects, each peptide bond location is approximated as a hard sphere with a diameter d_α. To create a distance distribution, millions of chains are created, keeping only the chains in which none of the distances between any two bonds (besides those of the nearest neighbors) exceed d_α and discarding the rest. This is a Monte Carlo sampling method and only approximates general physical phenomena such as solvent effects or any intramolecular interaction such as charge, van der Waals or

hydrophobic effects. By varying both l_p and d_α it is possible to create distance distributions that mimic those of peptide chains found in varying denaturant concentrations.

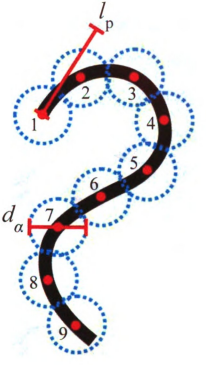

Figure 1.3.2 Schematic of a wormlike chain with excluded volume. The peptide backbone is assumed to have a uniform rigidity, κ, corresponding to a persistence length, $l_p = \kappa/k_BT$. The chain is assumed to have 10 segments per peptide bond (0.36 nm). The excluded volume model assumes that a hard sphere of diameter d_α is present at the end of each peptide bond and conformations in which two bond termini that are not nearest neighbors are closer than d_α are excluded from the simulated ensemble. Since tryptophan- cysteine distances are considered explicitly in calculating the rates, configurations for which the chain distance between these two residues is less than d_α are included. Taken from reference (*33*).

More recently, molecular dynamics (MD) simulations have been used to produce P(*r*) by simulating tens of thousands of motion trajectories, each up to ~ 10 μs long and making many measurements of *r* as the unfolded protein randomly diffuses (*35*).

Trp-Cys Contact Quenching in Protein Folding

Trp-Cys contact quenching is a useful probe for systems much more complex than peptide chains; it was originally shown by Buscaglia et al. (*36*) to be a viable probe of protein folding. For a folding experiment, a tryptophan and cysteine are placed such that they are far enough apart then when the protein is folded there is no possibility of the cysteine quenching the triplet state. However, when the protein is unfolded, the cysteine and tryptophan are free to diffuse and come into contact and quench the triplet state.

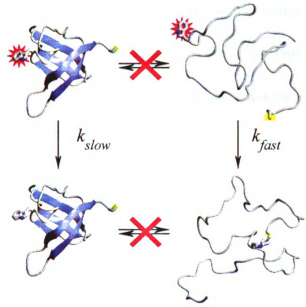

Figure 1.3.3 Schematic illustrating how contact quenching can show protein folding. The top left shows a folded protein with a single tryptophan residue excited to the triplet state and on the top right, an unfolded protein with the same excited tryptophan. Even though there is a single cysteine residue present on the protein, the only avenue for the tryptophan in the folded protein to decay to the ground state is through natural decay processes because the quencher is on the other side of the structure. In contrast, the tryptophan in the unfolded protein, shown on the lower right, can be quenched by the cysteine because it is free to diffuse. These two processes will show as two different decays when measuring the triplet lifetime, with the process on the left being much longer and closer to the natural lifetime of free tryptophan and the process on the right being much faster. Both of these processes are faster than the folding and unfolding processes and there is no exchange between these populations during the lifetime of the triplet state as shown by the red X's. Image is taken from ref (*36*).

When observing the triplet state, it is possible to infer the percentage of the folded and unfolded populations by the relative amplitudes of a fast decay rate, corresponding to quenching caused by the freely diffusive unfolded protein, and a much slower rate corresponding to the fully folded protein. As an added benefit of this type of experiment, it is possible to observe folding intermediates by moving the tryptophan and cysteine residue positions on the protein and observing how the relative rates may change, possibly due to some parts of the protein having greater stability than others for a given concentration of denaturant. Also, since the two rates are sensitive to two different states, with k_{fast} sensitive to the unfolded state and k_{slow} to the folded state, if their relative amplitudes do not show an inverse relation while changing denaturant or folding conditions, it may be evidence of intermediate states.

1.4 Folding Kinetics Experiments

Folding Prompts

Conceptually, the simplest possible protein folding experiment would be to take a single protein molecule and observe it as it transitions between the folded and unfolded states. Of course in order to go from a conceptual experiment to a real one, a few additional concepts are necessary. The first missing component to a folding experiment is a folding prompt.

Almost any environmental variable can be used as a folding prompt. Rapid changes in pH (*37*), pressure (*19*), and temperature (*38*) have all been used as folding prompts. There are optical folding triggers also available such as photo-dissociation (*39*) and photo-switchable peptides (*40*). All of these prompts are limited to one extent or

another to a specific class or individual proteins. For example some proteins unfold reversibly at certain temperatures while others do not. Photo-dissociation can only be used as a prompt for proteins such as cytochrome-c, which is folded only when associated with a heme group. One can unfold a protein through physical manipulation techniques such as laser or magnetic tweezers (*41*) or by the tip of an atomic force microscope (*42*) but these measurements tend to find the folding energy landscape as a function of pulling force and, although they can be very useful in probing a folding pathway, it can be very difficult to measure the time resolved folding kinetics through such methods. These experiments are much more suited to directly measure unfolding and any folding information is usually gained indirectly. They are also far from the physiological conditions found inside the cell. For an experiment that measures time resolved folding kinetics to be feasible, a protein or a large population of proteins must be initiated to go from one state to the other by a rapid environmental change, instigated by means of some sort of folding prompt.

Another important avenue to exploring protein folding is computer simulation. Although it has long been a goal to fold a protein starting from a completely random conformation *ab initio* through computer simulation, this is exceedingly difficult with the current state of computational power. An all-atom simulation using explicit water molecules (hydrophobic interactions are crucial to protein folding) can take many months in order to simulate just a few microseconds of molecular dynamics. For example, Freddolino et al were able to simulate a fast folding protein in a 30,000 atom system using 327 CPU cores at a rate of 100 ns/day (*43*) Using less computationally expensive

techniques, such as implicit solvent or coarse-grain models (*44*), allows simulation of longer times scales as well as making it easier to gain enough data for suitable statistics.

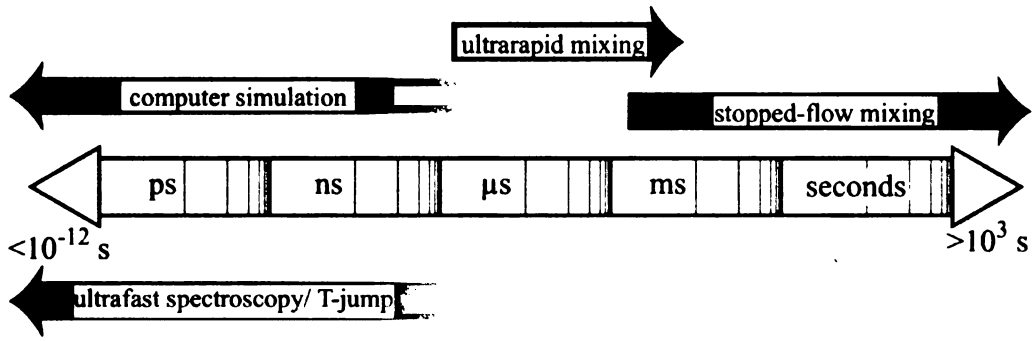

Figure 1.4.1 Timeline comparing the time ranges for different experimental prompts. Computer simulations are generally able to only measure up to microsecond timescales with picosecond or greater resolution. Ultrafast laser spectroscopy can measure up to microseconds with picosecond resolution (*45*). Ultrafast measurements are typically limited by the available experimental prompts such as T-jump, which can only measure protein unfolding, and photophysical triggers, which can be used only with a small subset of available proteins, such as myoglobin or cytochrome-c. Stopped-flow mixing experiments (as described in section 1.4), using a variety of probes such as fluorescence, SAXS or CD can measure folding following a dead time of about 1 ms. Ultrarapid mixers (such as the one described in section 2.1) have a mixing time of ~ 5 – 10 μs and can measure folding up to the first few milliseconds.

The most generic folding prompt available is to use a chemical denaturant such as urea or guanidine hydrochloride (GdnHCl), which will unfold all proteins that are naturally folded in water. It is important that following the prompt, the environment surrounding the protein must reach equilibrium faster than the protein itself. This restriction can cause a great deal of added complexity to a folding experiment.

A typical mixing experiment has a sudden change in the concentration of a chemical denaturant. Usually, the protein starts in solution with a high concentration of denaturant, for example 6 M GdnHCl. At this concentration, very close to 100% of the protein is completely unfolded. The initial solution is then rapidly diluted with a buffer solution containing no denaturant which drops the total denaturant concentration below

the threshold concentration for unfolding, allowing the proteins to begin to refold. As this occurs a fast probe such as UV tryptophan fluorescence observes the protein in solution.

Stopped-flow Mixers

A conventional mixing experiment uses an apparatus called a stopped-flow mixer. The most basic stopped-flow mixer is comprised of only a few parts. There are two syringes, one containing the unfolded protein in solution with denaturant and the other syringe, typically 10 times larger, containing a buffer solution. The syringes are connected together at the mixing chamber and attached to the exit of the mixing chamber is an observation chamber where the protein state is probed.

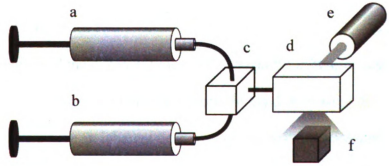

Figure 1.4.2 Diagram showing a stopped flow mixer. The protein in solution with denaturant is held in one syringe (a) and the diluent in the other (b). The two syringes are pressed at the same time forcing the solutions to mix in the mixing chamber (c) and into the observation chamber (d). There the protein can be observed by exciting with a laser (e) and detecting the fluorescence (f).

Stopped-flow measurements are a well-developed technique and there are a number of commercial manufacturers of stopped-flow instruments, able to perform a number of different experiments using a variety of available probes. There are however a number of unavoidable limitations with such an experiment. The most serious of these is the mixing itself. At the molecular length scale, which is the local environment for any protein molecule, all motion and therefore all mixing is diffusively driven and is actually quite slow. The common example given is that if one were to mix cream into coffee with

only diffusive mixing, the coffee would be cold long before the cream was fully mixed. A stopped-flow mixer employs the simplest method to speed up mixing: turbulence. Turbulence divides up a flow into a mass of chaotic eddy currents, each of a very small size, allowing for short diffusion times across eddies.

However, there is a tradeoff in using turbulent mixing in that for a folding kinetics experiment, the protein environment must be in equilibrium for any measurements to be meaningful. Therefore before a measurement is taken, one must wait for any remaining turbulence subsequent to mixing to die down and during that time the system is unobservable. Another similar limitation in some stopped-flow designs is that the mixing and observation chambers are not necessarily the same and more time may be lost as the solution transits between the two.

By adding up all the different times lost between the initiation of folding by mixing and the first measurement one can determine the dead time of the instrument. Stopped-flow mixers have an inherent dead time on the order of milliseconds and even the most advanced device on the market has a dead time only slightly smaller than one millisecond.

Continuous-flow Mixers

It is possible to modify the stopped-flow mixer design by elongating the observation chamber and flowing the solutions continuously at a constant flow-rate. In this mixer, called a continuous-flow mixer, observations taken at different positions along the observation chamber correspond to different times after mixing, with observations further from the mixing region corresponding to later times. In a continuous-flow mixer, the observation region immediately follows the mixing region and by shrinking the

overall length scales for the entire apparatus by using glass tube capillaries (*46-53*) or sub-millimeter high precision machining (*54-56*), the turbulence dies down within a relatively short distance, allowing a dead time on the order of 100 μs. Since all measurements taken at a single flow rate and position correspond to the same time after mixing, limitations on the speed of the measurement itself are lifted, allowing for higher resolution, time-integrated measurements.

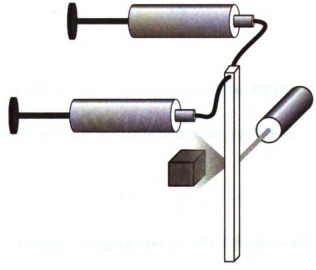

Figure 1.4.3 In a continuous-flow mixer, the mixing and observation chambers are combined and mixing occurs at the top of the chamber. The mixed solution flows down the chamber at a constant rate and the detector moves along the chamber to take measurements corresponding to different times after mixing.

However, high flow-rates of the order of ml/s are needed in order to create the turbulence necessary for mixing, which is prohibitive for use with expensive biochemical samples. The high flow rates also yield flow instabilities that can be difficult to control, making operation of the mixer difficult.

Limits on Turbulent Mixing

For many proteins, much of, if not the entire, folding process can be missed within the dead time of a stopped-flow mixer or even a capillary mixer. In order to

observe the early events in protein folding, it is necessary to find a way to go from fast to ultra-rapid mixing.

Going back to the coffee and cream analogy, instead of using turbulence or waiting for diffusion, let us simply stir the coffee. By stirring, the time necessary to displace some of the cream from one side to the other of the cup is

$$t_s = \frac{l_s}{v_s} , \tag{1.11}$$

where l_s is the distance stirred and v_s is the velocity of the stirring motion (*57 p.9*). In comparison, the diffusion time for any particular cream particle is

$$t_D = \frac{l^2}{D} , \tag{1.12}$$

where l is the distance the particle travels and D is the diffusion constant of the cream particle in coffee. On the molecular lever, all mixing is diffusive, but for macroscopic length scales (such as those the size of a Starbuck's venti) the diffusion time is so long, it is necessary to stir the coffee and cream into smaller and smaller regions with shorter diffusion times, much like turbulent mixing as described earlier.

Therefore, it would seem that by simply continuing to decrease the size of the mixer and the ensuing length scales, one could make even faster mixers with even shorter dead times, but in reality these designs reach a hard limit imposed by fluid mechanics. There is actually a minimum feature size for a turbulent mixer so that if the features are scaled even smaller, mixing times will actually increase. To understand this, it is best to start with the Navier-Stokes equation.

$$\rho\left[\frac{\partial \mathbf{u}}{\partial t}+(\mathbf{u}\cdot\nabla)\,\mathbf{u}\right]=-\nabla P+\eta\nabla^2\mathbf{u}\,, \qquad (1.13)$$

This equation, which is the basis of all incompressible fluid dynamics is essentially **F** = ***m*****a** for a fluid. On the left side is the density times the acceleration field (both the time and spatial derivatives of the velocity field) and on the right is the sum of the forces, resulting from a pressure gradient and velocity dependent viscosity.

By taking the ratio of the inertial forces to the viscous forces one can derive the Reynolds number:

$$Re=\rho\frac{u/t+u^2/l}{\eta u/l^2}\,, \qquad (1.14)$$

where u, l, ρ, and η are a characteristic fluid velocity, length, density and viscosity (*58*). A mixer's characteristic length is based on its geometry, for example the diameter of the mixing chamber channels. For constant flow, the Reynolds number can be simplified as

$$Re=\frac{ul}{\nu}\,, \qquad (1.15)$$

where ν is the kinematic viscosity (*57*). The Reynolds number is a unit-less constant that tells the nature of the fluid dynamics in a system. It tells what kinds of forces dominate, viscous or inertial. As the length scale l gets smaller, the Reynolds number also decreases, showing that viscous forces are starting to dominate. A person in a pool of water (with l ~ height and u ~ kicking speed) will have a Reynolds number of about 10^4, a fish about 10^2 and a bacteria of about 10^{-4} (*57*). Turbulent flow can only occur at high Reynolds numbers, typically > 10^3 (*58*). At lower Reynolds numbers flow typically

becomes laminar and at low Reynolds number, $< 10^2$ there is never turbulent flow. Capillary continuous-flow mixers require such high flow rates because their dimensions have become so small that they cannot achieve a high enough Reynolds number to allow turbulence any other way. This would appear to introduce a physical limit to the minimum feature size of a mixer design and therefore a minimum possible dead time, but by finding a novel mixing method instead of turbulence, designs can overcome this limit.

In this thesis I present two novel microfluidic mixers. The first is capable of measuring UV fluorescence with a mixing time 500 times shorter than the current state of the art. The second is capable of kinetics measurements of intramolecular diffusion as well allowing us to determine the diffusion coefficient of unfolded proteins in folding conditions for the very first time. Both of these methods are applied to the same protein, the B1 domain of protein L, to discover new processes early in the folding path.

2. Ultrarapid Microfluidic Mixing

2.1 Hydrodynamic Focusing T-Mixer

Focusing Mixer Principals

Starting with the Navier-Stokes equation (eq. 1.10), allowing the left hand side to go to zero and keeping all the non-inertial terms, yields the Stokes equation for laminar flow:

$$\eta \nabla^2 \mathbf{u} = \nabla P \ . \tag{2.1}$$

Note that in the low Reynolds number regime, all motion is governed by this simple differential equation and entirely determined by applied pressures and the system geometry. Furthermore, all flows can be calculated numerically by including constraints, ie: non-compressible fluid (∇ x $\mathbf{u}$ = 0) and non-slip boundary conditions ($\mathbf{u}$ = 0 at the walls). An interesting consequence of low Reynolds number flow is that there is no time derivative and consequently all motion is symmetric in time, meaning that if the applied pressures are reversed, all motion is also reversed (*57*).

One of the earliest mixer designs utilizing low Reynolds number flow is the hydrodynamic focusing mixer first introduced by Brody et al. (*58, 59*). The original design had a minimum feature size of about 1 – 2 μm and was comprised of 4 channels meeting at the center of the mixer. The top channel supplies the protein denaturant solution and the two sides supply buffer. The two solutions are mixed at the center and exit through the bottom channel. The mixer was originally fabricated using a silicon

wafer substrate. Features were etched 10 μm deep using a photolithography process at a Micro-Electro-Mechanical Systems (MEMS) fabrication facility and sealed with a glass cover-slip allowing the entire mixer to be viewable.

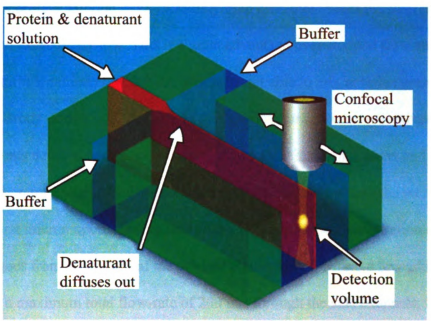

Figure 2.1.1 Schematic showing the basis behind the hydrodynamic focusing microfluidic mixer. The protein-denaturant solution is focused into a jet less than a micron wide. The protein in the jet experiences a local change in denaturant concentration, going from 90 to 10% of the original concentration within the first 10 μm of formation.

When flowing, the buffer solutions from the side channels focus the center protein denaturant solution into a ~ 100 nm wide ribbon, or jet, that flows down through the exit channel where it is observed. Diffusion time is related to particle size, and the protein molecules are much larger than those of the denaturant, either urea or guanidinium, which makes the diffusion time for a protein, about 10^{-2} s to diffuse 1 μm, 10 times longer than that of the denaturant (*58*). This means that the denaturant diffuses quickly out of the stretched and very thin jet soon after formation, but the protein molecules stay

within a micron of the center streamline for the duration of their flow through the exit channel.

In order to produce a jet, the microfluidic chip is designed to flow with a ratio of 100:1 diluent:protein solution – an incredibly high ratio that makes the final denaturant concentration exceedingly low. This is a great advantage over stopped flow and continuous turbulent mixers, which are generally not able to mix at ratios great than 10:1.

The Brody design was the basis of the hydrodynamic focusing T-mixer used in the experiments detailed here. David Hertzog in the Bakajin lab at Lawrence Livermore National Laboratory originally designed the mixers. In the first design the jet forms within the first micron upon entering the mixing region and the concentration of denaturant goes from 90 to 10% of the original concentration within a few additional microns. At a maximum total flow-rate of 200 nl/s through the side channels, the design has a Reynolds number of 15 and a mixing time of 8 μs, as defined by the corresponding time to drop from 90% to 10% of the original denaturant concentration (*60*).

The current mixer design has been through at least three different design iterations, improving on all aspects through extensive use of computer modeling (COMSOL Multiphysics, Stockholm, Sweden). The first iteration, as described above was a simple T-design. The design was improved computationally by running numerical simulations to minimize the mixing time (*61*). The simulations operated by varying the design geometry and flow rates to find the global minimum in the mixing time using a semideterministic algorithm (*62*). The algorithm arrived at a design that introduced a constriction at the mixing region, making the fluid flow faster through the region where the jet is being formed, and shortening the mixing time from 20 μs to 8 μs when flowing

at the same flow rate (*61*). The design also lowered the sample consumption through the center channel from 5 nl/s to 3 nl/s.

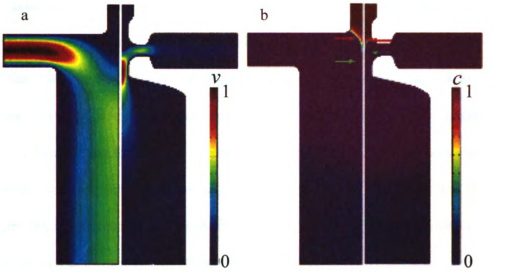

Figure 2.1.2 a) Simulated velocity field plots of the earliest design on the left (*60*) and the second iteration (*61*) on the right. They are both normalized with a V_{max} of 3.25 m/s at left and 17.3 m/s on the right. b) Color map of the normalized denaturant concentration of the same two designs. The red arrows point to the locations of c = 90% and the green to c = 30%. This image is taken from ref (*61*).

Because of the increased fluid velocities in certain regions of the microfluidic chip, a new limit was reached in the design. In the original designs, the simulations were simplified by assuming that, aside from the very top and bottom of the channels, motion was uniform across the majority of the flow cross-section and therefore only the center 2D plane, parallel to the flow geometry, had to be simulated. At low flow velocities this approximation is valid since, even with no-slip boundary conditions, the channel top and bottom are far enough away that they do not influence the velocity in most of the channel. At high velocities, however, this is no longer valid, especially when the fluid makes a sharp turn such as the path of the buffer solutions entering the mixing region. In this case the fluid on the top and bottom of the channel have a lower velocity than that in the middle going through the turn, and therefore the fluid in the center of the channel

feels a greater centrifugal force towards the outside of the bend, eventually forcing the center fluid to fold over itself along the top and bottom of the channel in a phenomena called a Dean vortex. These vortices were first characterized in flows through curved pipes with high Dean number flow (*63*). The Dean number is defined as the Reynolds number time the square root of the ratio of the flow cross-sectional radius and the radius of the flow curvature. In the case of the mixer, at high flow rates the protein solution enters the mixing region through the center of the chip and is forced into the jet by the side channel solutions, which have been bent 90 degrees. At the 90 degree turn, the side flows form Dean vortices mirrored on both sides and bifurcate the center solution into two flows along the top and bottom thirds of the channel which are no longer moving at the flow velocity determined at the center plane of the chip.

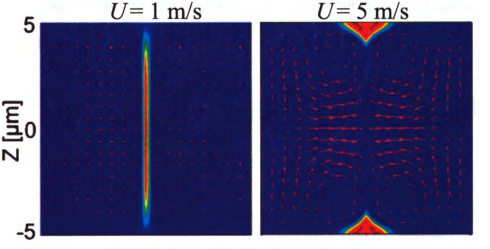

Figure 2.1.3 A cross-sectional vector map showing the fluid velocity vector component normal to the channel at the very top of the mixing region where the side solutions are forced into a 90 degree turn overlaid with a concentration intensity map showing the sample solution. The map on the left shows that at low flow rates, the velocity field is uniform with almost no velocity normal to the flow down the channel. At a high flow rate, as shown on the right, much of the fluid velocity is towards the center where near the mid-plane of the channel, the fluid is forced upwards causing Dean vortices as shown by the circular velocities. Note that the sample solution shown on left is a uniform jet, and on right is bifurcated at high flow rates (*64*).

Bakajin et al. at Lawrence Livermore National Laboratory solved the problem of the Dean vortices in the third iteration of the design (*64*). In the new design, the side channels are redirected downward immediately before entering the mixing region. In the final version, the mixer was able to produce a uniform jet across the entire cross-section of the observation channel for flow rates greater than 5 m/s, yielding a mixing time of 4 μs to go from 90% to 10% of the initial denaturant concentration and only 1.2 μs for it to reach 30% concentration – a level usually below that necessary for many proteins to begin to refold.

The current version of the hydrodynamic focusing mixer used in the experiments detailed here is slightly revised from the optimum design by Yao. In the current version, the minimum feature size is slightly larger to lessen the possibility of clogs and to enhance fabrication yields. The current design has a uniform jet up to 3 m/s and a mixing time of about 8 μs.

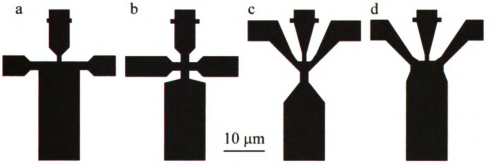

Figure 2.1.4 a) The first hydrodynamic focusing mixer. b) The second iteration after the geometry was improved by finding a global minima in the mixing time. In this design the channel immediately following mixing is constrained, making the fluid velocity faster in the mixing region. c) The design by Yao that lessens effects caused by Dean vortices. In this design the side channels enter the mixing region at much smaller angle than the previous design, lowering any centrifugal forces experienced by the fluids. d) Mixer design used by the Lapidus lab. The feature sizes are slightly larger than that of the optimum design, lessening the occurrences of clogging and allowing slightly higher tolerances during fabrication.

Focusing-Chip Properties

The hydrodynamic-focusing microfluidic-chip measures 20 by 20 mm square by 670 μm thick and is manufactured out of fused silica. All features inside the chip are etched about 10 μm deep as described in section 2.3.

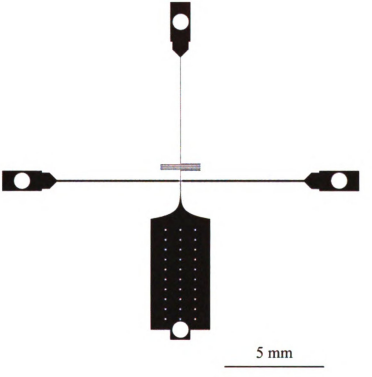

Figure 2.1.5 Geometry of a single T-Focusing microfluidic-chip. At the center of the chip is the hydrodynamic focusing mixing region. Radiating outward are four microfluidic channels. The top channel, named the supply or center channel, transports the protein-denaturant solution to the mixing region. The side channels on the left and the right of the mixing region supply the diluent necessary for mixing. The exit channel at the bottom allows the mixed protein solution to flow out of the mixing region to where it can be observed and then later collected. On the back surface of the microfluidic-chip are four through-ports, shown as circles located at the end of each channel. The holes allow external experimental solutions access to the interior of the microfluidic chip and are either drilled by a computer numeric controlled (CNC) mill or sandblasted during the final stages of fabrication. Each hole is centered about 2 mm from the edge of the chip and is up to .5 mm in diameter.

In order to produce a jet, a fluid-flow ratio between the center and side channels (Q_c/Q_s) of about 1% must be maintained. The hydrodynamic focusing T-mixer design uses air pressure to push the solutions through the microfluidic chip by pressurizing the

volumes above the different solution reservoirs. Although it could be possible to attain the optimum flow ratio of 1% by designing the microfluidic channel geometry such that a set pressure ratio produces the desired flow ratio in a one-to-one manner, maintaining this flow-ratio would be exceedingly difficult because the center pressure setting would be two orders of magnitude smaller than the side pressure. By differing the channel geometry between the supply and side channels, it is possible to attain the optimum flows at more convenient pressure ratios. This is accomplished by changing both the cross-sectional area and overall distance of the channels before they reach the mixing region, with long narrow channels providing more resistance to flow than shorter, wider channels.

The three input channels, the center and the two sides, start about 1 mm from the edge of the chip and are 1 mm wide out of convenience for drilling the through-hole ports, which are about .5 mm in diameter. After 2 mm from the start of the channels, they narrow to 800 μm and enter a filter section, which is necessary to remove any particles or debris from the solutions that could clog or damage the small features and openings inside the mixing region. Although all the solutions are first filtered through a 0.22 μm syringe filter (Millipore, Billerica, MA) before use, the in-chip filters provide one last precaution. They also act as flow resistors to help control the flow ratio between the center and side channels.

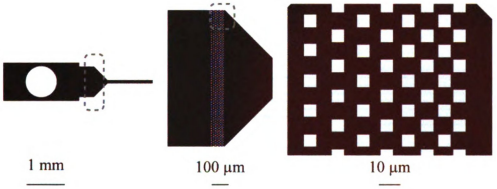

Figure 2.1.6 The filter regions are comprised of 8 rows of square posts measuring 6 μm per side spaced 8 μm apart. The rows alternate such that the position of a post in one row faces a gap between posts in the next, making a checkerboard like array. The distance between consecutive rows starts at 7 μm and decreases to 1 μm, making the minimum distance between the edges of nearest neighbor posts 1.4 μm, which is the maximum size particle that would be able to traverse through the filter section.

Following the filter section, the channels start at 800 μm wide and then narrow to 80 μm in the side channels and to only 10 μm wide for the supply channel. The side channels continue at this width for 6.1 mm all the way to the mixing region in the center of the chip. The center channel has a large serpentine region that extends the total distance of the channel from about 6.1 mm to almost 20 mm long. The serpentine section acts as a resistor, much like that in an electronic circuit and has a resistance of 6.2×10^{16} $Pa/(m^3/s)$.

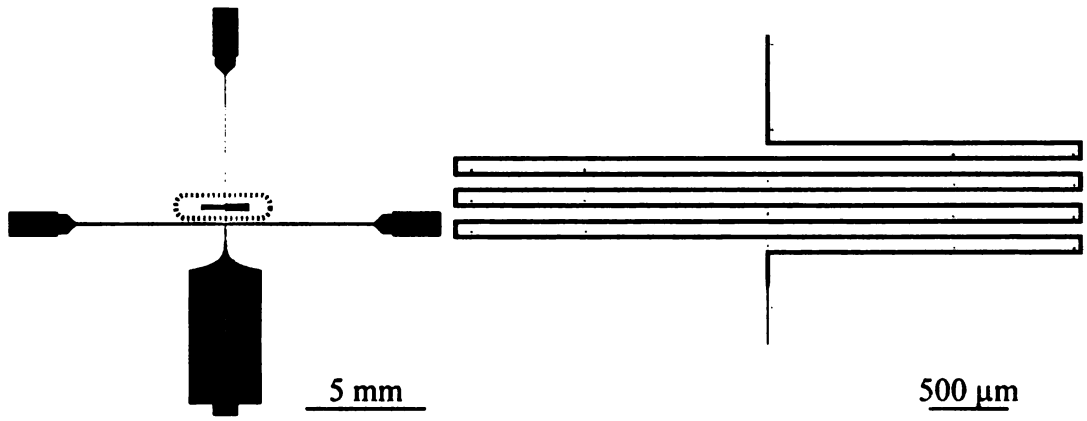

Figure 2.1.7 The serpentine region switchbacks seven times, making the 10 µm wide center channel 19.75 mm long. Following the serpentine region, the channel narrows again, this time to 5 µm and continues a final 400 µm to the mixing region.

As described in section 2.1, the mixing region itself is about 5 µm long and empties into the exit channel of the microfluidic-chip. Within a couple microns following the mixing region, the exit channel quickly widens to 10 µm and extends for 500 µm. This 500 µm long region is the observation region of the microfluidic-chip, where UV fluorescence or other optical measurements are taken. Following the observation region, it is necessary to widen the exit channel cross-section in order to lower flow resistance of the exit solution and decrease any backpressure on the input solutions.

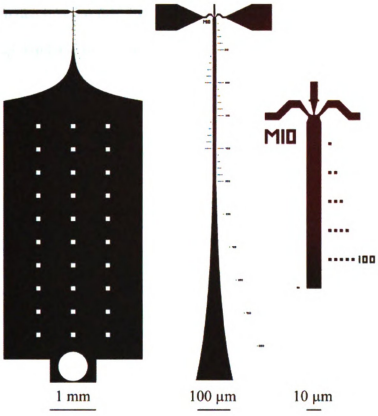

Figure 2.1.8 As shown on the left, the exit channel widens exponentially in 1425 µm to 3000 µm wide and continues for another 5.6 mm towards from the bottom edge of the chip, ending with a nub large enough to drill the exit port through. The large posts seen inside the widest region measure 100 x 100 µm are 400 µm apart and provide structural strength to the microfluidic chip by supporting the coverslip during the bonding process described in section 2.3. Shown in center is the 500 µm long observation region which widens exponentially at the end. At right is the first 100 µm of the observation region.

A single microfluidic-chip can generally be used for up to about 2 weeks before the quality of the jet starts to diminish. Possible causes for the loss of quality include protein aggregation inside the exit channel or mixing region and debris escaping past the filters and clogging either the side or center channels. If the nature of the clog is organic, such as dust, protein aggregation or even bacterial growth, the chip can often be recovered by immersion in a piranha solution (3:1 H_2SO_4:H_2O_2) bath and a subsequent

thorough rinse in deionized water. Eventually the jet will degrade irreparably and the microfluidic-chip will have to be permanently retired.

T-Mixer Chip Manifold

The physical connection between the microfluidic mixer chip and the rest of the instrument is through a two-part assembly, comprised of a chip holder/fluid reservoir manifold and a pressure distribution headpiece.

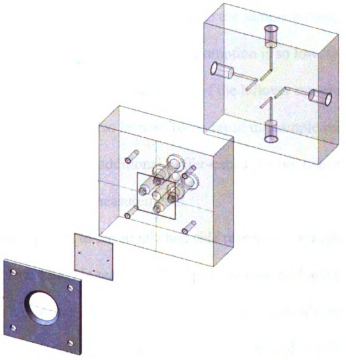

Figure 2.1.9 The microfluidic-chip is secured to the holder manifold with a machined aluminum faceplate (shown at far left) and affixed by four screws. The faceplate has a 1.5 cm diameter beveled window in the center to allow the objective to scan an area containing the mixing region as well as the entire observation region (500 μm long region of the exit channel). The chip (shown to the right of the faceplate) is secured oriented with the four through-ports facing corresponding o-rings seated in the manifold (shown at center). Machined into the manifold directly above (directed towards the top right in the image) the four ports on the microfluidic-chip are four wells, or reservoirs, each of a volume of about 400 μl that either hold the sample or buffer solutions or collect the spent solution. A large hole is machined through the center of the manifold directly above the mixing region of the affixed microfluidic-chip, allowing excess UV light to escape without backscattering through the objective as well as inhibiting any auto-fluorescence from the manifold itself. It also allows direct illumination of the microfluidic-chip features during optical microscopy alignment steps. The pressure distribution headpiece (shown on far right) is affixed above the manifold and seals each of the reservoirs such that the air pressure in each can be controlled via an external pressure control box.

In a typical experiment the side channel reservoirs are both filled with 200 μl of diluent solution, typically buffer, and the center channel with about 20 - 50 μl of protein in solution with high concentration denaturant. These volumes allow experimentation times ranging from less than 30 minutes to a couple hours depending on the pressures and corresponding flow rates used, before having to refill the side channel and empty the exit channel wells. The center channel well, filled with the sample protein solution, usually does not have to be refilled because sample consumption is so low, typically only a few μl per entire dataset. After the experiment most of the leftover sample can be recovered from the center well. It should also be possible to reuse the sample recovered from the exit well although there may be additional buffer-exchange and concentration steps involved before the next set of measurements.

Pressures are applied to the supply and side reservoirs through the pressure distribution headpiece which is sealed to the top of the manifold and connected via high pressure tubing to a pressure control box where the center and side pressures are regulated. The pressure control box is comprised of two sets of two pressure transducers, one set for low pressure ranges, 0 – 15 psi (Marsh Bellofram, Newell WV) and the other for larger ranges up to 120 psi (type 2000). All of the transducers are computer controlled, reducing the house air pressure from 90 psi to the working pressure used in a mixing experiment, typically 10 – 50 psi. Also contained in the box is a set of computer-interfaced pressure gauges used to measure and verify the instantaneous set pressures for the instrument.

There are currently two different manifold-headpiece assemblies, both constructed from the same design. The first is machined out of clear acrylic (lexan) and is

used typically for room temperature experiments. The second assembly, shown in Figure 2.1.10, is used for temperature dependent experiments and is machined from aluminum, due to its high thermal conductivity.

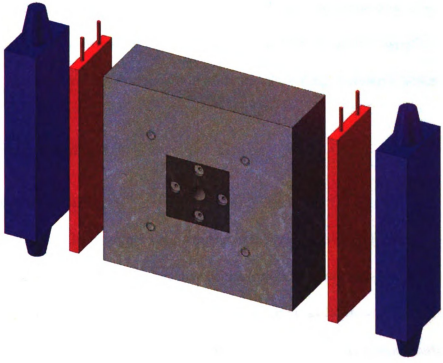

Figure 2.1.10 Two Peltier modules (TE Technology CH-77-1.0-0.8, Traverse City, MI - shown in red) are sandwiched on opposite sides of the manifold by water-cooled heat sinks (shown in blue). The Peltier modules and heat sinks provide either cooling or heating to the entire assembly and are controlled by a digital controller (TE Technology model 1600). A thermistor affixed to the side of the headpiece and connected to the controller measures the temperature of the assembly and completes the feedback loop for the controller allowing the manifold to be well regulated with a temperature range from 0 – 100 C. To cut down on scattered and reflected light, the temperature manifold is anodized black on the surfaces where the microfluidic-chip is seated.

When tested, there was no discernable difference between the temperature measured directly on the surface at the center of the microfluidic-chip and the temperature set by the controller and measured from the body of the headpiece after all have reached equilibrium. For low temperature measurements, a jet of dry nitrogen gas is aimed at the underside of the microfluidic-chip to prevent surface condensation.

When the aluminum temperature manifold was first used it was found that, because of the ionic nature of the buffer solutions used in protein folding experiments, even with the protective oxide layer and anodization, aluminum salts would still precipitate out of solution inside the microfluidic-chip, causing irreparable clogs. This problem was solved by providing the manifold with an inert protective layer of Parylene applied through chemical vapor deposition (Advanced Coating, Rancho Cucamonga CA).

2.2 Serpentine Mixer

Chaotic Advection Mixing

The extremely low sample volume used in the hydrodynamic focusing mixer is one of its greatest assets. However because of the low sample volume the design can only be used with a limited number of high-fidelity probes such as fluorescence. For probes that require a large number of protein molecules, such as light absorbance measurements or small angle X-ray scattering, a signal from the $1 \times 0.1 \times 10$ μm volume of protein inside the mixer at a given moment would be far too small. Instead, we need to find another clever method to mix without turbulence.

The Dean vortices, described in the earlier section, point to a way out. Dean vortices are one of the phenomena present in chaotic advection, first defined by Hassan Aref in 1984 (*65*). The hydrodynamic focusing mixer mixes solutions simply by increasing the interfacial surface area of the two fluids (sample and buffer) in order to speed up diffusion – essentially mixing without stirring at all. To understand, we start with advection, which can be described as the motion of a particle in a moving fluid such that,

$$\mathbf{V}_{particle} = \mathbf{V}_{fluid} \cdot \tag{2.2}$$

The equation describing the particle velocity is:

$$\mathbf{V}_{particle} = \left(\frac{dx}{dt}, \frac{dy}{dt}, \frac{dz}{dt} \right) \cdot \tag{2.3}$$

Whereas the equation to describe the motion of the fluid is:

$$\mathbf{V}_{fluid} = \left[u\left(x, y, z, t\right), v\left(x, y, z, t\right), w\left(x, y, z, t\right) \right]. \tag{2.4}$$

This leads to the advection equations:

$$\frac{dx}{dt} = u\left(x, y, z, t\right), \tag{2.5.a}$$

$$\frac{dy}{dt} = v\left(x, y, z, t\right), \tag{2.5.b}$$

$$\frac{dz}{dt} = w\left(x, y, z, t\right) \tag{2.5.c}$$

which are just three ordinary differential equations, that from the vantage point of dynamical systems theory are more than enough to produce nonintegrable or chaotic dynamics (*66*). In fact, the flow does not need to be time dependant in order for chaos to result; the geometry of the fluid channels can be enough to stir the fluid pushed through. Whitesides et al. described the chaotic advection behind an early chaotic mixer as introducing "transverse components of flow that stretch and fold volumes of fluid over the cross section of the channel." (*67*)

Figure 2.2.1 Three different types of chaotic advection microfluidic mixers. a) A herringbone pattern etched into the bottom channel creates circular vortices as shown in the inset images(*67*). b) A bended channel(*68*). d) Twisted channels (*69*). Some designs split and recombined the fluid many times such as c) (*70*) and e) (*71*).

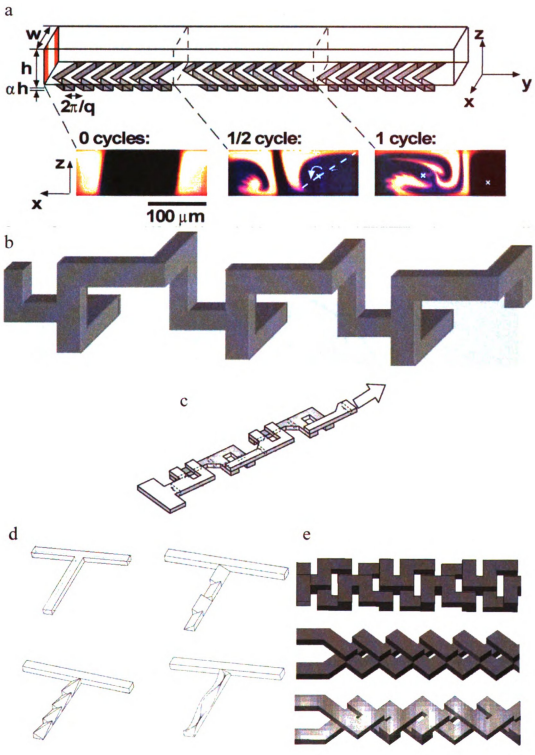

Figure 2.2.1

The mixer design used in the experiments detailed later has a much simpler but effective flat serpentine channel, first described by Chamarthy and Wereley (*72*). The mixer uses two different aspects of chaotic advection, Dean and corner vortices. Dean vortices, as described in the previous section, are caused by sharp bends in the fluid motion. Corner vortices are found in the flow immediately following corners very close to the channel sides and result from discontinuities in the boundary conditions found at the sharp edges of a corner.

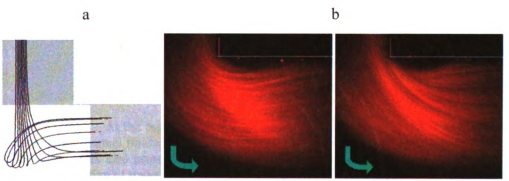

Figure 2.2.2 a) Visualization of flow trajectories as they go around a bend showing a Dean vortex. Re = 80 (*68*). b) Flow visualization using a low concentration of tracking particles at Re = 93. Left shows flow at the top wall of the channel and the right shows flow at the mid plane (*72*).

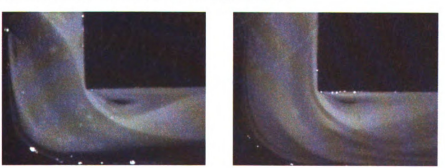

Figure 2.2.3 Epifluorescence images showing corner vortices at Re = 200 (*72*).

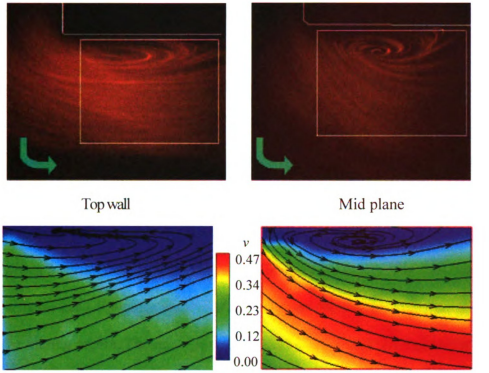

Figure 2.2.4 At the top wall, fluid spirals into the corner vortex and at the mid plane of the channel fluid spirals out and rejoins the channel flow. This interacts with the Dean vortex also present. At top are visualizations of the flow trajectories of a low concentration of tracer particles, Re = 136 and below are simulated stream traces for Re = 200 (*72*).

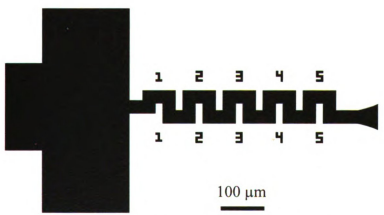

Figure 2.2.5 Serpentine mixing region taken directly from the current photolithography mask as designed by Avinash Kane. The serpentine comprises 5 total periods, each made of 4 turns and is a total of 981 μm long for a streamline through the center.

The serpentine design is a periodic repeat of bends, shown in Figure 2.2.5. At the optimum flow rate of Re ~ 200, the Dean and corner vortices will interact. This

interaction plays a key role, Chamarthy et al. claiming, "In each period of the channel, the Dean vortices stretch the mixing plane and the corner vortices 'cut' and 'fold' it (*72*)," much the same way as the mixer designs shown in figure 7 (d) and (c) but using a much simpler design with only one layer of channels.

The current serpentine microfluidic mixer used to collect all the data in the Trp-Cys contact quenching mixer project was designed by Avinash Kane in the Bakajin lab at Lawrence Livermore National Laboratory (*73, 74*). The design starts with a T-mixer that is inline with a 5 period serpentine region. When flowing at the optimum flow rate of 250 μl/min the mixer has a Reynolds number of 120. It takes about 282 μs for the fluid to traverse the mixing region. The mixer is still efficient at flow rates lower than the optimum down to Reynolds number of about 60.

In order to test the mixing efficiency, a series of confocal microscope images, as described in Section 3.2, were taken with a low concentration of the fluorophore Fluorescein in the center channel solution at different flow rates and ratios between the side and center solutions. The quality of the mixing was evident visually (see Figure 2.2.6) with Reynolds numbers below 20 showing no evidence of any mixing at all.

Figure 2.2.6 Confocal microscopy images taken of the serpentine mixer at different flow rates, in plane with the serpentine on left and cross sectional of the channel immediately following the serpentine at right. a) Image showing no mixing because the Reynolds number is too low (Re = 14.3). Note that a jet of the Fluorescein solution produced by the T at the start of the mixer progresses through the serpentine without any interference. b) The effects of Dean and corner vortices cane be seen here at flow with Re = 83. c) Image of the full channel is shown by flowing only Fluorescein solution. Mixing is also evident from the cross sectional image (right panels).

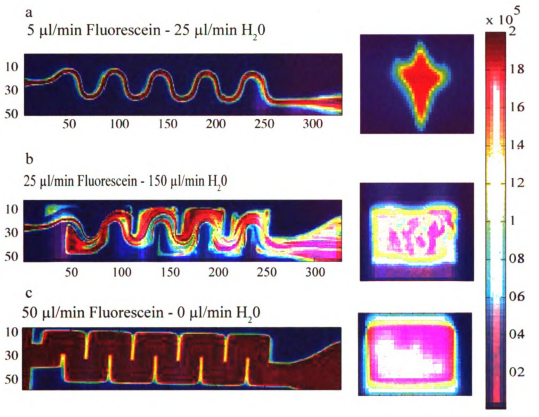
a
5 µl/min Fluorescein - 25 µl/min H20
10
30
50
50
100
150
200
250
300
b
25 µl/min Fluorescein - 150 µl/min H20
10
30
50
50
100
150
200
250
300
c
50 µl/min Fluorescein - 0 µl/min H20
10
30
50
x 10^5
2
18
16
14
12
1
08
06
04
02

Figure 2.2.6

It is important to be able to quantify the quality of mixing in order to assess the character of a mixing design and to find the optimum flow conditions for a given mixer. Chamarthy et al. found that the method of Coefficient of Variance provides a sufficient way to quantify the quality of mixing and is defined as:

$$CoV = \frac{\sigma}{I_m} = \frac{\sqrt{\frac{\sum (I_i - I_m)^2}{N-1}}}{I_m}, \qquad (2.11)$$

where I is the intensity at a given pixel and I_m is the mean intensity. When used on the cross-sectional images shown in Figure 2.2.6, the top image (a), where Re is too low for efficient mixing, the CoV value is 0.33. For the flooded instance shown in the bottom image (c), the CoV is much lower with a value of 0.17. An entirely uniform image would have a CoV of exactly 0. The middle image showing efficient mixing has a CoV of 0.15, which is very comparable to that of the flooded instance. As shown in Figure 2.2.7, which plots the CoV as a function of Reynolds number, that Re = 60 or higher produce efficient mixing.

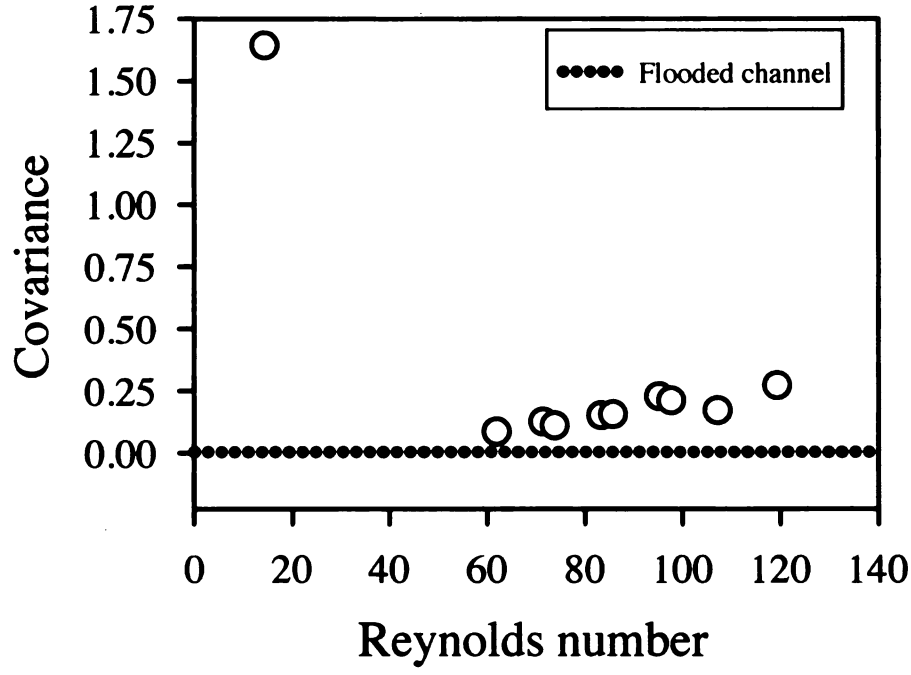

Figure 2.2.7 Plot showing mixing efficiency, as defined by equation 2.11 as a function of Reynolds number. Flow with very low Reynolds number, Re = 14 produces a very high CoV, however at Re ≥ 60, the CoV is much closer to that of the flooded channel.

Serpentine Mixer Microfluidic-Chip Properties

The serpentine mixing chip measures 30 mm wide by 10 mm high and is 670 μm thick. It is fabricated out of fused silica using the process described in section 2.3 and has features etched 30 – 40+ μm deep.

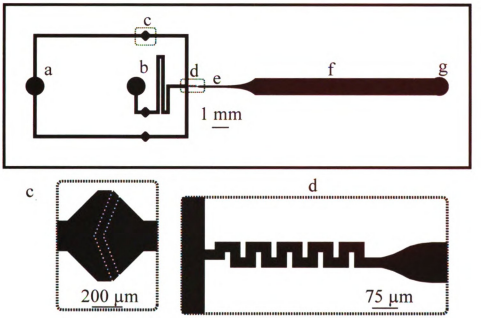

Figure 2.2.8 Geometry of the chaotic advection mixing microfluidic-chip. a) Buffer inlet. b) Protein solution inlet. c) Filter section (one of three total per chip). Each filter post is a 10 by 10 µm square and they are spaced 10 µm apart. d). The serpentine mixing region is comprised of five turns and the channel is 30 µm wide. e) The narrow observation region is 120 µm wide and 1.4 mm long. f) The wide observation region is 1000 µm wide and 10.4 mm long. g) Outlet port.

The chip has only three ports, an inlet for the buffer solution and one for the protein and denaturant solution and an outlet for the mixed solution. In this design, the buffer solution is divided internally into two side channels that meet at the mixing region, where they are combined in a T configuration with the protein solution immediately before entering the serpentine mixing region. Following the mixing region the chip has two observation regions, the first 120 µm wide for measurements on a fast timescale and the second 1000 µm wide for measurements on a timescale an order of magnitude larger.

A manifold similar to that used by the T-mixer chip provides the physical connection between the microfluidic chip and the rest of the instrument. The chaotic advection design has a significantly higher fluid consumption rate than that of the T-mixer, microliters versus nanoliters per minute. These high flow rates are needed in order

to obtain optimum mixing and because deep channels are necessary to increase the path length for absorbance measurements. This trade-off for higher consumption allows for a simpler manifold design. Instead of using air pressure to force solutions stored in internal manifold reservoirs through the chips, the solutions are provided by syringes plumbed to the manifold via high-pressure tubing. The flow rates are controlled directly by computer controlled syringe pumps (KD Scientific model KD200, Hollison MA).

The chip's internal pressure is not uniform and can only be determined computationally as a function of flow rate and geometry. Pressure fluctuations can contribute to instabilities, especially if bubbles are present inside the manifold tubing or the syringes, which allow the solutions to act as compressible fluids. This can be especially problematic at low flow rates. It may take minutes for the flow to reach equilibrium after a flow rate has been changed. Also problematic is that abrupt changes in the chip geometry, such as the transition between the narrow and wide observation regions, can cause a stationary large pressure drop within the chip at a given flow rate. This drop can then induce dissolved gasses to come out of solution and form bubbles within the chip, further changing the microfluidic properties.

2.3 Microfabrication

All of the microfluidic mixer chips were fabricated at either the Center for Micro- & Nano-Technology at Lawrence Livermore National Laboratory or the UCLA Nanoelectronics Research Facility. Both microfabrication facilities feature class 1000 clean rooms and the equipment and chemicals needed for microelectromechanical system (MEMS) fabrication, such as etchers, mask aligners, and wafer handling machinery. The clean room is especially important because dust and contaminants can destroy the

micron-sized features and lower the yield of workable devices. Some of the later fabrication steps were also performed at the W. M. Keck Microfabrication Facility at Michigan State University.

The fabrication process starts with 500 μm thick, 4 inch diameter wafers made of highly polished high grade fused silica substrate (SENSOR Prep Services, Elburn IL). Fused silica is one of the more difficult substrates for microfabrication due to the limited family of chemicals and processes that are capable of etching it, with the exception of hydrofluoric acid (which can be highly dangerous). However, fused silica has been found as the only compatible substrate due to its transparent properties at UV wavelengths.

The first fabrication step is to deposit a layer of polycrystalline silicon (polysilicon, or poly) on all the substrate surfaces. The poly is deposited by flowing silane gas (SiH_4) under very low pressure over the surface of the substrate in a 600 C furnace in a process called chemical vapor deposition (CVD). The poly layer acts as a stencil for the later fused silica etching step. In this process, ~ 1 μm of poly must be deposited for every 10 μm of the planned etch depth. Unfortunately, with the current deposition procedure, it is not possible to deposit a poly layer greater than ~ 4 μm thick due to the strain induced on the substrate in the substrate-deposition layer interface. Layers exceeding this limit can induce microfractures in the substrate that become visible after the poly has been removed. This limits the etching depth of the fused silica substrate to ~ 40 μm. It is conceivable that with an improved poly CVD method, channel depths of 100+ μm should be possible, doubling the signal size for the contact quenching measurements.

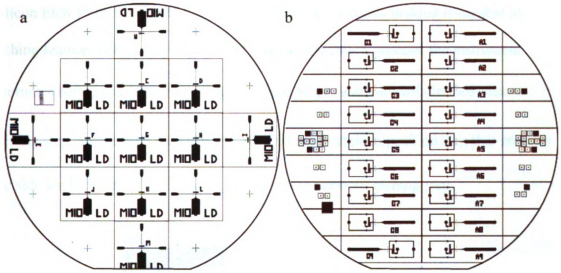

Figure 2.3.1 a) Mask pattern for the hydrodynamic T-mixer. There are 13 chips total, labeled A-M, on the wafer although the flat edge makes one unusable and the three others on the edge are also rarely functional. The dicing pattern is a simple 2 cm by 2 cm grid. b) Mask pattern for the chaotic advection serpentine mixer chip. There are 18 chips on the wafer, labeled A1-9 and C1-9, and with this design the chips cut off by the flat are often still functional. The dicing pattern is a 1 cm by 3 cm grid. The miscellaneous objects on the outer strips of the wafer are alignment and testing marks left from the mask development process.

The photolithography steps begin with spin coating the top surface of the substrate with a ~ 900 nm thick layer of photoresist (AZ 4110 or 5214). A UV mask aligner then aligns the mask with the wafer. Once aligned, the mask is brought into hard contact with a vacuum assist directly onto the wafer and the photoresist is exposed for about 6 seconds to UV light. By using hard contact with vacuum, it is possible to fabricate submicron size features without using stepper optics or e-beam lithography. Following exposure, the wafer is bathed in developer for about 60 seconds, revealing the mask pattern. The wafer is then inspected under a microscope and, if there are any defects, the photoresist is stripped and the photolithography is repeated.

Once the photolithography steps have been deemed satisfactory, the mask pattern is etched into the poly layer in a deep reactive ion etcher (STS Systems plc, Advanced

Silicon Etch 1998, Newport UK) that uses the Bosch process, making it capable of etching features with a very high aspect ratio. In the Bosch process, the instrument alternates between using a reactive gas such as SF_6 in a downward directed plasma-etching step, and using a gas such as C_4F_8 in a passivation deposition step that protects the side walls of any of the features created in the previous etching step.

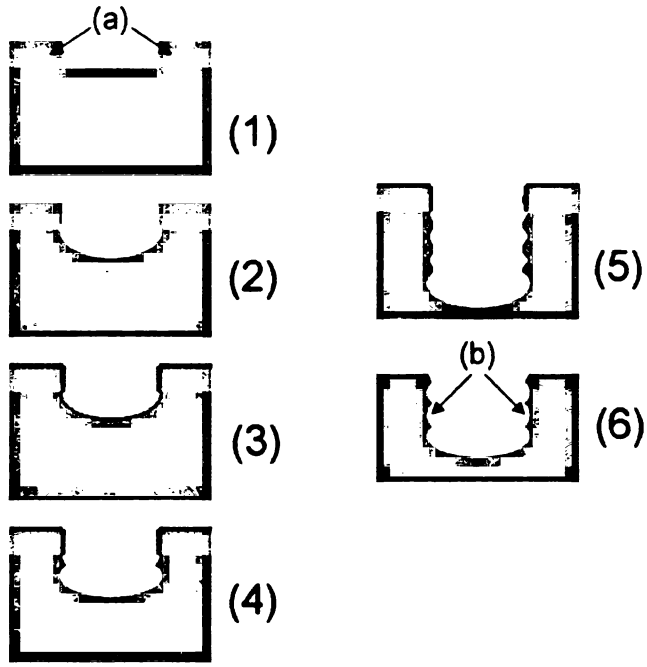

Figure 2.3.2 The Bosch process[3]. 1) Photoresist is shown as material 'a' and has a hole patterned on the Si substrate. 2, 4 and 5 show plasma etching steps and 3 shows the passivation layer deposition shown as the light green layer. Step 6 shows the final features after the passivation layer has been removed and 'b' points towards undulations in the sidewalls that can often occur as a result of the Bosch process.

Following the silicon etch step, the wafer is ready for the oxide etch step, which is done in a second, more sophisticated etcher (ULVAC Technologies, NLD570 Oxide Etcher, Methuen, MA). The ULVAC etcher is state of the art and uses a proprietary

---

[3] Image taken from wikipedia commons: http://commons.wikimedia.org/wiki/File:DRIE_Bosch_process.png.

process based on the Bosch process; it takes about 30 minutes to etch 10 μm with a selectivity of about 10:1 between the oxide substrate and the poly mask layer.

A XeF_2 etcher then removes the polysilicon mask layer from both the front and back surfaces of the wafer. Although the layer could be removed by a wet etching step, such as a KOH bath, it has been found that this pits the surfaces of the substrate and inhibits bonding.

To drill the through-hole ports for each chip (4 ports for the T-mixer and 3 for the serpentine design) a thick protective layer of photoresist is first spin-coated onto the top surface of each wafer, allowing the wafers to be removed from the clean room and shipped to the facilities at Michigan State University. Holes are drilled using a tabletop CNC mill (Sherline Products P/N 8020, San Marcos CA) programmed with exact positions taken from the original electronic mask design file. A diamond drill bit (WOLFCO Inc., W754720, Thompson CT) is used to drill holes .020 – .030" in diameter.

It is very important that all the glass grit produced in the drilling steps be cleaned from the substrate surface. This can be exceedingly difficult due to both van der Waals forces and hydrogen bonding from surface bound water molecules, holding the quartz particles to the surface. The ability to remove the particles is very sensitive to relative humidity, with the force needed to remove particles at 10% relative humidity increasing by a factor of 12 at 90% relative humidity (*75*). Although the grit may be entirely immobilized while the substrate is open to the air, after all the fabrication steps have been completed and the chip is used in an experiment, the grit become mobile once fluids fill the channels, at which point any grit can continue through the channels where it can clog a channel and render the chip unusable.

Before the last bonding steps, while the substrate surface is still externally accessible, it is important to measure the etched depths of the microfluidic channels with a surface profiler (Veeco Instruments Dektak^3 at MSU, Dektak 8 at the UCLA Nanolab, Woodbury NY). Depth information is important for calculating the fluid velocity from either the set pressure ratio for the hydrodynamic focusing T-mixer or from the volumetric flow rate for the chaotic advection serpentine mixer.

The final fabrication steps permanently bond the substrate wafer with a 170 μm thick coverslip, also made of fused silica. The coverslip and substrate are cleaned with a reverse RCA procedure with an RCA 1 (5:1:1 H_2O:NH_4OH:H_2O_2) bath as the last step. This last step ensures that the surfaces of both wafers are hydrophilic and, as such when placed in contact, the surfaces will bond spontaneously in a process called direct bonding (*76*). In order to make the bond permanent the wafers are annealed at 1100 C for two hours. Finally the wafers are diced into individual microfluidic chips that can be used immediately for experiments.

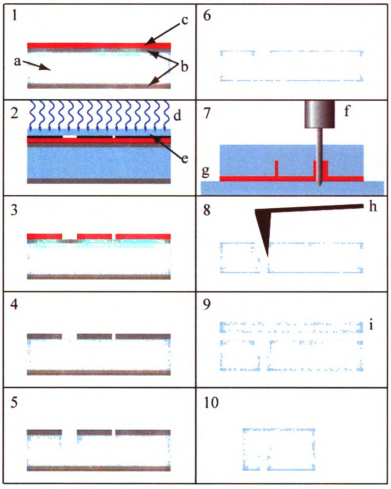

Figure 2.3.3 Cartoon showing the fabrication steps for a microfluidic mixer. 1. The process starts with a highly polished 500 μm thick fused silica substrate (a) with a layer of polysilicon deposited on the top and bottom surfaces (b) and spin-coated with a layer of photoresist (c). 2. A photomask (e) is brought into hard contact with the wafer and the photoresist is exposed to UV light (d). 3. The wafer is placed in a developer bath and the pattern is revealed in the photoresist. 4. The wafer is placed in a DRIE and the features are etched into the top poly coating. The photoresist is then removed. 5. The poly then acts as a mask when the wafer is placed in an oxide etcher and the features are etched 10 – 40 μm into the fused silica substrate. 6. The poly coating is then removed in a XeF_2 etcher. 7. The wafer is bonded to a sacrificial glass plate with a heat-activated sealant (g), features side down, and a diamond drill bit (f) abrasively drills through-holes from the backside. 8. A surface profiler (h) then directly measures the etched feature depths. 9. A 170 μm thick fused silica coverslip wafer is directly bonded on the top surface of the wafer. 10. The wafer is diced into individual microfluidic chips.

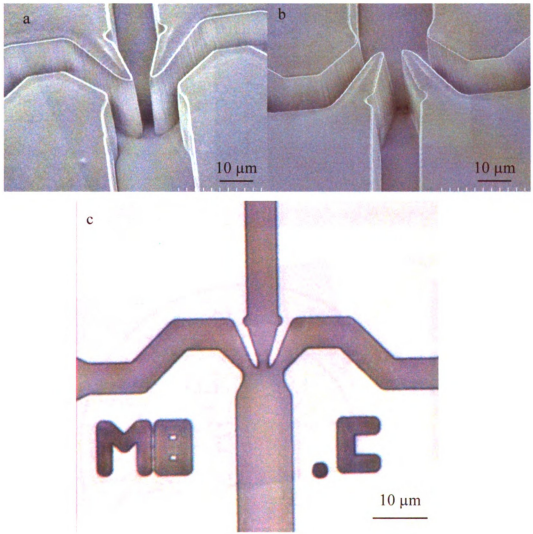

Figure 2.3.4 a) and b) Electron micrograph images of a hydrodynamic focusing mixer taken August 2008 at the UCLA Nanolab Facility. Note that the poly layer is still present and can be seen as the beveled edges seen on the top surface, especially between the side and center channel nozzles. c) Optical microscope image of a similar mixer taken in 2007 at the Lawrence Livermore National Laboratory.

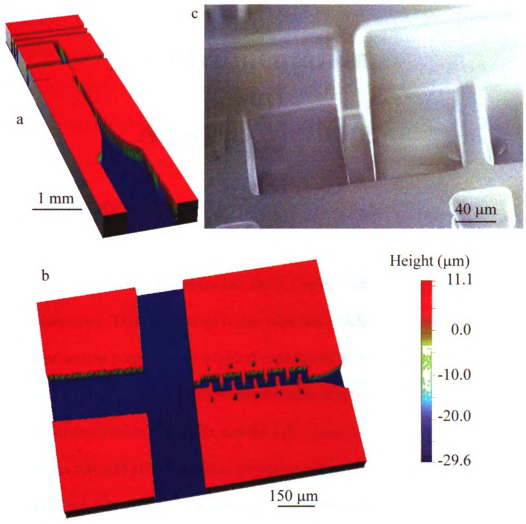

Figure 2.3.5 a) and b) Images from a stereo optical surface profiler (Veeco Instruments Inc. Wyco NT3300, Plainview NY). The images taken at the UCLA Nanolab facility show the uniform depth and surface smoothness of the etched channels in the 40 μm deep serpentine chip. c) An electron micrograph of the same chip. Note that the channel walls are slightly chamfered due to the early signs of failure of the polysilicon mask layer. There was enough of the original top surface of the substrate remaining for the wafer to still be deemed satisfactory.

3. Instrumentation and Analysis Methods

3.1 Confocal Microscopy

The microfluidic-chip and the manifold assembly are mounted on an inverted optical microscope (Olympus America Inc. IX51, Center Valley, PA) adapted for confocal microscopy. This microscope is also used in a standard wide-field mode for alignment and testing purposes. For a typical experiment the center channel reservoir holds the protein in solution with a high concentration denaturant, usually 6 M guanidinium hydrochloride (GdnHCl), and the side channel reservoir holds a solution of diluent, such as 100 mM pH 7 potassium phosphate buffer (KPi). Although both solutions are clear, 6 M GdnHCl has a much higher index of refraction than that of the buffer, 1.434 compared to 1.336 for 100 mM KPi, making it possible to observe a jet through the microscope with the naked eye and thus be able to test the quality of the current microfluidic-chip and verify debris or protein aggregation as causes for jet degradation. The microscope is equipped with a UV optimized CCD video camera (Sony XC-EU50, Tokyo Japan) that is particularly well adapted to observe the presence of a microfluidic jet by the difference in the index of refraction between the center and side channel solutions.

To measure tryptophan fluorescence with an optical microscope, the simplest configuration is that of an epifluorescence microscope. In this type of microscope the

excitation light is reflected by a dichroic mirror through the objective and focused onto the sample at the focal plain. The light emitted by any fluorescence in the sample at the focal plane is collected through the same objective, passed through the dichroic mirror and focused by the eyepiece into an image. There are drawbacks however to using epifluorescence microscopy. It is necessary to illuminate the entire field of view with the excitation light, which can be very difficult to do uniformly with a UV light source, especially at the intensities necessary for tryptophan fluorescence. Also, by illuminating and imaging the entire field of view, backscatter and fluorescence of nearby objects either above or below the focal plane drastically increase the background noise and lower the resolution.

By adding a few additional elements, it is simple to convert an epifluorescence microscope to a confocal microscope. First, by using a collimated light source, optimally a laser, it is possible to illuminate the sample only within the small focal volume of the objective. By using an infinity-corrected objective, the emitted light collected by the objective is also very close to collimated and can be collected by a second lens following the dichroic mirror instead of an eyepiece. Most importantly, by placing a pinhole at the focal plane of the second lens it is possible to select only the light emitted within the focal volume of the objective and discard any light outside of the focal plane. Finally, a detector following the pinhole measures the light intensity of the fluorescence within the focal volume. By incrementally moving the sample, it is possible to raster an image in 2D or 3D. As an added advantage, the detector used for a confocal microscope can be much simpler than that of an optical microscope, since it only has to measure the total intensity collected over an arbitrarily large surface area and does not have to create an image itself,

unlike the CCD array detectors used in optical microscopy. The resolution of a confocal microscope is limited by the size of the confocal volume of the objective and by the size of the pinhole.

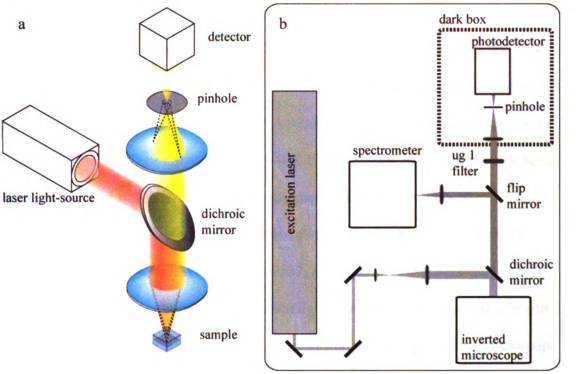

Figure 3.1.1 a) Diagram showing a simplified laser confocal microscope. The red beam denotes the excitation laser and the yellow beam shows the light collected from fluorescence within the sample. The lower set of dotted lines show light emitted from fluorescence outside of the desired focal plane inside the sample and the upper set of dotted lines show the same emitted light excluded due to the pinhole, allowing only light from the confocal volume to pass on to the detector. b) Diagram of the UV confocal system used in the Lapidus lab. The system is capable of taking either intensity measurements using a photodetector or spectral measurements using a spectrometer. The ability to switch between the two measurements is provided by a switchable flip-mirror shown above.

Excitation light is provided by an argon ion laser (Cambridge Laser Laboratories Lexel 95-SHG, Freemont CA) tuned to the 514.5 nm wavelength band and subsequently frequency doubled by a BBO crystal (Beta Barium Borate: BaB_2O_4) to emit a beam tuned to 257 nm and the TEM_{00} mode. The laser is typically power limited to output at

10 mW measured at the exit of the laser, which translates to about 4 – 5 mW when measured directly above the microscope objective. Upon exiting the laser the beam is approximately a Gaussian profile about 2 – 3 mm in diameter and is then widened by two telescoping lenses to a width of about 8 – 10 mm.

The excitation beam is reflected 45° by a dichroic mirror directly into the back port of an inverted microscope adapted for confocal microscopy. The microscope is equipped with a high numerical aperture (NA = 0.50) air-gap 40X objective (Optics for Research division of Thor Labs OFR LMU-40X-UVB, Verona NJ). The objective has a focal spot diameter of 1 μm and a working distance of 1 mm. For confocal measurements, light both enters and exits through the same back port. The dichroic mirror (CVI Melles Griot TLM1-250-45-P-0537, Albuquerque NM) necessary to separate the excitation beam from the emission light has a reflective cutoff wavelength of 300 nm, which reflects the excitation beam directly into the back port of the microscope but allows all emission fluorescence to pass through to the detectors.

Two complementary translation stages have been installed onto the top of the microscope for sample positioning. The topmost translation stage is a nanopositioner (Mad City Labs Nano-LP100, Madison WI) and is a necessary component for most confocal microscopy setups. It is responsible for rapidly moving the sample in a raster pattern necessary to create confocal images. The nanopositioner is driven by piezoelectric crystals that expand and contract depending on an applied electric voltage, yielding a motion mechanism that is both very fast and highly repeatable. By measuring the capacitance of the gap created by the crystal expansion between the moving and fixed parts of the positioner, the controller (Nano-Drive, Mad City Labs) can calculate the

position of the stage with high precision and drive the nanopositioner in closed-loop mode. The positioner has a travel distance of 100 μm in X, Y, and Z directions and is able to resolve distances to nanometer resolutions. The microfluidic-chip manifold assembly fits snuggly onto the top of this positioner.

Between the nanopositioner and the microscope itself is an electromechanically screw driven translation stage (KL-Series 12-6436, SEMPREX Corp Campbell CA). The mechanical positioner is controlled by computer and has a large travel distance of 6 cm × 4 cm in the horizontal and vertical directions with micron resolution. This stage is used for rough positioning, such as for centering the chip in the field of view, and to take multiple images along the length of the jet throughout the 500 μm long observation region of the microfluidic chip.

The confocal setup is capable of measuring two different kinds of observables, provided by two different detectors and fully described in Lapidus et al. (*77*) and Waldauer et al. (*78*). It is possible to choose between the two different setups by switching a motorized flip mirror positioned immediately following the dichroic mirror.

The first observable measured is raw fluorescence intensity, which is detected by a GaAsP photocathode PMT photon counter (Hamamatsu H7421-40, Japan). The detector is housed in a dark box following a 50 mm focal length convex lens and a 100 μm diameter pinhole. The pinhole is mounted on a motorized two directional micrometer positioner (Newstep ANS12, Newport Corp Irvine CA) coplanar with the face of the pinhole and is remote controlled to allow the intensity signal to be optimized without opening the dark box. Because the photon counter has no wavelength selectivity, it is highly sensitive to stray light, so a bandpass filter with a center wavelength of 360 nm

(UG1) is typically used inline with the fluorescence light immediately before it enters the dark box. In addition to being placed inside a dark box, the entire confocal microscopy setup is located inside a dark room and all stray light is kept to a minimum during an experimental run.

The other setup is capable of spectroscopic measurements of the emitted light. These measurements are taken with a spectrometer comprised of a monochromator (MicroHR, Horiba Instruments Inc, Irvine CA) with a 1200 hash/μm grating in conjunction with a linear array CCD camera. The total setup is able to provide spectra with a 300 - 440 nm range. Following the flip-up mirror described previously, a convex lens with a focal length of 33 mm focuses the light to the entrance slit of the monochromator. The adjustable width slit at the entrance of the monochromator acts as the "pinhole" of the confocal setup. Two different CCD cameras have been used with this instrument. The first, a Sygnature-CCD-3648-VIS (HORIBA Scientific, Kyoto Japan) had a room temperature CCD sensor comprised of a 3648 pixel linear array and was used until 2008 when it was replaced with an iDus 420A-BU (Andor Technology, South Windsor, CT) due to problems with low sensitivity and a nonlinear wavelength response. The sensor on the new camera has a 1024 by 225 pixel CCD array and is cooled to between -20 and 0 C to greatly lower electronic noise.

3.2 UV Fluorescence Measurements

UV Fluorescence Intensity Data Acquisition

A central computer (Optiplex 170L Dell Corp, Round Rock TX) running LabVIEW 7.1 (National Instruments Corp, Austin TX) on Windows XP (Microsoft Corp,

Redmond WA) controls all data acquisition. The computer interfaces with the pressure box through an A/D converter card (PCI-6602 National Instruments) both setting and reading center and side channel pressures. Communication with the nanopositioner is through a second A/D converter card (PCI-6221 National Instruments). A digital counter card (PCI-DIO-96, National Instruments) interfaces with the photon detector. The spectrograph CCD camera interacts directly with the computer through USB either through LabVIEW virtual instruments (VIs) of our own design or though acquisition software provided by the CCD manufacturer. The mechanical positioning stage controller interfaces with the computer via a serial connection and is controlled by AMICron Motion Control Software (Semprex Corp, Campbell CA), which is then interfaced within LabVIEW VIs through macros written in MacroExpress (Insight Software Solutions, Kaysville UT).

Photon counter (intensity) measurements are taken with a VI called SCANMIXER. The VI controls the nanopositioner, the mechanical positioner and the pressure settings and takes readings from both the photon counter as well as instantaneous pressure readings from the pressure box. The program is used to raster intensity images taken through a series of photon counter readings.

The VI used to take spectral data is called SpecAQ and is capable of measuring the emission spectra of a protein or fluorescent molecule at any point along the microfluidic jet as well as controlling the center and side pressures. By its nature, a spectrograph reading taken with a CCD camera is much noisier than a reading taken by the photon counter used to take intensity measurements. Each spectrograph reading must therefore be time integrated much longer than that of a photon-counter reading, typically

for at least a full second per spectra versus 10 ms per reading taken in the SCANMIXER VI. Thus SpecAQ is limited to taking only linear series of measurements, rather than fully scanned images.

Fluorescence Intensity Analysis

A typical individual photon-counter scan covers an area of 10 x100 μm and yields an image that is 41 pixels across by 51 pixels high, saved to an ASCII file about 12 KB large. In order to measure the intensity decay over a time window covering 500 μs at a single flow-rate, it is necessary to take a set of 4 – 6 successive scans yielding about 10,000 different individual photon-counter intensity readings. In a given image, the vast majority of the individual intensity readings are taken in locations in the observation channel away from the location of the jet and their corresponding pixels only show experimental background light and electronic noise.

The pixels showing the actual tryptophan fluorescence are selected from the image and then processed into a more useful data form through an analysis software suite I wrote to work with MATLAB (MathWorks, Natick MA). The program is able to determine the location of the jet within a given image and output a column of intensity values, each calculated from the intensity of a single pixel along the center of the jet, summed with an additional number of pixels in the same row to the left and right of the center pixel, all corresponding to the same time after mixing. The positions of each intensity value along the jet are also converted into time after mixing and output to a second column by taking the distance of each point from the t_0 location, determined in the first image taken from known landmarks designed into the chip geometry, and dividing by the flow velocity as calculated from the set pressure ratio.

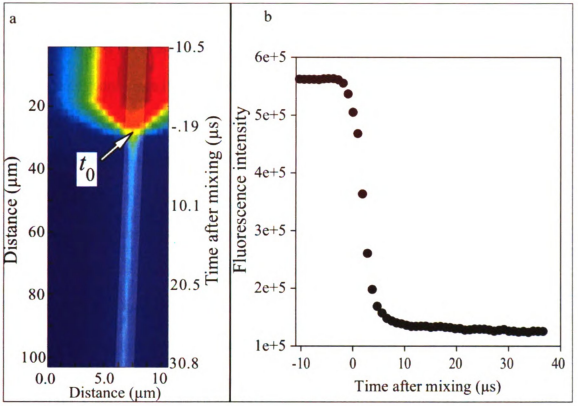

Figure 3.2.1 a) Raw intensity scan showing the mixing region and the first 70 μm of the microfluidic jet. The pixel corresponding to the start of mixing (t_0) is determined from landmarks visible in the supply channel (not indicated). The distances are converted to times as shown on the right vertical axis; by incorporating the microfluidic flow velocity calculated from the chip geometry and the applied pressures. b). Fluorescence versus time can be calculated from the raw intensity data. The pixels within the overlaid region in the raw intensity data are summed in each row to determine the intensity as a function of distance along the jet. Because the supply channel is much wider than that of the jet, there is an enormous drop in the overall intensity after mixing and must be corrected by normalization. Note that a fluorescence decay is still visible from ~ 7 μs onward that is not rooted in artifacts from the chip geometry but is a result of the protein in the jet starting to fold.

Because of the nature of the experimental setup, many intrinsic features of the microfluidic-chip design as well as defects in individual chips appear as artifacts in an intensity-versus-time plot. A major artifact is caused by the narrowing of the supply channel upon entering the mixing region and the later widening of the jet along the exit channel, which manifests as a rapid decrease in intensity at t_0 and a gradual increase in intensity with increasing time. Bumps in the bottom or sidewalls of the observation

channel alter the flow of the jet, causing small deviations from a straight centerline. These effects will show as abrupt changes in intensity once the data is converted from the raw intensity scans since the analysis software assumes a linear jet. Since these effects are not necessarily linear and are intrinsic to the experiment itself, they cannot be easily corrected mathematically or by simulation. However, it is possible to correct for them experimentally by normalization.

In order to normalize a dataset, it is necessary to take an additional set of measurements under the same conditions as the original dataset, preferably on the same day, but instead of mixing the protein solution into a diluent with no denaturant; the side channel solution has the same denaturant concentration as that of the protein sample solution. In this control measurement, the protein should remain unfolded all the way through the microfluidic chip. Any changes in the measured intensity should be only a result of measurement artifacts. Dividing the original dataset with the control dataset at each individual time point produces a normalized dataset.

An additional correction used to ensure the quality of the data is that all measurements are taken with at least two and usually three different flow velocities. If a measured decay is actually an artifact of the mixing properties or defect that is not visible in the control experiment, the changes in fluorescence should only have a dependence on the position within the chip and not the time after mixing.

The mixing time is defined as the time it takes for the concentration of denaturant to drop from 90% to 10% of the original concentration. Mixing occurs within the first few microns of the mixing region and the time is an intrinsic property of the design of the mixing chip. The distance that the mixing takes place is generally similar for a given

design at a given pressure ratio, regardless of the overall flow velocity. This means that for an optimum pressure ratio, the mixing time will decrease with higher flow velocities. Therefore, any early intensity data from within or near the mixing time, especially if taken at a low flow velocity, is suspect of being an artifact. By flowing at more than one fluid velocity, we are able to work around this artifact that cannot be corrected by normalization alone.

It is possible to measure the mixing time of a microfluidic chip at a given flow-rate directly. Potassium iodide (KI) is an efficient quencher of tryptophan fluorescence and by mixing free tryptophan molecules in the form of N-acetyl-tryptophanamide (NATA) into KI, the fluorescence intensity drops sharply within the mixing time. It is important to divide out this data set with a non-quenched set in order to correct for the microfluidic chip geometry, much in the same manner that a folding dataset is divided by a non-folding dataset as described above. The fastest mixing time of the most recent direct measurement for the current microfluidic chip design was 14.7 μs when flowing at 1.5 m/s and using a flow-rate of 50:1 side to center ratio. When using the looser mixing time definition of the time from 90 – 30% of the initial concentration, this time decreases to 4.0 μs.

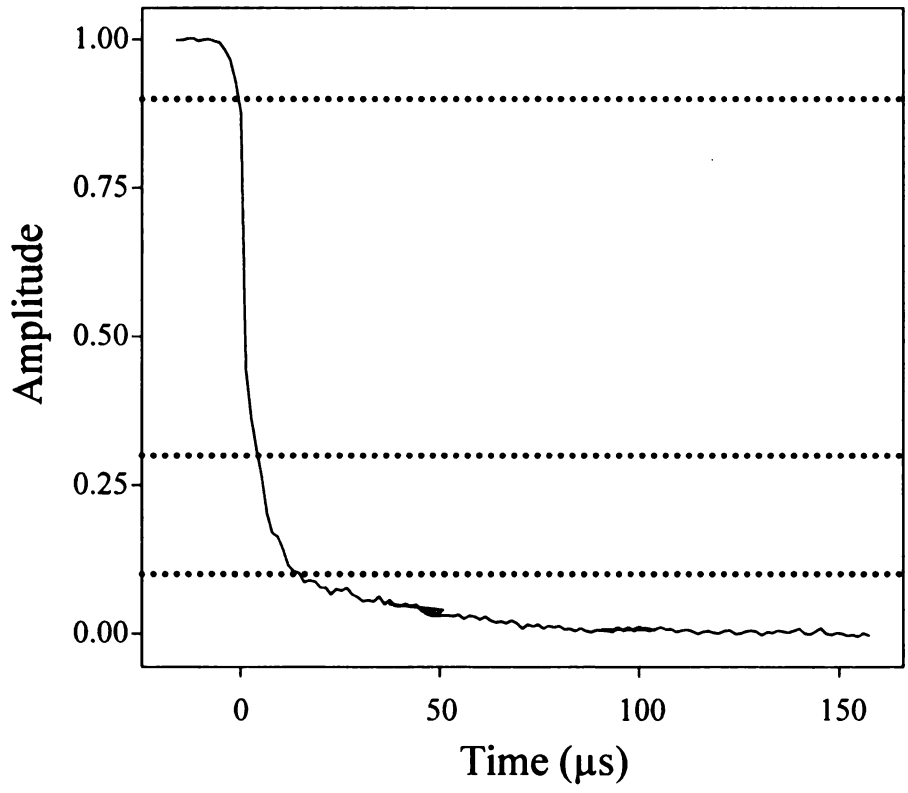

Figure 3.2.2 Plot of the relative fluorescence intensity 500 μM NATA mixed into 400 mM KI at a flow rate of 1.5 m/s and a flow ratio of 50:1 KI:NATA solutions. The plot has also been renormalized such that the initial amplitude is one and the final amplitude is 0. The top dotted line is at 90% of the initial intensity, the second is at 30% and the bottom is at 10%. The time for the fluorescence to decay from 90% to 10% is 14.67 μs and the time to decay to 30% is 4 μs (*79*).

Fluorescence Spectra Analysis

A typical spectral measurement series is comprised of 51 individual spectral measurements, taken at evenly spaced intervals along a 100 μm long length of the microfluidic jet within the observation channel of the microfluidic-chip. Each spectral measurement contains either 3648 or 1024 wavelength dependent intensities depending on whether the measurements were taken with the old or new CCD cameras described in section 3. A full data set can total a few MB in size.

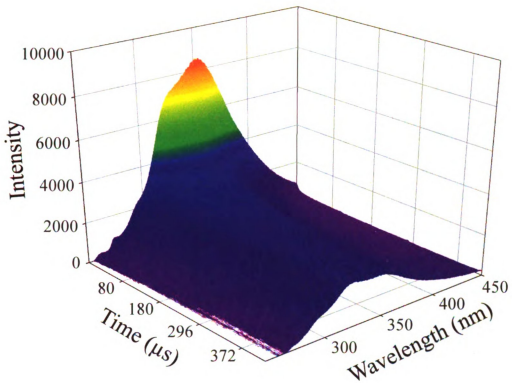

Figure 3.2.3 A full spectral dataset taken for Lambda Repressor. It is made of over 150 individual spectra taken along almost 300 μm of the observation channel corresponding to over 500 μs.

There are many ways to condense such a large data set to a more manageable size and determine important kinetics. Many of these methods involve throwing out much of the seemingly less important intensities and focusing on a small set of wavelengths or just the wavelength of the overall maximum for the entire spectra. A more efficient way to analyze the time evolution of an entire spectra measurement, using the entire set of wavelength dependent intensities, is to use singular value decomposition (SVD).

SVD is a factorization process for rectangular matrices very similar to that of eigenvalue analysis for square matrices. The SVD of an $m \times n$ matrix $\mathbf{A}$ is defined as

$$\mathbf{A} = \mathbf{USV}^{\mathbf{T}}, \tag{3.1}$$

where **U** is an orthonormal $m \times m$ matrix and **V** is an orthonormal $n \times n$ matrix. **S** is an $n \times n$ diagonal matrix containing the singular values, ordered such that $s_1 \geq s_2 \geq \ldots \geq s_n \geq 0$.

According to Beer's law, the measured spectrum at time t_j of a system of N_S spectrally distinguishable species (e.g. a spectral shift and an overall change in intensity) can be described as a linear combination of the spectra of the individual species (*80*):

$$A_{ij} = A(\lambda_i, t_j) = \sum_{n=1}^{N_s} f_n(\lambda_i)\, c_n(t_j) \ , \qquad (3.2)$$

where A_{ij} is an element of the measured spectrum. This can be rewritten as:

$$\mathbf{A} = \mathbf{F}\mathbf{C}^{\mathbf{T}} \ , \qquad (3.3)$$

where **F** and **C** are matrices consisting of the set of N_S column vectors that make up either the time evolution or spectra of the individual species. This equation bears a striking resemblance to equation 3.1 and, if **A** is noise free, the SVD of **A** differs from this representation only by normalizing **F** and **C** and introducing the multiplicative factor in the singular values. In this case the $\mathbf{S}_i = 0$ for $i > N_S$. When noise is present, it is effectively separated out into the vectors for $i > N_S$ and the corresponding singular values are nonzero but much lower than those for the first vectors.

Computing the SVD of a large matrix representing real data was exceedingly difficult until 1965 when Golub and Kahan first discovered an algorithm that makes it very simple on modern computing systems (*81*).

One of the experiments where the use of SVD has been demonstrative is the folding study of the protein Lambda Repressor. The SVD of the time resolved spectra, as shown in Figure 3.2.4, has 4 significant components. The first two components had singular values two orders of magnitude larger than all of the rest. The first basis vector is basically the same shape as the average measured spectrum and its time resolution is shown in the first amplitude vector. From the plot it is visible that this means there was an exponential-like decay in the overall intensity. The second basis vector shows a wave-like shape, which is negative on the left and positive on the right. This represents a shift over time of the real spectra from red to blue. Looking at the time evolution in the second amplitude vector, we can see that the spectral shift occurs with an exponential decay. Most interestingly, the decay rate for the spectral shift and that for the overall intensity were not the same which was interpreted as evidence of downhill folding (*79*). One of the defining characteristics of downhill folding is that different probes will exhibit different kinetics (*82*).

The next two basis vectors show what could be other signals, however their singular values are two orders of magnitude smaller than the first two and most likely reflect artifacts in the measurements. This is most evident in the time evolution aplitude vectors which show large jumps at the positions where the mechanical stage was moved to a new section of the chip observation window. Also interesting is the fifth component of the SVD, which selected out the signal from one stuck pixel of the CCD during a single spectral measurement about 600 μs after mixing.

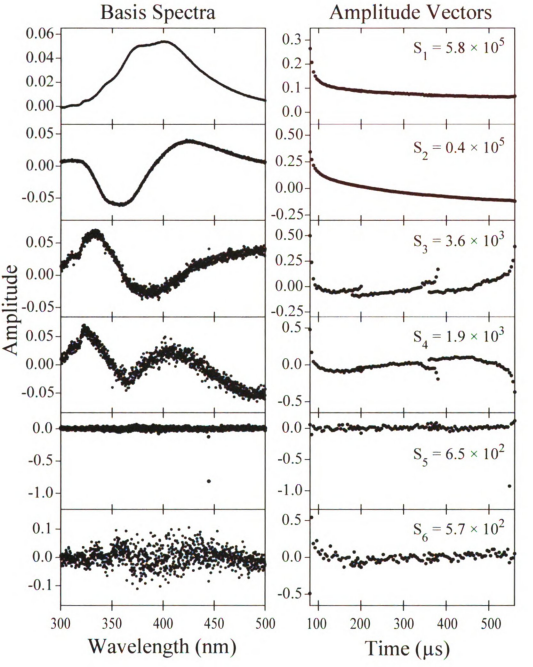

Figure 3.2.4 Plots showing the first 6 components of the SVD of the protein Lambda Repressor spectra raw data shown in **Figure 3.2.3**. The first component clearly shows a decay in the overall intensity. The second component shows a spectral shift. Note that all the significant signals have been selected out by the first 4 components and that all the higher components have much lower singular values and only contain noise.

3.3 Trp-Cys Contact Quenching Mixer Experiments

Trp-Cys Contact Quenching Mixer Instrument

The microfluidic-mixing version of the Trp-Cys contact quenching instrument sits on the same optics table as an equilibrium instrument, and shares the same lasers and most of the same electronics. It is possible to switch between the two different measurements by flipping only two mirrors.

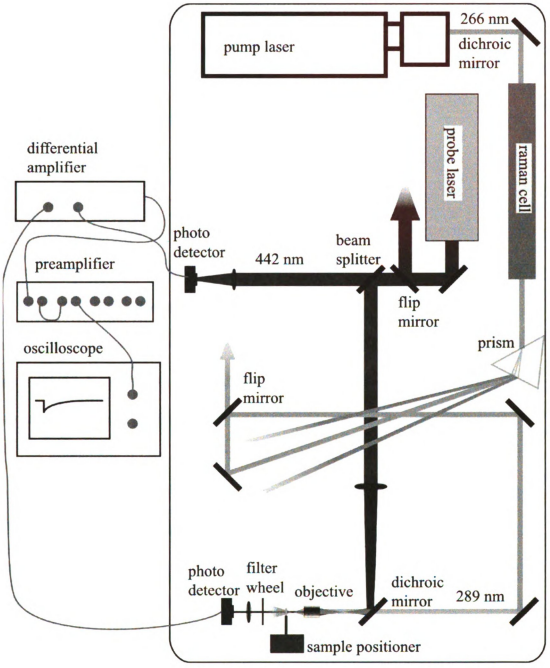

Figure 3.3.1 The Trp-Cys contact mixing instrument is on the same table as the equilibrium instrument and shares many of the same components. It is possible to switch between the two instruments by toggling two flip mirrors, as shown by the beams terminated with arrowheads.

Light for the pump beam is provided by a Q-switch pulsed Nd:YAG laser (Continuum Surelite II-10, Santa Clara CA). The primary 1064 nm beam is frequency doubled twice, yielding a 266 nm output beam. The laser has a repetition rate of 10 Hz

and measures about 0.1 W of power exiting the frequency doublers. Because much of the light emitted from the laser is escaped light from the original and first doubled wavelengths, the first mirror following the exit of the laser is dichroic and selects out the desired 266 nm light.

Although tryptophan will fluoresce when excited with light of 266 nm wavelength (257 nm light provides the excitation light for the fluorescence mixer) it is not adequate for Trp-Cys quenching experiments because it has a very low quantum yield for triplet state excitation (*27*). It is however a very effective wavelength to induce photodamage in tryptophan. By using a wavelength closer to the optimum excitation wavelength of 280 nm it is possible to lower the laser power, yet obtain the same signal level. This in turn lessens photodamage to both the protein molecules and to the microfluidic chip. A lower pump laser power also lessens other unwanted effects such as thermal lensing.

A Raman cell (Light Age 101 PAL-RC, Somerset NJ) is used to shift the wavelength of the excitation light from 266 to 289 nm. The cell is composed of a steel tube filled with high-pressure (1500 psi) methane gas and a window on both ends. Light entering the tube scatters inelastically with the methane molecules, transferring energy to and from the molecules in multiples of the different allowed vibrational or rotational modes. The spectrum that exits the cell is comprised of the primary 266 nm light as well as the first few Stokes and anti-Stokes lines. A quartz Pellin-Broca prism placed in the beam line immediately following the cell is used to refract the emitted spectrum; the first Stokes band with a wavelength of 289 nm is selected across the other side of the optics table.

The probe beam source is a CW He-Cd laser (Kimmon Koha Co. LTD IK4101R-F, Tokyo Japan) that outputs a 442 nm wavelength Gaussian beam about 1.2 mm in diameter. In order to cancel out any variations in the probe laser power, the beam is divided in two by a beam splitter and one of the beams is sent directly to a reference photodetector. The other beam is used for measurements with the reference signal voltage subtracted out electronically in a later step. The photodetectors used in this instrument (1621 Nanosecond Photodetector, New Focus, San Jose CA) are fast Silicon/PIN type, have a time resolution of <1 ns rise-time and a flat frequency response curve from DC to ~ 200 MHz. It is important to have the baseline light intensity at both detectors matched as close as possible such that almost all of the DC component can be subtracted out. This is accomplished by placing a variable neutral density filter wheel in front of the signal detector, which usually has the higher overall intensity.

A 300 MHz digital oscilloscope (TDS 3032B, Tektronix, Beaverton OR), externally triggered by the pump beam laser to take one reading per pulse digitizes the analog voltage signals. The oscilloscope has a large data buffer and is capable of averaging up to 512 readings in internal memory in order to average out any noise or fast oscillations in the probe beam.

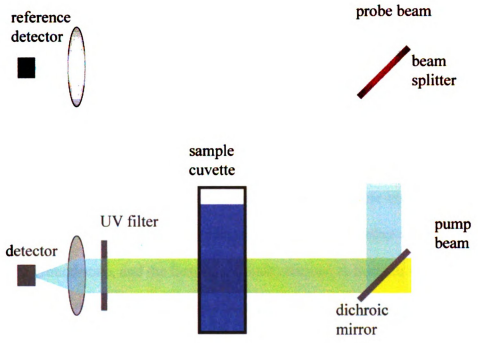

Figure 3.3.2 The setup for an equilibrium Trp-Cys contact quenching experiment (*29, 31, 83*). In this experiment, the sample protein solution is placed in a temperature-controlled quartz 1 cm path length cuvette. In order to measure Trp-Cys contact quenching, the probe and pump beams must be collinear and pass through the same sample volume. This is accomplished by using a dichroic mirror. The signal is obtained by subtracting the voltage measured at the reference photodetector from the voltage read at the measurement detector.

Adapting the equilibrium Trp-Cys contact-quenching instrument to enable microfluidic mixing experiments adds many additional layers of complexity. One of the most immediate issues is that of the optical absorbance path length. With current fabrication techniques, it is not possible to etch channel depths greater than 40 μm deep – this yields a path length 250 times shorter than that for the 1 cm cuvette used in equilibrium experiments. It is therefore necessary to add two additional levels of electronic signal amplification. The first level is provided by a high performance 100 MHz differential amplifier (Lecroy Corp. DA 1853A, Chestnut Ridge NY), which performs the reference subtraction and has a maximum gain of 10 ×. The second stage of amplification is provided by a 4 channel 350 MHz preamplifier (Stanford Research

Systems SR445A, Sunny Vale CA). Each of the independent channels provides a gain of 5 with a maximum peak-to-peak input of 400 mV. Generally the first channel is used and often the second as well, yielding a total gain of 50, or 250 when using both amplifiers.

The microfluidic mixer adds many additional constraints. Inside the observation region, a pulse of the pump beam must illuminate a small volume of solution in order to excite the protein tryptophan residues to the triplet state. That same excited volume must also be illuminated by the probe beam in order to observe its member molecules as they return to the ground state, and the instrument must continue to monitor this volume even as it flows through the microfluidic chip observation channel. It is therefore important to have the probe beam diameter set much larger than the pump beam. In this manner, the small excited volume stays within the probe illumination over the time if takes for the flow to traverse the probe beam diameter. For example, if the probe beam diameter is 100 μm and the pump beam is 1 μm and the flow-rate inside the observation channel is 1 m/s, then the total window available to observe the tryptophan triplet state absorbance is 100 μs long. If the beams are aligned such that the pump beam is aligned directly in the center of the probe beam only half of the window would be available, providing only 50 μs before the tryptophan molecules originally excited to the triplet state by the pump beam travel out of the volume illuminated by the probe beam.

In order to produce these beam diameters, additional optics are necessary in comparison with the equilibrium experiment. The most crucial optic is the addition of a UV objective (Objectives for Research LMU-3X-266, Cantwell NJ). The 3X objective has a working distance of 49 mm and is capable of focusing the beam to a 5 μm diameter spot at the focal point. By focusing the probe beam onto the backplane of the objective,

the emitted light is a tight collimated beam. The beam diameter can be determined from the ratio of the object and focusing lens focal distances (60 mm for the objective and 250 mm for the focusing lens) and is estimated to be about 60 μm.

One of the most important adjustment parameters is the distance between the microfluidic chip and the objective. It is important that the pump beam diameter be as small and uniform as possible in order to achieve a high time resolution, which means moving the chip as close to the focal point as possible. It would seem best to orient the chip such that the focal point is in the center of the channel. It turns out however that this is also the location in the beam with the highest energy density, much too high for the fluid and exceedingly dangerous to the chip as well. If the chip is placed too close to the focal point the interior surface of the channel or the surface of the chip can be ablated with just a few pulses and the entire channel can be compromised within a minute of pump beam illumination. After much experimentation, the optimum orientation was found to be with the focal point just in front of the surface of the chip, ensuring a pump beam diameter inside the channel of 5 – 10 μm and no damage to the microfluidic chip.

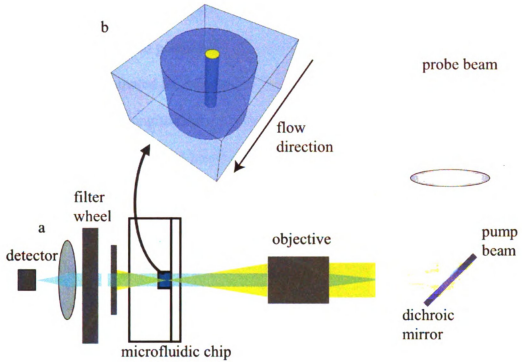

Figure 3.3.3 a) A detailed schematic of the Trp-Cys microfluidic mixer instrument. The probe beam is focused unto the back plane of the microscope objective and is made collinear with the pump beam through the use of a dichroic mirror. The probe beam exits the objective as a collimated beam with a diameter of about 100 μm. The pump beam is focused into the center of the probe beam and a few microns in front of the surface of the chip and passes through the center of the microfluidic channel. The probe beam is then focused and collected by a detector. b) A schematic showing a sample volume of test solution inside the microfluidic chip observation channel. The large blue cylinder corresponds to the probe beam volume and the small yellow cylinder to the excitation volume.

The small pump beam diameter has the added advantage of increasing the time resolution of the instrument by exciting a smaller local volume of protein molecules which all have had similar trajectories through the mixer and similar times since their local denaturant concentration was abruptly decreased during mixing, allowing refolding. For example, with a pump beam diameter of 1 μm and a flow-rate of 1 m/s, all of the tryptophan molecules will have the same time after mixing (within ± 1 μs) throughout their passage through the probe beam. Therefore the time resolution is much closer to 1 μs even though the probe beam time window is 50 – 100 μs long.

The microfluidic chip manifold is mounted on a computer controlled mechanical stage, which is necessary to position the microfluidic chip in the probe and pump beam path. The stage is automated for motion in the plane normal to the beam and can also be adjusted by hand in the longitudinal direction to position the chip correctly with the pump beam focal point. The automated positioners are driven by a piezo-actuator mechanical screw drive (Picomotor model 8301, New Focus, San Jose CA) capable of 10 nm step increments. The actuators are used in a closed-loop configuration with an optically encoded translation stage with 12.5 nm resolution (9066-COM-E, New Focus), much less than the uncertainty due to other conditions such as the size of the pump and probe beams.

The entire instrument is controlled via a data acquisition computer. The computer interfaces with the pump beam and is able to control the shutter as well as the Q-switch delay (laser power), the oscilloscope via GPIB, the syringe pumps and the sample positioner. All of these aspects are automated and the data collected through a suite of LabVIEW VIs.

Trp-Cys Measurement Data Acquisition and Analysis

When starting with a newly mounted microfluidic chip, or following a drastic change in the instrument's optical alignment, it is necessary to map the microfluidic chip in order to be able to translate between the micron stage position settings and the actual location of the mixing and observation regions inside the chip relative to the probe beam. This is accomplished by taking an absorbance scan of the mixing and narrow observation regions of the chip while flowing 10 mM Fluorescein (Sigma-Aldrich, St. Luis MO), a highly absorbent fluorophore (absorbance maximum at 238 nm, $\varepsilon = 39.8\ mM^{-1}cm^{-1}$, and

additional maxima[4] at 460 and 493 nm) through the channels. Although, due to the large probe beam diameter, the image is not nearly as sharp as those taken with confocal microscopy, it is still possible to discern the chip geometry and determine the positions and t_0 location in the microfluidic chip.

[4] Taken from the Fluorescein product information page courtesy of Sigma-Aldrich. http://www.sigmaaldrich.com/etc/medialib/docs/Sigma/Product_Information_Sheet/f7505pis.Par.0001.File.tmp/f7505pis.pdf

Figure 3.3.4 a) A close-up optical absorbance scan of the serpentine mixing region filled with 10 mM Fluorescein shown with the chip geometry overlaid. The total scan area is 1000 μm by 300 μm with each pixel measuring 100 μm wide by 10 μm high. b) A scan showing the entire narrow observation region. The scan measures 3 mm long and 300 μm high.

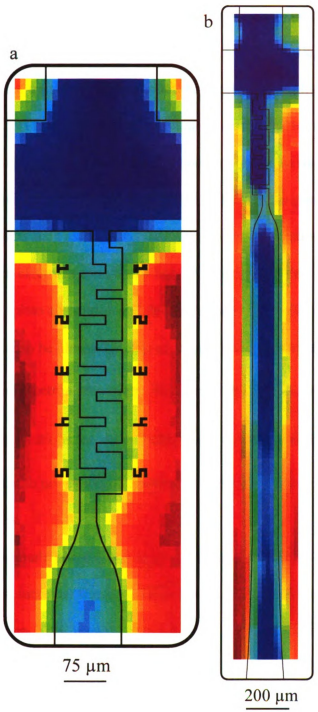

Figure 3.3.4

After the chip has been mapped it is possible to optimize the instrument by taking triplet lifetime measurements of NATA flowing through the microfluidic mixer. Optical excitation of tryptophan transiently excites both the singlet and triplet states, however the singlet state is very short lived, on the order of nanoseconds. The lifetime of the triplet state is much longer, about 40 – 50 μs, which is comparable to the time it takes for a NATA molecule to exit the probe beam diameter. Excitation also generates additional undesired photoproducts such as hydrated electrons and neutral radicals that can be problematic. Hydrated electrons can absorb light at wavelengths that overlap with the triplet → triplet tryptophan absorption and decay within ~ 3 μs following the pump beam pulse. This amplitude can be almost entirely eliminated however by degassing the solutions with N_2O, an electron scavenger. We have found that it is most effective to bubble the side buffer solutions for an hour until they are fully saturated with N_2O. After bubbling it is important to not expose the solutions to the atmosphere, which necessitates using gastight syringes.

Another problematic photo-effect is thermal lensing, in which some of the power dissipated inside the solution by the pulse beam changes the local density and index of refraction of the solution. This, in turn, causes the probe beam to slightly deflect and move across the detector. The effect resolves on the millisecond timescale as heat diffuses out of the probe volume and by flowing the solutions much of the thermal lensing seen in the equilibrium experiments is avoided. However, it will also often appear as an acoustic effect in the first 200 – 400 ns. Thermal lensing can be lessened by decreasing the power of the pulse beam and by adjusting the optics of the pulse and probe beams. Some of the more effective adjustments include changing the position of the

detector and focusing the probe beam to a smaller spot on the detector, which can allow movement of the beam without affecting the measured intensity.

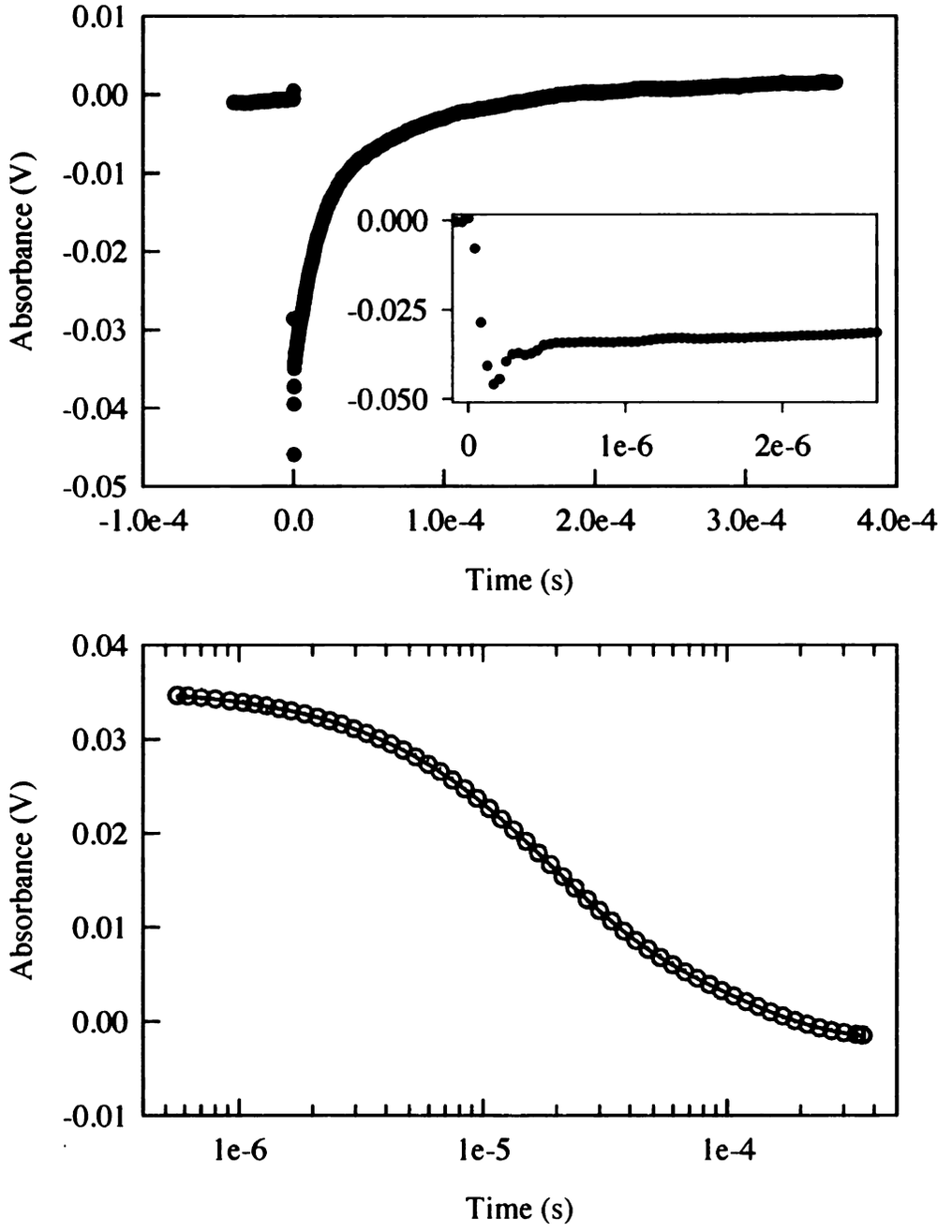

Figure 3.3.5 Tryptophan triplet absorbance decay of Protein L during the first 300 μs following mixing from 4 to 0 M GdnHCl in 17 % sucrose solution. Upper plot shows the raw voltage as measured by the oscilloscope immediately following the differential amplifier and inset shows a 2 μs window including the pulse, where thermal lensing is clearly visible. Bottom plot shows the data after they have been inverted, logarithmically binned in time and curve fitted to a double exponential (shown as the solid line), with the points preceding the pulse and the first 100 ns removed.

The absorbance signal is measured by a digital oscilloscope following a differential amplifier that compares the voltage of the reference detector and the probe detector and adds gain. The pump beam laser triggers the oscilloscope externally to start recording about 1 – 10 μs before the pulse and record for 400 μs, which is about 4 times longer than any excited molecules would remain inside the probe beam diameter. Any pre-pulse data are useful to determine the baseline voltage. By looking at the first 400 ns it is possible to adjust the optics to maximize the signal and minimize any thermal lensing or at least to restrict it to the earliest points.

Once the instrument has been optimized with NATA measurements, it is ready to measure an actual protein sample. For real measurements, the oscilloscope is set to average 256 readings, greatly reducing any noise resulting from a single pulse of the pump beam or present in the probe beam (see upper panel of Figure 3.3.5). The measurement files are prepared for curve fitting by first removing all the points prior to the decay and any early thermal lensing; then the remaining data are logarithmically binned, which greatly reduces much of the electronic noise that may have remained following averaging. Lastly, the data are inverted and analyzed through curve fitting software such as TableCurve 2D (SYSTAT Software, Chicago IL) as shown in the lower panel of Figure 3.3.5.

There are a few notable sources in this instrument for systematic error. Individual data points can be greatly affected by thermal lensing as discussed previously, which can greatly affect curve fitting. Longer-lived decays, such as the natural decay of the triplet in a fully folded protein, can be distorted by the additive effect of a non-exponential decay caused by the excited molecules exiting the probe beam volume. This artificial decay can

also be affected by uncertainty in the location of the pump beam in relation to the probe beam. If the probe beam or many of the other optical elements are adjusted after the chip has been mapped, any position data may be suspect and contribute to error in the time after mixing. The map itself, due to the large diameter of the probe beam used during the scan, contributes to a ~ 10 – 20 μm uncertainty (about one or two pixels in a typical scan) as to the location of the initial measurement. It is difficult to assign an exact time after mixing to measurements taken between the mixing region and the observation window, where the channel is widening exponentially from 30 – 120 μm, because the flow velocity is changing as a function of the width.

For measurements taken inside the 120 μm wide observation channel, the uncertainty in time for any measurement would be the sum of the uncertainties from the placement of t_0 (± 20 μm) and the flow velocity arising from any uncertainty in the depth of the etched channel (± 5% of the measured value). The uncertainty of individual positions in relation t_0, about 80 nm, which is the resolution of the optically encoded stage, is negligible in comparison with other uncertainties. Because the pump beam is occasionally adjusted to optimize the signal or to diminish thermal lensing, there is a small contribution in the uncertainty for t_0 or any measurement taken subsequent to pump beam adjustment, however any large changes in alignment will extinguish the signal. Therefore, the uncertainty in the location of the pump beam can be estimated to be about 5% of the diameter of the probe beam or about 5 μm. For a chip with a measured depth of 40 μm and a volumetric flow rate of 300 μl/min (1.04 m/s in the observation region), the maximum total error in any time measurement would be 20.8 μs (error from mapping,

assuming 20 μm long pixels) + 5.2 μs (uncertainty due to pump beam alignment) + 3.6 μs (uncertainty from channel dimensions), for a total maximum error of 21.7 μs.

4. Protein L Experiments

4.1 Introduction

Much of the experimental effort on protein folding over the last 15 years has focused on the so-called two-state folders (*84, 85*). These usually small, single-domain sequences have mono-exponential kinetics on the millisecond (or slower) timescale and the folding rate has a Boltzmann-like dependence on temperature or denaturant concentration (*86*). However, the experimental measurements of these two-state folders were limited to millisecond or longer timescales due to the limitations of stopped-flow mixing technology (*21*) as shown in section 1.4. Evidence for the absence of kinetic processes on faster timescales for a two-state folder is usually inferred only from the lack of a burst phase, or missing amplitude, during the mixing time. To study faster events, researchers have investigated secondary structure formation and hydrophobic collapse on the nanosecond and microsecond timescales, which suggest that some folding steps were possible before 1 ms (*87*). However, these experiments were primarily on model peptide or non-folding protein systems. At the same time there has been a lively debate on the validity and value of energy landscape theory to describe protein folding (*9, 11, 88*). The "new view" may allow for more complex folding paths than traditional transition state theory but seems unnecessarily complicated for describing a two-state folder.

A small number of extremely fast-folding proteins have also been studied on the microsecond time scale using laser temperature jump and have generally shown two-state behavior, but these experiments typically cannot prompt refolding from a fully unfolded

state (*89-91*). The hydrodynamic microfluidic T-mixer detailed in the previous chapter has a mixing time of just a few microseconds, which allows observation of real proteins folding from a fully denatured state on the time scale that hydrophobic collapse and secondary structure formation may be occurring (*60, 77, 92*).

The B1 domain of protein L is a common model system for studying protein folding. Initial mass spectrometry in conjunction with H*D*-exchange equilibrium experiments provided direct evidence that protein L is a two-state folder (*93*). This model was confirmed with stopped-flow mixing fluorescence and CD measurements, both of which showed single exponential decays with rates of 27.8 s^{-1} and ~ 27 s^{-1} respectively with no perceptible burst phase within the 1.7 ms dead time (*21*). Plaxco et al. (*94*) confirmed and expanded these findings by stopped-flow small-angle X-ray scattering (SAXS) measurements. They found no evidence of a rapid hydrophobic collapse of the unfolded protein following an abrupt change in solvent conditions to those favorable to folding, instead concluding that the collapse occurs concurrently to the folding process. Later H*D*-exchange experiments showed no intermediate folding state in the free energy between folded and unfolded states under native conditions (*95*). These data revealed a significant energy barrier of about 4.6 kcal mol^{-1} (*21*) between the unfolded and folded states.

After exploring the folding of protein L using Trp-Cys contact quenching in equilibrium and Trp-Cys contact quenching, UV fluorescence, and FRET in ultrarapid microfluidic mixing experiments, we found that the unfolded state of protein L is much more complex than previously thought.

Expression and purification of protein L

The protein L plasmid (Y47W), a generous gift from David Baker, is expressed by standard methods first developed by Gu et al. (*96*) with additional purification steps detailed by Yi and Baker (*93*) The K23C and T57C mutants were made and expressed as described by Singh et al (*97*). For FRET measurements, Site specific labeling of protein L with a unique donor and unique acceptor molecule was accomplished using a modified sequential labeling protocol pioneered by Haas et al. (*98*), as described in detail elsewhere (*99*). Two Cys residues were introduced into wildtype protein L by mutagenesis. One Cys replaced residue Ser16 at the base of the N-terminal hairpin, and a second Cys was added to the C-terminus (residue 65).

For the UV fluorescence mixing experiments, the protein, typically prepared in 6 M GdnHCl and 100 mM potassium phosphate buffer at pH 7.0 with a concentration of 500 μM (concentrations as low as 100 μM were used with no change in measured kinetics). All experiments took place at room temperature (23 C). The protein concentration was ~ 30 μM in all of the equilibrium Trp-Cys contact quenching experiments.

For the Trp-Cys contact quenching mixing experiments, all samples were prepared in 1 ml volumes at 1 mM concentration in 4 M GdnHCl. Because the mutant has an exposed cysteine residue, all the samples were stored at -10 C in 5 mM TCEP with an additional 50 μl of 100 mM TCEP added immediately before use in order to prevent the production of disulfide bonds. Diluent buffers used in the experiments of various GdnHCl and sucrose concentrations were always bubbled with N_2O for at least an hour,

atmospherically sealed prior to an experiment, and carefully handled in order to reduce any population of free radicals.

4.2 Equilibrium Experiments

For the equilibrium experiments, Protein L was prepared in 100 mM potassium phosphate buffer at pH 7.0 (concentration ~ 15 μM) with a series of guanidinium hydrochloride concentrations ranging from 0 – 6 M. Fluorescence spectra were taken with a SPEX Fluorolog spectrofluorometer (HORIBA Jobin Yvon, Edison NJ) excited at 280 nm and viewed between 300 and 400 nm. All measurements were taken at room temperature.

The Folding Transition

Singh et al. first performed a series of equilibrium Trp-Cys contact quenching experiments at varying denaturant concentration with two different protein L mutants, which varied in the placement of a quenching cysteine residue (*97*). In the first mutant, a cysteine replaced the lysine residue at the 23^{rd} position and, in the second mutant, replaced a threonine at the 57^{th} position. In both of these positions, the cysteine is too far away from the tryptophan residue to quench it when the protein is folded. When the protein is unfolded, the loop between the tryptophan and the cysteine is either 10 or 34 residues long.

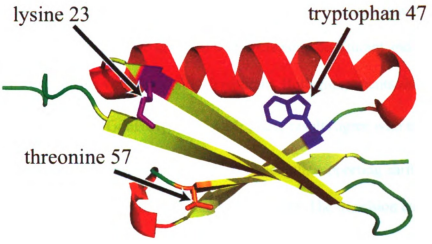

Figure 4.2.1 Cartoon depicting the structure of protein L. Note that the single tryptophan residue is hydrophobically buried when the protein is folded. Residues 23 or 57 were subsequently mutated to cysteine residues for contact quenching experiments. Image rendered using the PyMOL Molecular Graphics System (Delano Scientific, Palo Alto CA) using the structure 1HZ6 (*100*) in the Protein Data Bank[5] (*101*).

Section 1.3 explained how a Trp-Cys contact quenching protein folding experiment works. The tryptophan may decay by two different mechanisms, either by being quenched by a freely diffusive cysteine residue when the protein is in the unfolded state, which happens at a characteristically fast rate – or when the protein is folded by a much slower, natural decay mechanism, possibly due to solvent interactions. It is possible to determine the fraction of the molecules in the folded or unfolded state from the relative amplitude of the fast and slow rate for a measured triplet decay.

[5] www.pdb.org

UV fluorescence (Figure 4.2.2) excited at 280 nm has two significant SVD components, 1) an overall decrease in signal with increasing denaturant and 2) a spectral shift to higher wavelengths with increasing denaturant. Both components show a cooperative transition with $[GdnHCl]_{1/2} \sim 2.5$ M. These results agree with the previous report for titration curves measured at only one wavelength, supporting earlier conclusions that the protein only has two stable states (*21*). The transition curve from Trp-Cys contact quenching has a slightly higher midpoint, $[GdnHCl]_{1/2} \sim 2.8$ M, and is broader, suggesting complexity in the unfolded state that is not reflected in the fluorescence measurements.

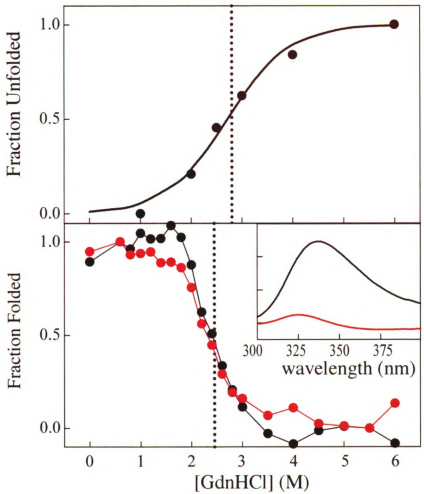

Figure 4.2.2 Fraction of the folded and unfolded populations of T57C as a function of denaturant concentration as measured by various spectroscopic probes. The plot in the top of the figure shows the fraction unfolded as measured by the relative amplitude of the fast Trp-Cys rate k_{fast} and shows a transition midpoint at ~ 2.8 M GdnHCl (dotted line). The plot on the bottom shows two independent spectral components of UV fluorescence data as determined from the SVD of a series of spectral measurements. Both the overall intensity (black) and the spectral shift (red) show a single cooperative transition at ~ 2.5 M GdnHCl (dotted line), indicating their sensitivity to only two conformational states. Data taken from Singh et al. (*97*).

Intramolecular Diffusion of the Unfolded State

The contact formation rate of the unfolded protein (k_{fast}) increases slightly with decreasing denaturant concentration when going from 6 M to about 3 M GdnHCl: however below 3 M, the rate drops sharply. This differs significantly from a similar

experiment performed by Buscaglia et al. in which measurements of Trp-Cys contact formation of unfolded cold shock protein found the rate to increase monotonically with decreasing denaturant concentration, which they interpreted as resulting from a increase in inter-residue interactions at lower concentrations of denaturant (*36*).

Previous studies have shown that the tryptophan triplet state lifetime is about 40 μs in water and greater than 1 ms when the tryptophan is buried in a protein's hydrophobic core (*28*). On the other hand, Lapidus et al. showed that for an unstructured peptide, a cysteine 10 residues away from the tryptophan will quench the triplet state on the 100 ns timescale (*29*). We observed rates in three different ranges at different denaturant concentrations; a fast rate due to intramolecular quenching ($\sim 10^5\ s^{-1}$) by cysteine, a slow rate due to natural decay of the triplet in a hydrophobic environment ($\sim 10^3\ s^{-1}$) and a medium rate due to solvent quenching ($\sim 10^4\ s^{-1}$). By plotting this data (Figure 4.2.3 right) along with the relative amplitude of each decay, it is evident that the stabilities of the protein ensembles leading to the fast and medium rates are very similar and are similar to the stability of the wild type as measured by fluorescence (Figure 4.2.2). This medium decay rate therefore represents a slowly diffusing population within the unfolded basin.

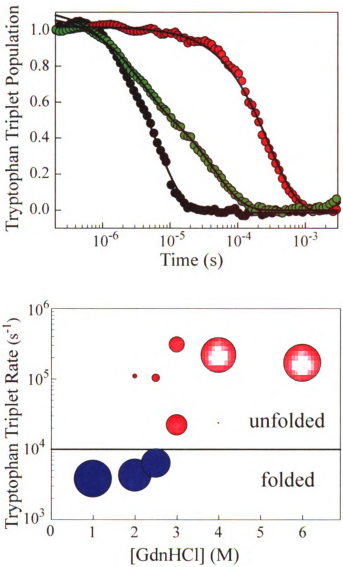

Figure 4.2.3 Top) Decay kinetics of the tryptophan triplet state of the mutant K23C at various concentrations of denaturant. The black (6 M GdnHCl) and red (1 M GdnHCl) points can be well fit to single exponentials, while the green (3 M GdnHCl) points require a two-exponential fit [fit values shown in bottom figure]. Bottom) Relative tryptophan triplet decay amplitudes for the protein mutant K23C are represented by the area of each circle as a function of denaturant concentration and observed rate. All kinetics were fit to two exponentials. The rates $\log(k) \geq 5\ s^{-1}$ are due to intramolecular diffusion between W47 and C23; $\log(k) \sim 4\ s^{-1}$ represents a relatively rigid conformation in which the tryptophan is quenched by solvent; $\log(k) \sim 3\ s^{-1}$ represents a native-like state with the tryptophan hydrophobically buried. Data taken from Waldauer et al. (*78*).

As discussed in section 1.3, it is possible to determine the reaction-limited (k_R) and diffusion-limited (k_{D+}) rates from the observed decay rate by varying the temperature and viscosity of the system as shown in the equation:

$$\frac{1}{k_{obs}} = \frac{1}{qK} + \frac{1}{k_{D+}} = \frac{1}{k_R(T)} + \frac{1}{k_{D+}(T,\eta)} \quad (4.1)$$

Figure 4.2.4 plots of $1/k_{obs}$ versus the viscosity η at a series of different temperatures. Note that the y-intercept of the line yields $1/k_R$ and the slope of the line gives $1/\eta k_{D+}$.

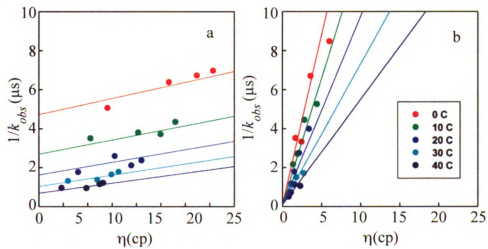

Figure 4.2.4 Temperature and viscosity dependence of observed quenching rates of protein L T57C at 6 M (a) and 2.3 M (b) GdnHCl. Errors of these measurements are typically less than 10%. Figures are taken from ref (*97*).

At 6 M GdnHCl, the diffusion-limited rate is 5 times faster than the reaction limited rate for both the short and the long loop mutants and is similar to that for unstructured peptides under similar conditions. As the denaturant condition decreases however, the reaction-limited and the diffusion-limited rates trend in opposite directions – the reaction-limited rate increases while the diffusion-limited rate decreases as shown in Figure 4.2.5.

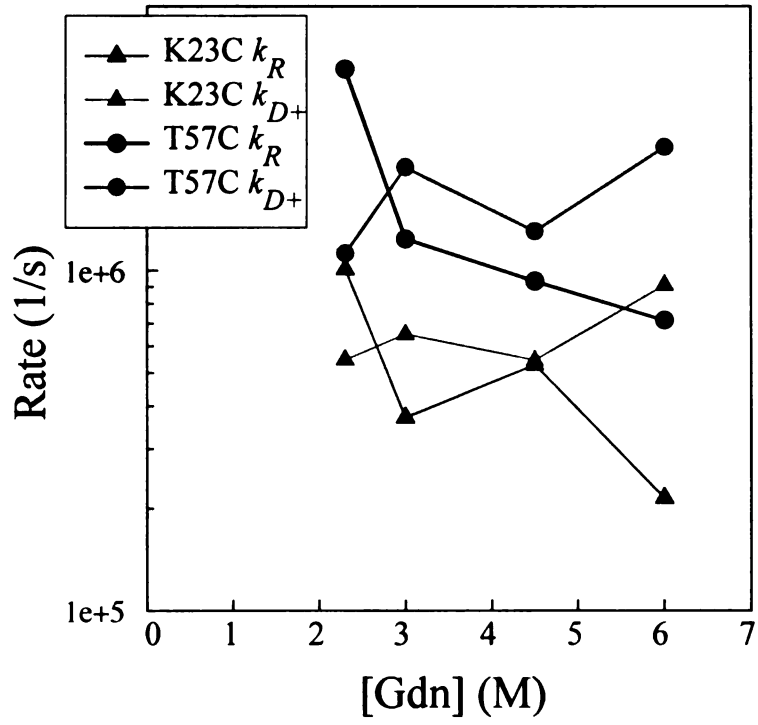

Figure 4.2.5 Reaction-limited and diffusion-limited rates as measured experimentally by Singh et al. (*97*) from the y-intercept and slope of line of best fit from the plot of $1/k_{obs}$ versus viscosity. Based on the sum of squares of the fit, the error of these rates is typically less than 10%. Note that k_R and k_{D+} trend in opposite directions. Data taken from Singh et al. (*97*).

Singh et al. (*97*) used a wormlike chain with an excluded volume, as described in section 1.3, to describe the Trp-Cys distance distribution in conjunction with SSS theory, to reproduce the measured k_R. They assumed that the persistence length l_p is an intrinsic property of the chain and should not change with solvent conditions, but that the excluded volume diameter d_α and the diffusion coefficient D are dependent on intramolecular interactions and therefore do depend on denaturant concentration. After simulating 2 million chains it was possible to determine a probability distribution, which can then be used in the equation presented in section 1.3,

$$k_R = \int_a^{\infty} q(r)P(r)dr \,, \tag{4.2}$$

and using the full description of $q(r)$ as determined experimentally by Lapidus et al. (*31*) (shown in section 1.3), to determine k_R. It was found that k_R had very little dependence on l_p and therefore the persistence length was fixed at 4 Å. The calculated rates were sensitive to the excluded volume d_a, which was allowed to vary. In this manner they were able to find the corresponding P(r) for any concentration of denaturant where k_R was experimentally measurable.

Table 4.2.1 Parameters used in wormlike chain simulations and the resulting k_R. calculated from equation 1.8. Taken from reference (*97*).

mutant	n	l_p (Å)	[GdnHCl] (M)	d_a (Å)	$\langle r^2 \rangle^{1/2}$ (Å)	calc. k_R (s^{-1})	meas. k_R (s^{-1})
T57C	10	4.0	6.0	3.9	19.2	7.4×10^5	7.2×10^5
			2.3	2.3	17.5	4.3×10^6	3.9×10^6
K23C	24	4.0	6.0	3.8	32.1	2.0×10^5	2.1×10^5
			2.3	2.3	28.6	1.1×10^6	1.0×10^6

Table 4.2.1, shows the measured k_R for both loops in 6 and 2.3 M denaturant concentrations and wormlike chain parameters that very closely matched the measured values. In 6 M GdnHCl, the values for the excluded volume diameter were very close to 4 Å, showing that the properties of the denatured proteins are very similar to those of completely unstructured peptide chains (*33*). Using the distributions that generated these calculated values of k_R, it was then possible to calculate the effective diffusion coefficient D, using the measured diffusion-limited rates in equation 1.9, which can be simplified as:

$$\frac{1}{k_{D+}} = \frac{1}{k_R^2 D}\int_a^{l_c}\frac{dr}{P(r)}\left\{\int_a^{l_c}(q(x)-k_R)\,P(x)dx\right\}^2 \qquad (4.3)$$

Table 4.2.2 Diffusion coefficients calculated from equation 4.1 using the wormlike chain probability distributions given in Table 4.2.1. Taken from reference (*97*).

mutant	[GdnHCl] (M)	meas k_{D+} (s^{-1}) (η = 1cP)	$D \times 10^6$ ($cm^2\ s^{-1}$)	$D_{6M}/D_{2.3M}$
T57C	6.0	2.3×10^6	0.33	6.6
	2.3	1.1×10^6	0.05	
K23C	6.0	9.1×10^5	0.57	5.2
	2.3	5.4×10^5	0.11	

The calculated diffusion coefficient, as shown in Table 4.2.2, varies greatly between the short and long loop mutants, which demonstrate that the intramolecular diffusion is a local property of the loop sequence. Singh et al. based this on two different observations: first, that the coefficients are lower than that of peptide sequences made of ~ 33% glycine (*33*), which should be less stiff than the denatured protein loop; and second, the T57C loop between the Trp and Cys, forms a β-strand and has a higher diffusion coefficient than the K23C loop which forms a mostly α-helical structure. This difference likely reflects the propensity for extended structure in the β-strand sequence.

Also note that the calculated coefficients for the protein mutants in 2.3 M denaturant both decrease by a factor of about 6 relative to 6 M GdnHCl. This most likely reflects a global property of the chain. The loss of denaturant yields a state that is still unfolded, but much less diffusive than that of a fully denatured protein, possibly reflecting transient interactions throughout the entire chain.

Discussion

This decrease in *D* represents a very significant change in the protein internal dynamics. As a point of reference, a change of this magnitude in the translational diffusion coefficient for a given particle through water would correspond to an almost 1000 fold increase in mass (*97*). Extrapolating this trend suggests that under folding conditions it may be low diffusivity that limits the folding rate.

4.3 UV Fluorescence and FRET Kinetics Measurements

The UV fluorescence emission of protein L was measured and normalized according to the procedures detailed in section 3.2 in a hydrodynamic focusing mixer fabricated from the most recent design, as detailed in section 2.1, with an optimal mixing time of $\sim 2 - 4$ μs.

Figure 4.3.1 Kinetics of protein L fluorescence after ultrarapid mixing, taken from Waldauer et al (*78*). a) Contour plot of tryptophan fluorescence with peak intensity near 350 nm in the mixer. Protein L in 6 M GdnHCl flows down from the top of the figure to the mixing region, which is positioned at ~ 45 μm in the y-axis of the image. b) Intensity as a function of time after mixing. The intensity is calculated as described in section 3.2. The black points are measured after mixing into 0 M GdnHCl and the green points after mixing into 6 M GdnHCl. c) Ratio of intensity after mixing into 0 M GdnHCl and into 6 M GdnHCl. The data shown were measured at three different flow rates and combined, with only the adjustment of a y-axis offset. The data for all three rates overlay seamlessly except near the mixing region, when the jet formation time will be different for different flow rates (these data not shown). The line is a fit of the data to two exponentials starting at 4.5 μs with the amplitudes constrained to be 1.0 at t = 0. d) FRET efficiency, E, as a function of time after mixing for constant 0 M GdnHCl (red), constant 6 M GdnHCl (green), and dilution to 0 M GdnHCl from 6 M GdnHCl (black). Intensities of donor and acceptor fluorophores are calculated as a sum over measurements over 0.3 μm across the jet and E is calculated using equation 3.1.

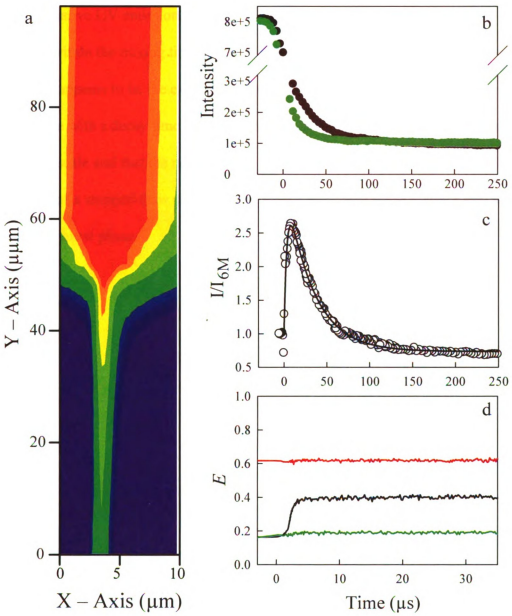

Figure 4.3.1

The relative UV emission (Figure 4.3.1.c) shows a significant increase in fluorescence within the mixing time, a small time-resolved increase with a rise time of 4 ± 2 μs (which appears to be the exponential tail of the unresolved phase), and a decrease in fluorescence with a decay time 43 ± 7 μs. Note that there is no significant change on the 1 ms time scale and that the net change in signal is negligible. Therefore, from the point of view of a stopped-flow measurement with a dead time greater than 1 ms, there is no perceptible burst phase.

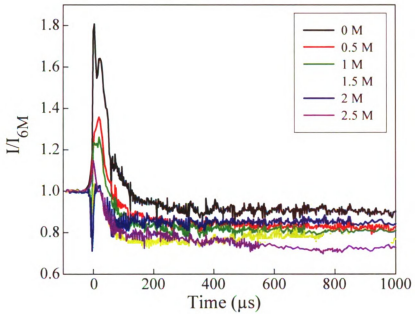

Figure 4.3.2 Folding kinetics of protein L after ultrarapid mixing into various concentrations of guanidine.

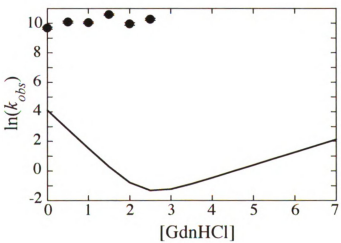

Figure 4.3.3 Measured rates of the slower decay in UV intensity (points), curve fitted from the decays shown in **Figure 4.3.2** and plotted as a function of final denaturant concentration. The line is the two-state model of the rates previously measured by Scalley et al. (*21*) using stopped-flow mixing.

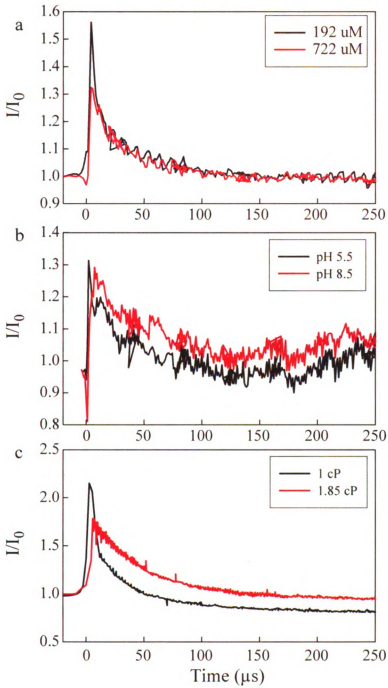

Figure 4.3.4 Folding kinetics of protein L after ultrarapid mixing under various conditions. For all measurements, the unfolded buffer conditions were 6 M GdnHCl at pH 7. a) Comparison of different protein concentrations: 192 (black) and 722 (red) μM. b) Comparison of different pH levels: pH 5.5 (black) and pH 8.5 (red). c) Comparison of different viscosities: 1.00 (black) and 1.85 (red) cP. The flow rates were adjusted to account for the increased viscosity due to adding sucrose.

Figure 4.3.2 shows the raw intensity decay at various denaturant concentrations and Figure 4.3.3 shows the rates of the slow decay. In contrast to the slower folding rates observed by stopped-flow mixing, these rates are independent of denaturant concentration. Figure 4.3.4 shows there is also no change in rate with changing protein concentration, changing the folding pH between 5 and 8, or a two-fold increase in the viscosity of the folding buffer. The early 4 μs rise in signal is too fast to accurately measure a rate with our instrument, but within our experimental error there does not seem to be any denaturant dependence on this process either.

Figure 4.3.1 (d) shows Förster resonance energy transfer (FRET) efficiency between two fluorophores at positions 16 and 64 on the folding protein chain as a function of time since mixing. These data were obtained by Shuhuai Yao at Lawrence Livermore National Laboratory from samples produced by Marcus Jäger at UCLA. FRET efficiency, E, is defined as the relative intensity of the acceptor fluorophores:

$$E = I_A / (I_D + I_A) \ , \qquad (4.4)$$

and is intrinsically normalized. The intensity of each fluorophore is observed on separate detectors and E is calculated point by point as shown in Figure 4.3.1 (d) (note that the data are not corrected for differences in detection between the two channels). In contrast to Figure 4.3.1 (d), plot (c) shows only a rapid increase in E within the mixing time of 2+2 μs. This result indicates that initial collapse due to the change in solvent conditions is much faster than 10^6 s^{-1}, in agreement with observations of other proteins (*77, 102, 103*).

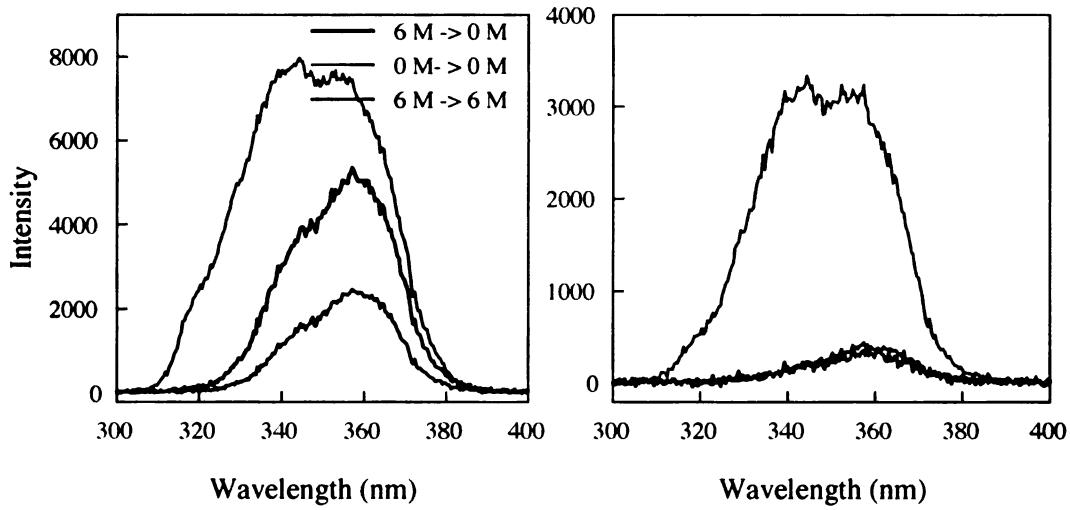

Figure 4.3.5 UV fluorescence spectra of protein L in 0 M GdnHCl (red) 6 M GdnHCl (green) and 0 M GdnHCl after dilution from 6 M GdnHCl (black). Each spectrum was collected 12 μm (left) and 64 μm (right) below the mixing region. The solution was moving at a speed of 0.54 m/s, which corresponds to 22 μs (left) and 118 μs (right) after mixing. The black and green spectra were recorded on the same sample. The red spectrum was recorded on a sample that had equilibrated in 0 M GdnHCl for more than 1 hour and had a concentration within 10% of the other sample.

The time-resolved fluorescence spectra were collected in 3 different experiments (6 M mixed into 6 M, 6 M to 0 M, and 0 M to 0 M GdnHCl) and analyzed individually (see Figure 4.3.5). There are two significant components: 1) An overall change in intensity that shows a rise during the mixing time, a ~ 50 μs decay, and another rise beyond 1 ms and; 2) A spectral shift that is only significant beyond 1 ms. This shows that full hydrophobic burial of the tryptophan only occurs in the final step of folding.

Discussion

In contrast to the folding studies outlined previously, the data here, presented by Waldauer et al. (*78*), suggest that the folding pathway ahead of the major barrier has a hidden complexity. We found a significant and unresolved increase in FRET and tryptophan fluorescence within 2 – 4 μs, and the tryptophan fluorescence has a resolved

tail that extends to ~ 8 μs (Figure 4.3.1). Since, in the absence of a significant barrier different probes may show different rates (*104*), the rise in tryptophan emission extending to ~ 8 μs and the unresolved increase in FRET efficiency may represent the same process of relaxation of the denatured protein population in 6 M GdnHCl into unfolded equilibrium in water. After the initial rise, the tryptophan emission decreases with a ~ 43 μs decay time. This rate is independent of flow rate, viscosity and protein concentration and extensive testing of these mixers (*60, 61*) show that once the jet has formed, the solvent composition has reached equilibrium. That the 43 μs decay observed by tryptophan emission is not mirrored in the FRET signal suggests that this phase is not a global collapse or expansion of the protein. Instead it likely reflects a local structural rearrangement that forms during the initial collapse and may not be productive to folding.

Does the 43 μs phase represent an intermediate state? According to Arrhenius, the rate is dependent on the size of then energy barrier between the two states. It is reasonable to assume that the size of the energy barrier changes as a function of denaturant concentration such that (*105*):

$$\Delta G_u([GdnHCl]) = \Delta G_u^0 - m[GdnHCl], \quad (4.5)$$

where ***m*** is an empirically determined constant and ΔG^0 is the energy barrier in 0 M denaturant. As such, the observed rate during folding or unfolding can be written as:

$$k_{obs} = k_f^{H_2O} e^{-m_f[GdnHCl]} + k_u^{H_2O} e^{m_u[GdnHCl]} \quad (4.6)$$

It is evident from this equation that if one plots the natural log of the observed rate as a function of denaturant concentration, that if there is an energy barrier, the log of the rate will have a linear dependence on denaturant. This is clearly visible in Figure 4.3.3 where

the measured rates for the 36 ms folding step show a chevron dependence on denaturant. From the slopes of the two sides of the two sides of the chevron, it is possible to determine m_f and m_u. It is also evident from the points in the figure showing the measured rate of the 43 μs decay that there is no visible dependence on denaturant concentration and the $m = 0$. The energy barrier ΔG^0 could still be nonzero, however there is no evidence of an intermediate such that $\Delta G^0 = -RT \ln([U]/[I])$. If such an intermediate exists it would certainly be off-pathway because the decay of tryptophan intensity is opposite from the increase in intensity observed during the last step of folding. However, there is no evidence that these rates have any dependence on denaturant concentration, and there is no observable structural distinction. Based on recent theoretical work on the relaxation rate of a two-state system with a range of barriers, we estimate an upper limit on the free-energy barrier of this process of 0.5 kcal/mol (*106*). Additionally, the lack of viscosity dependence on the rate of this process suggests that the unfolded state is dominated by internal friction or low intramolecular diffusion. Therefore we find little compelling evidence for a distinct intermediate rather than an ensemble of unfolded conformations.

Given the wide range of contact rates and the lack of conclusive evidence of an intermediate, we have chosen to describe the 43 μs process as diffusion on a rough potential using the formalism first developed by Zwanzig (*107*). The degree of roughness can be estimated by $\Delta E^2 = (kT)^2 \ln(\tau/\tau_0)$, in which τ is the observed process time and τ_0 is the expected time from diffusion on a smooth potential. Szabo, Schulten, Schulten theory for a Gaussian chain predicts the relaxation time of the unfolded state is $\tau_0 =$

$\langle R^2 \rangle / 3D$ (*33*). Using the diffusion coefficient determined by Singh et al. (*97*), $D = 10^{-8}$ cm^2/s and $R = 2.2$ nm yields a relaxation time of $\tau_0 \sim 1.6$ μs. Using $\tau = 43$ μs we calculate $\Delta E \approx 1$ kcal/mol, which is about 20% of the barrier height between the unfolded and native states.

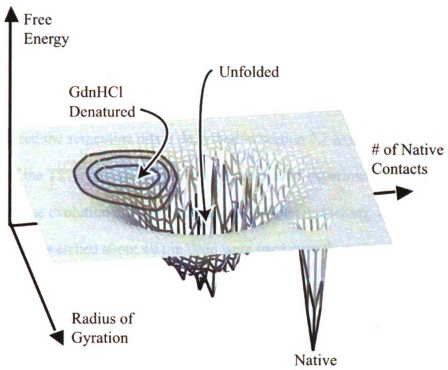

Figure 4.3.6 Conceptual representation of the energy landscape under final folding conditions as presented in Waldauer et al (*78*). The gray circles represent the population of the fully denatured molecules that relax on the landscape during and after mixing. The depth of the unfolded and folded basins are calculated from the two-state model given by Scalley et al. (*86*). The roughness in the unfolded basin is calculated by adding a normally distributed random number wit ha standard deviation of 1 kcal/mol. The < 10 μs rise in **Figure 4.3.1** c and d is the downhill relaxation of the denatured state into the unfolded basin. The 43 μs decay is the diffusion on the rough part of the landscape towards the bottom of the unfolded basin. The 36 ms rise time observed by Scalley et al. (*21*) is the escape from the unfolded to the native basin.

4.4 Trp-Cys Contact Quenching Kinetics Experiments

Equilibrium Trp-Cys contact quenching experiments showed that the unfolded state at 6 M GdnHCl differed greatly from that at 2.3 M GdnHCl. As the denaturant

concentration decreased, the rate for intramolecular diffusion also decreased while the reaction-limited rate increased. However, the equilibrium measurements were limited in that intramolecular diffusion could not be measured at concentrations below 2.3 M GdnHCl, because below this concentration the protein remains folded. Therefore, the only way to measure the intramolecular diffusion of a protein in folding conditions is to employ ultrarapid mixing such that the protein starts denatured but is quickly brought into folding conditions, such as 0 M concentration of denaturant, and observed as it begins to refold.

We used the serpentine mixer described in section 2.2 to measure Trp-Cys contact quenching of the T57C mutant of protein L. In a series of experiments we were able to measure the time evolution of the observed rate of triplet quenching. In the experiment, microfluidic chips etched about 40 μm deep were used with flow rates that allowed for a dead time of less than 300 μs. Measurements were taken on the instrument detailed in section 3.3. All measurements were taken with a 10× gain differential amplifier, yielding a total measured signal of about 30 – 40 mV as shown in the top of Figure 3.3.5. Each raw decay signal was logarithmically binned and then curve fitted to either a single or double decay, or at times a stretched exponential.

Measurements were taken at 200 μm intervals along the observation region as well as within the widening region between the end of the serpentine and the very beginning of the observation channel. At the highest flow rate observations within this region produced the earliest measurements, and were 281 μs after mixing. Total flow rates ranging from 235 (Re = 111) to 300 (Re = 142) μl/min were used. It was found that

with current fabrication techniques higher flow rates often lead unpredictably to permanent chip failure.

Three different mixing experiments exploring the time evolution of the triplet lifetime have been conducted so far, differing in the final denaturant concentrations of 0.17 M (mixing 4 M in 0 M GdnHCl, at a ratio of 10:225), 1.13 M (mixing 4 M into 1 M GdnHCl) and 4 M GdnHCl. All of the experiments were run with flow ratios of 1:23 or 1:25 sample-to-diluent per volume.

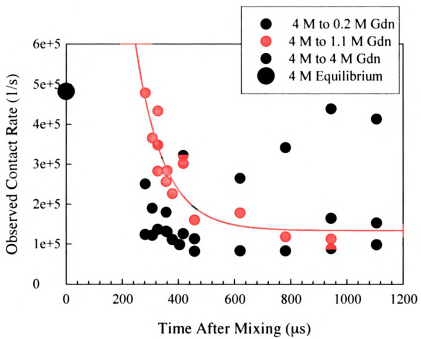

Figure 4.4.1 Plot showing the observed fast decay rate versus time after mixing into three different final denaturant concentrations. There is no evidence of time evolution of the observed fast rate when mixing from 4 to 0.2 M GdnHCl (black). When mixing from 4 to 1.1 M GdnHCl (red) it is possible to see the fast rate decrease exponentially with a decay time of about 100 μs with increasing time after mixing, which is evidence of the protein becoming more compact. There is a lot of scatter in the non-folding measurements, where the protein was mixed into 4 M GdnHCl (green), due to thermal lensing which made fitting the data to a double decay more difficult. Also included is the equilibrium fast rate measured by Singh et al in 4 M GdnHCl for comparison (*97*). Uncertainty in rate for all points was within 10% and uncertainty in time after mixing was ± 21 μs.

When mixing from 4 to 0.2 M GdnHCl, all of the absorbance measurements could be effectively fitted to a single exponential decay with about the same confidence as that of a double or stretched exponential decay. We found that, when the decay rates are plotted as a function of time after mixing there is little evidence of a time evolution of the observed rate when viewed from just less than 300 μs until over 1 ms of time after mixing. This is not surprising since the burst phase observed in the UV fluorescence mixer showed that any rearrangement in the unfolded state when going from 6 M to 0 M GdnHCl, such as collapse, occurs within the first 4 μs, with a relaxation time of about 40 – 50 μs which would make it very difficult to observe, since the first measurement was taken at 281 μs. In contrast to the UV fluorescence experiments, in which no change in the burst phase kinetics was observable with varying the final denaturant concentration, there is an exponential decay with a decay time of 100 μs in the fast rate of the observed rate when mixing from 4 M to a final concentration of 1.1 M GdnHCl. In the test case where the protein is being mixed such that the final concentration is the same as the initial, there should be no kinetics; however it was difficult to verify this experimentally because of an increase in thermal lensing, possibly due to the overall change in the index of refraction between the 0 M and 4 M GdnHCl, which made it difficult to separate the fast and slow decay rates.

To further investigate the fast rate and determine if the quenching is reaction or diffusion limited, a series of measurements were taken at the same time after mixing into 0 M GdnHCl with varying final sucrose concentrations. It is important to note that changing the viscosity of the diluent solutions affects the mixing properties of the chip. In this experiment, all the flow rates were kept the same at a total flow rate of 275 μl/min

with a flow speed of 3.78 m/s through the mixing region. The series of measurements had a range of Re in the mixing region from 140 at 0% sucrose to 62 for 23%, which is within the predicted range of efficient mixing for the serpentine chip (*74*).

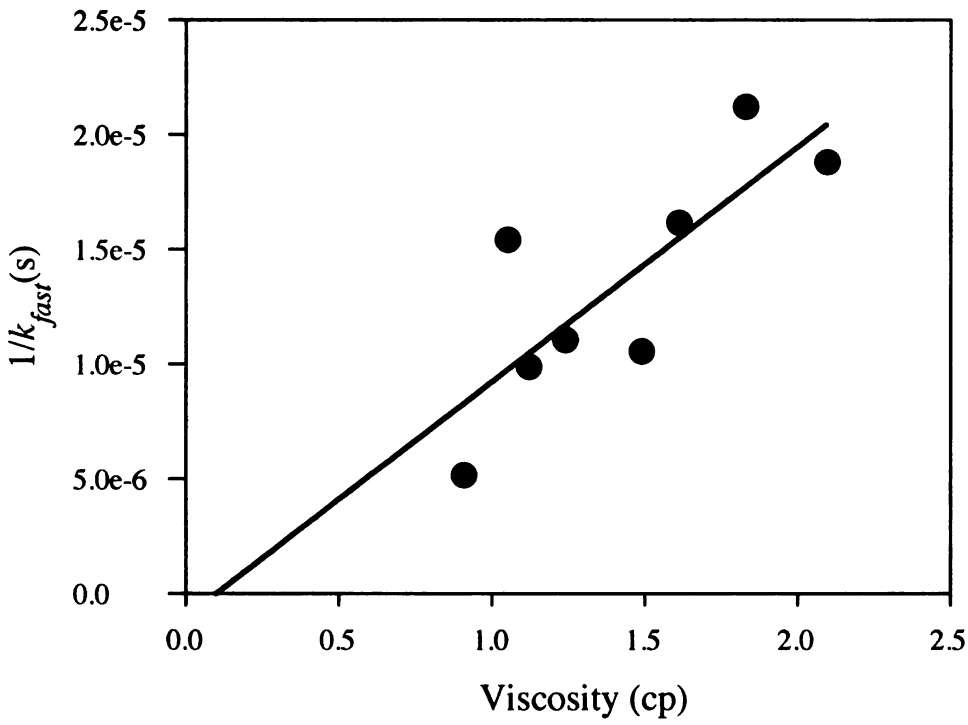

Figure 4.4.2 Plot showing $1/k_{fast}$ versus viscosity taken for protein L mixing from 4 M GdnHCl to a final concentration of about 0.16 M, 360 μs after mixing. The slope of the line of best fit is 1.0×10^{-5} s and corresponds to $1/k_{D+}$ at $\eta = 1.0$. The error in the y-intercept is 4.7×10^{-6} which is larger than the calculated value of -1.0×10^{-6}, which places an upper limit on $1/k_R$ of 3.7×10^{-6} s. Such a low value of k_R means that the measured contact quenching was most likely diffusion limited. Uncertainty in rate for all points was within 10%.

From equation 1.6 it has been shown that, by plotting $1/k_{obs}$ as a function of viscosity, one can determine the reaction limited rate k_R from the y-intercept of the line of best fit. When the observed rates taken when mixing into 0.16 M GdnHCl are plotted,

as shown in Figure 4.4.2, the line of best fit has a negative y-intercept of -1.0×10^{-6} s with an error of 4.7×10^{-6} s. This puts a lower limit on the possible value for k_R of 2.7×10^5 s^{-1} ($1/k_R < 3.7 \times 10^{-6}$ s). It is possible to determine $1/k_{D+} = 1.0 \times 10^{-5}$ at $\eta = 1$ from the same plot used for k_R from the slope of the line of best fit. Further experiments are needed to determine if quenching in other denaturant concentrations such as 1 M GdnHCl is diffusion-limited.

In order to determine the intramolecular diffusion coefficient D from SSS theory it is necessary to determine the pairwise distance probability distribution of the tryptophan and cysteine residues. For unstructured peptides and the equilibrium Trp-Cys experiments discussed in section 4.2, the distributions were determined from a wormlike chain model with excluded volume. This model is sufficient to characterize the intramolecular diffusion of unstructured peptide chains or unfolded proteins in relatively high concentrations of denaturant, but in order to model an unfolded protein in folding conditions like those in 0 M GdnHCl, the parameters used become unphysical and the model breaks down.

Instead of a simple physical model, a probability distribution can be determined from a large series of molecular dynamics (MD) simulations. MD simulations have a number of advantages over Monte Carlo chain sampling algorithms such as wormlike chain or random coil, and other non-physics based models such as GO-like models. These advantages include: 1) MD simulations are unbiased by native structure (in contrast to GO-like models that are based on the native state topology); 2) The simulations take into account quantitative chemical detail such as the hydrophobicity and

charge of each residue; 3) they can model the unfolded state in the absence of denaturant; and 4) MD simulations can predict early folding events under folding conditions.

Voelz *et al.* have run thousands of all-atom implicit solvent MD simulations of protein L, yielding enough statistics to construct a series of distance probability distributions (*35*). Simulations were run on the distributed computing platform Folding@Home on hundreds of graphics processing units (GPU). All the simulations were run using the AMBER9 MD package, using a specially modified GROMACS for GPU and the AMBER9 ff96 force field with a generalized Born/surface area (GBSA) implicit solvent model.

To obtain sufficient statistics, Voelz et al. ran ~ 10,000 parallel simulations at 300 K, 330 K, 370 K and 450 K, from which they were then able to calibrate through polymer theory modeling to being the equivalent to 0.25 M, 1.5 M, 2.3 M and ~ 3.2 M GdnHCl concentrations respectively. The simulations were started with the protein in either an extended or random coil conformation; both populations converged within 1 μs to a collapsed compact globule state with a radius of gyration R_g ~ 12.2 Å for temperatures up to 370 K and R_g ~ 21.8 Å at 450 K, which is much closer to that of a random coil conformation. In comparison, the average R_g for the simulations started in the native state was about 12 Å, only 0.2 Å smaller than that of the unfolded proteins after 1 μs when simulated in folding conditions. This compares well with the R_g = 11.8 Å of the NMR structure (*108*), but lower than the value of $R_g \approx 11.8$ Å that measured in SAXS (*94*) and single-molecule FRET (*109*) experiments. As noted by Merchant et al., His-tag and

FRET labeling effects, and/or overestimation of Rg in the SAXS experiment can explain this difference (*110*).

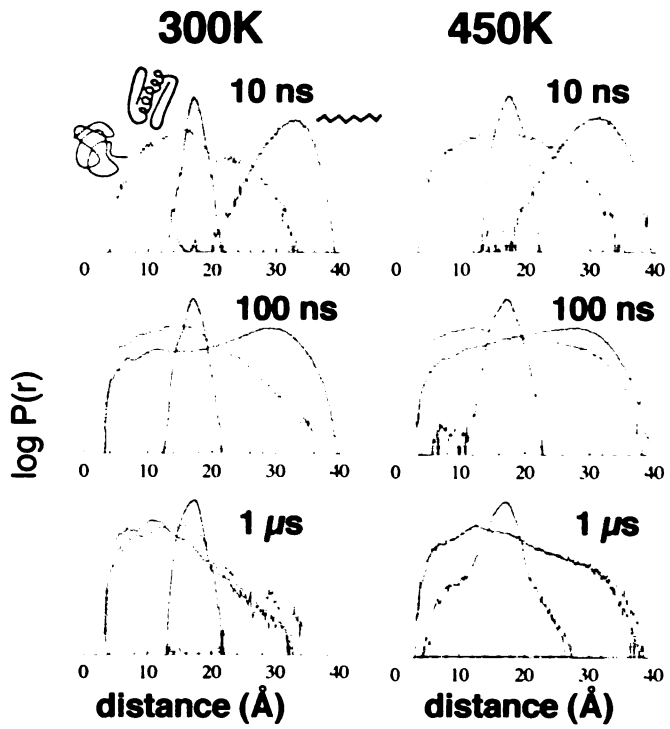

Figure 4.4.3 Histograms of the Trp-Cys distance probability distribution P(r) as determined by tens of thousands of MD simulations (*35*). The simulations run at 300 K are calibrated to correspond to proteins in 0 M GdnHCl and 450 K to about 3.2 M GdnHCl. At both temperatures, populations started in extended coil (red) and random coil (tan) conformations both converged to the same probability distribution. Populations started in the native conformation (blue) however remained stable.

From the Trp-Cys distance distribution P(r), it is possible to calculate the reaction-limited rate k_R, using equation 1.6. Using the distribution from simulations run at 300 K, which is equivalent to 0.25 M GdnHCl, $k_R = 2.6 \times 10^7\ s^{-1}$, well above the lower limit determined experimentally.

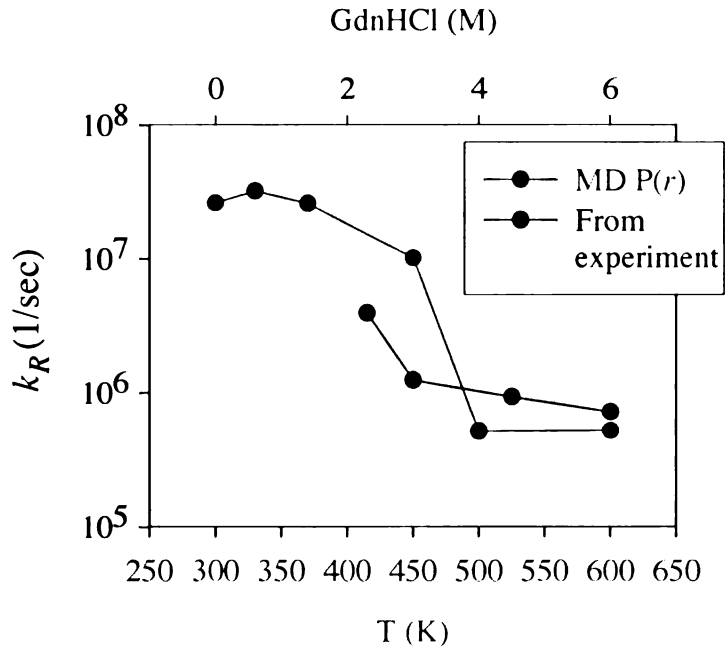

Figure 4.4.4 Reaction-limited rates calculated by using either a wormlike chain model or MD simulations (*35*). The very high rates as the denaturant concentration decreases imply that the observed rate become diffusion-limited.

By using equation 1.7, the calculated P(r) and k_R, and the value of k_{D+} determined experimentally, it is further possible to determine the intramolecular diffusion constant $D = 6.07 \times 10^{-10}$ cm^2/s. This is about 80 times smaller than that determined for protein L in 2.3 M GdnHCl and about 550 times smaller than D for 6 M GdnHCl.

It would seem that with such a low diffusion coefficient, the protein would move too slowly for Trp-Cys quenching to occur, however the length scales are much more compact for the protein in folding conditions in comparison with the protein in 6 M GdnHCl as shown by the change in R_g discussed previously. The average Trp-Cys distance from the MD simulations at 300 K (0.25 M GdnHCl) is 11.3 Å, which corresponds to a diffusion time of 21 μs ($t_D = r^2/D$) or a rate of 47,600 s^{-1}.

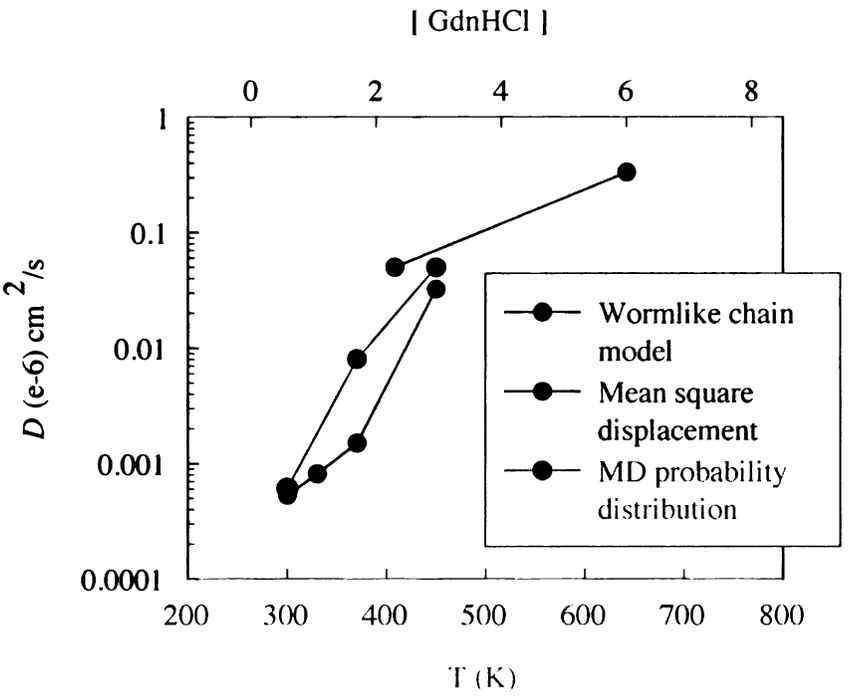

Figure 4.4.5 Intramolecular diffusion coefficient of the T57C mutant as determined via experiment and computer simulation. Values determined using measured k_{D+} are shown in purple and red. Values determined through mean sequence displacement (green) used information solely from MD simulation. The diffusion coefficient determined using the Trp-Cys mixing instrument and the MD P(*r*) is shown as the black outlined red circle and is in remarkably good agreement with the value predicted by MD alone (green).

Discussion

The experiments detailed above offer one of the first opportunities to measure the intramolecular diffusion of an unfolded protein under folding conditions. By varying the viscosity of the protein solution we found that the Trp-Cys contact quenching rate is very close to the diffusion-limited rate and that *D* decreases by a factor of ~ 550 from when the protein is in 6 M GdnHCl to folding conditions. This is a massive drop in intramolecular diffusion and, in comparison to the translational diffusion for the entire protein molecule, about 10×10^{-7} cm^2/s, is over 1500 times larger.

Any change in the observed fast rate k_{fast}, which is very close to being that of k_{D+}, since the rate is diffusion-limited, happens before our first available measurement at about 300 μs when mixing from 4 to 0 M GdnHCl. When mixing into 1 M GdnHCl, k_{fast} decreases exponentially however, which is in contrast to the ~ 50 μs decay time relaxation observed with the UV fluorescence mixer, which did not show any change with final denaturant concentration.

5. Conclusions

We have introduced the complexity behind protein folding and the necessity to understand the earliest events and the dynamics of the unfolded state in order to better understand the process as a whole. The avenue chosen to explore these processes in this thesis was through ultrarapid microfluidic mixers, using fluorescence and Trp-Cys contact quenching.

The microfluidic mixers introduced in this thesis use two different methods to overcome the limitations imposed by low Reynolds flow. The first is a hydrodynamic focusing mixer, which uses the equations behind laminar flow to focus a ribbon of protein solution only a hundred nanometers wide and produces mixing times of less than 5 μs with femtomolar sample consumption. The second, a serpentine mixer, is able to mix the much higher volumes that are necessary for optical absorbance measurements. It works by exploiting the fact that a fluid, even at low Reynolds number, can manifest chaotic advection. Using this toolbox we investigated the folding of the B1 domain of protein L – a protein that has long been established to be a simple two state folder – and found new kinetics.

UV fluorescence measurements taken with the hydrodynamic focusing mixer revealed hidden kinetics. In my experiments I saw a small time-resolved increase in fluorescence with a rise time of about 4 ± 2 μs and a decrease in fluorescence with a decay time of 43 ± 7 μs, which would have been entirely within the dead time of a stopped-flow instrument. I found that neither the rise time nor the decay time has any

visible dependence on the final denaturant concentration or other variables such as pH, viscosity or protein concentration. When similar FRET experiments were run by Shuhai Yao on an identical mixer there was a rapid increase in the FRET efficiency *E*, within the mixing time of 2 ± 2 μs but the decay was not mirrored in *E* implying that the decay was not a global phenomenon like collapse or expansion but more likely a structural rearrangement. This explanation is strengthened by the observation that there is no spectral shift within the observable time window for the hydrodynamic-focusing mixer, implying that any hydrophobic burial must occur much later during the final folding steps. The lack of any viscosity dependence for the decay implies that the unfolded state is dominated by internal friction or low intramolecular diffusion. From these results I postulate that the unfolded state is complex.

In this thesis are results of the first measurements of Trp-Cys contact quenching taken in a microfluidic mixer. I found that there was no time evolution in the fast observed rate over a time window starting at 281 μs following mixing and extending to about 1100 μs, when starting with a denaturant concentration of 4 M GdnHCl and mixing into a final concentration of 0.2 M. However, in contrast to my earlier fluorescence mixer experiments, when mixing into a final denaturant concentration of 1.2 M GdnHCl the fast rate slowed exponentially with time, with a decay rate of about 100 μs.

To put my observations in context, consider equilibrium measurements by Singh et al. which showed that as denaturant concentration decreases the reaction-limited rate increases and the diffusion-limited rate decreases, but these measurements were limited to GdnHCl concentrations no lower than 2.3 M. With the mixer, I was able to measure the intramolecular diffusion of an unfolded protein in folding conditions, which would

most closely mimic the conditions of a newly formed protein being released from the ribosome. Experimentally I was able to place a lower limit on the reaction-limited rate of 2.7×10^5 s^{-1} unfolded protein L in 0 M GdnHCl, and found that quenching is diffusion limited with a rate of 1.0×10^5 s^{-1}. Using the MD simulations by Voelz et al. to produce a calculated P(r) at 300 K in folding conditions, I found that at 0.25 M GdnHCl the reaction limited-rate is 2.6×10^7 s^{-1} and $D = 6.07 \times 10^{-10}$ cm^2/s, which is surprisingly close to the value calculated directly from the MD simulations without any experimental measurements. This value for D is about 550 times smaller than that determined for protein L in 6 M GdnHCl.

The difference in kinetics as measured by fluorescence and Trp-Cys contact quenching suggests the unfolded state undergoes a complex evolution before reaching the dominant energy barrier separating the folded and unfolded state. The roughness shown in Figure 4.3.6 can also be estimated by the ratio of the diffusion coefficients determined at 4 and 0.25 M GdnHCl such that $\Delta E^2 = (kT)^2 \ln(D_{4\ M} / D_{0.25\ M})$. In this case the roughness $\Delta E \sim 1.5$ kcal/mol, but further experiments are necessary to fully quantify this feature. Furthermore, the drastic change in D shows that diffusion in the unfolded state is extremely slow and must therefore significantly impact the final folding rate.

6. References

1. Kendrew, J. C., Dickerson, R. E., Strandberg, B. E., Hart, R. G., Davies, D. R., Phillips, D. C., and Shore, V. C. (1960) Structure of myoglobin: A three-dimensional Fourier synthesis at 2 A. resolution, *Nature 185*, 422-427.

2. Mirsky, A., and Anson, M. (1929) Protein coagulation and its reversal - The reversal of the coagulation of hemoglobin, *J Gen Physiol 13*, 133-143.

3. Anfinsen, C., Haber, E., Sela, M., and White, F. H. (1961) The kinetics of formation of native ribonuclease during oxidation of the reduced polypeptide chain, *Proc Natl Acad Sci USA 47*, 1309-1314.

4. Anfinsen, C. B. (1973) Principles that govern the folding of protein chains, *Science 181*, 223-230.

5. Dill, K. A., Ozkan, Weikl, Chodera, J., and Voelz. (2007) The protein folding problem: when will it be solved?, *Curr Opin Struct Biol.*

6. Bryngelson, J. D., and Wolynes, P. G. (1987) Spin glasses and the statistical mechanics of protein folding, *Proc Natl Acad Sci USA 84*, 7524-7528.

7. Nölting, B., Golbik, R., Neira, J. L., Soler-Gonzalez, A. S., Schreiber, G., and Fersht, A. R. (1997) The folding pathway of a protein at high resolution from microseconds to seconds, *Proc Natl Acad Sci USA 94*, 826-830.

8. Bai, Y., Sosnick, T., Mayne, L., and Englander, S. (1995) Protein folding intermediates: native-state hydrogen exchange, *Science*, 192-192.

9. Onuchic, J. N., Luthey-Schulten, Z., and Wolynes, P. G. (1997) Theory of protein folding: the energy landscape perspective, *Annual review of physical chemistry 48*, 545-600.

10. Dill, K. A. (1999) Polymer principles and protein folding, *Protein Sci 8*, 1166-1180.

11. Bicout, D. J., and Szabo, A. (2000) Entropic barriers, transition states, funnels, and exponential protein folding kinetics: a simple model, *Protein Sci 9*, 452-465.

12. Dinner, A. R., Sali, A., Smith, L. J., Dobson, C. M., and Karplus, M. (2000) Understanding protein folding via free-energy surfaces from theory and experiment, *Trends Biochem Sci 25*, 331-339.

13. Onuchic, J. N., and Wolynes, P. G. (2004) Theory of protein folding, *Curr Opin Struct Biol 14*, 70-75.

14. Oliveberg, M., and Wolynes, P. G. (2005) The experimental survey of protein-folding energy landscapes, *Q Rev Biophys 38*, 245-288.

15. Duan, Y., and Kollman, P. A. (1998) Pathways to a Protein Folding Intermediate Observed in a 1-Microsecond Simulation in Aqueous Solution, *Science 282*, 740-744.

16. Liwo, A., Khalili, M., and Scheraga, H. A. (2005) Ab initio simulations of protein-folding pathways by molecular dynamics with the united-residue model of polypeptide chains, *Proceedings of the National Academy of Sciences of the United States of America 102*, 2362-2367.

17. Nölting, B., and Andert, K. (2000) Mechanism of protein folding, *Proteins 41*, 288-298.

18. Kubelka, J., Chiu, T. K., Davies, D. R., Eaton, W. A., and Hofrichter, J. (2006) Sub-microsecond protein folding, *J Mol Biol 359*, 546-553.

19. Dumont, C., Emilsson, T., and Gruebele, M. (2009) Reaching the protein folding speed limit with large, sub-microsecond pressure jumps, *Nature Methods 6*, 515-519.

20. Kubelka, J., Hofrichter, J., and Eaton, W. A. (2004) The protein folding 'speed limit', *Curr Opin Struct Biol 14*, 76-88.

21. Scalley, M. L., Yi, Q., Gu, H., McCormack, A., Yates, J. R., and Baker, D. (1997) Kinetics of folding of the IgG binding domain of peptostreptococcal protein L, *Biochemistry 36*, 3373-3382.

22. Dobson, C. M. (2004) Principles of protein folding, misfolding and aggregation, *Semin Cell Dev Biol 15*, 3-16.

23. Fung, B., and McGaughy, T. (1976) Molecular motions in liquid. I. Rotation of water and small alcohols studied by deuteron relaxation, *The Journal of chemical physics 65*, 2970-2976.

24. Hamm, P., Helbing, J., and Bredenbeck, J. (2008) Two-dimensional infrared spectroscopy of photoswitchable peptides, *Annual review of physical chemistry 59*, 291-317.

25. Demchenko, A. P. (1986) *Ultraviolet spectroscopy of proteins*, Rev. and enl. translation of the Russian ed., Springer-Verlag, Berlin ; New York.

26. King, J. L., and Jukes, T. H. (1969) Non-Darwinian evolution, *Science 164*, 788-798.

27. Lakowicz, J. R. (2006) *Principles of fluorescence spectroscopy*, 3rd ed., Springer, New York.

28. Vanderkooi, J. M., (Ed.) (1992) *Topics in fluorescence spectroscopy: Biochemical Applications*, Vol. 3, Plenum Press, New York.

29. Lapidus, L. J., Eaton, W. A., and Hofrichter, J. (2000) Measuring the rate of intramolecular contact formation in polypeptides, *Proc Natl Acad Sci USA 97*, 7220-7225.

30. Connors, K. A. (1990) *Chemical kinetics : the study of reaction rates in solution*, VCH, New York, N.Y.

31. Lapidus, L. J., Eaton, W. A., and Hofrichter, J. (2001) Dynamics of intramolecular contact formation in polypeptides: distance dependence of quenching rates in a room-temperature glass, *Phys Rev Lett 87*, 258101.

32. Lapidus, L. J., Steinbach, P., Eaton, W. A., and Szabo, A. (2002) Effects of Chain Stiffness on the Dynamics of Loop Formation in Polypeptides. , *J. Phys. Chem. B.*

33. Buscaglia, M., Lapidus, L. J., Eaton, W. A., and Hofrichter, J. (2006) Effects of denaturants on the dynamics of loop formation in polypeptides, *Biophys J 91*, 276-288.

34. Szabo, A., Schulten, K., and Luthey-Schulten, Z. (1980) First passage time approach to diffusion controlled reactions, *The Journal of chemical physics.*

35. Voelz, V. A., Singh, V. R., Wedemeyer, W. J., Lapidus, L. J., and Pande, V. S. (2009) Unfolded state dynamics and structure of protein L characterized by simulation and experiment, *J Am Chem Soc.*

36. Buscaglia, M., Schuler, B., Lapidus, L. J., Eaton, W. A., and Hofrichter, J. (2003) Kinetics of intramolecular contact formation in a denatured protein, *J Mol Biol 332*, 9-12.

37. Rami, B. R., and Udgaonkar, J. B. (2001) pH-Jump-Induced Folding and Unfolding Studies of Barstar: Evidence for Multiple Folding ..., *Biochemistry.*

38. Liu, F., Dumont, C., Zhu, Y., DeGrado, W. F., Gai, F., and Gruebele, M. (2009) A one-dimensional free energy surface does not account for two-probe folding kinetics of protein alpha(3)D, *The Journal of chemical physics 130*, 061101.

39. Chan, C. K., Hofrichter, J., and Eaton, W. A. (1996) Optical triggers of protein folding, *Science 274*, 628-629.

40. Bredenbeck, J., Helbing, J., Kumita, J. R., Woolley, G. A., and Hamm, P. (2005) Alpha-helix formation in a photoswitchable peptide tracked from picoseconds to

microseconds by time-resolved IR spectroscopy, *Proc Natl Acad Sci USA 102*, 2379-2384.

41. Cecconi, C., Shank, E. A., Bustamante, C., and Marqusee, S. (2005) Direct observation of the three-state folding of a single protein molecule, *Science 309*, 2057-2060.

42. Rief, M., Gautel, M., Oesterhelt, F., Fernandez, J. M., and Gaub, H. E. (1997) Reversible Unfolding of Individual Titin Immunoglobulin Domains by AFM, *Science 276*, 1109.

43. Freddolino, P. L., Liu, F., Gruebele, M., and Schulten, K. (2008) Ten-microsecond molecular dynamics simulation of a fast-folding WW domain, *Biophys J 94*, L75-77.

44. Kolinski, A., and Skolnick, J. (2004) Reduced models of proteins and their applications, *Polymer 45*, 511-524.

45. Ihalainen, J. A., Bredenbeck, J., Pfister, R., Helbing, J., Chi, L., van Stokkum, I. H. M., Woolley, G. A., and Hamm, P. (2007) Folding and unfolding of a photoswitchable peptide from picoseconds to microseconds, *Proc Natl Acad Sci USA 104*, 5383-5388.

46. Regenfuss, P., and Clegg, R. (1987) Diffusion-controlled association of a dye, 1-anilinonaphthalene-8-sulfonic acid, to a protein, bovine serum albumin, using a fast-flow microsecond mixer and stopped-flow., *Biophysical chemistry 26*, 83.

47. Regenfuss, P., Clegg, R. M., and Fulwyler, M. J. (1985) Mixing liquids in microseconds, *Rev Sci Instrum 56*, 283-290.

48. Shastry, M. C., Luck, S. D., and Roder, H. (1998) A continuous-flow capillary mixing method to monitor reactions on the microsecond time scale, *Biophys J 74*, 2714-2721.

49. Park, S. H., Shastry, M. C., and Roder, H. (1999) Folding dynamics of the B1 domain of protein G explored by ultrarapid mixing., *Nat. Struct. Biol. 6*, 943-947.

50. Capaldi, A. P., Shastry, M. C., Kleanthous, C., Roder, H., and Radford, S. E. (2001) Ultrarapid mixing experiments reveal that Im7 folds via an on-pathway intermediate, *Nat. Struct. Biol. 8*, 68-72.

51. Welker, E., Maki, K., Shastry, M. C., Juminaga, D., Bhat, R., Scheraga, H. A., and Roder, H. (2004) Ultrarapid mixing experiments shed new light on the characteristics of the initial conformational ensemble during the folding of ribonuclease A, *Proc Natl Acad Sci USA 101*, 17681-17686.

52. Maki, K., Cheng, H., Dolgikh, D. A., Shastry, M. C., and Roder, H. (2004) Early events during folding of wild-type staphylococcal nuclease and a single-tryptophan variant studied by ultrarapid mixing, *J Mol Biol 338*, 383-400.

53. Roder, H., Maki, K., Cheng, H., and Shastry, M. C. (2004) Rapid mixing methods for exploring the kinetics of protein folding, *Methods 34*, 15-27.

54. Chan, C. K., Hu, Y., Takahashi, Rousseau, D. L., Eaton, W. A., and Hofrichter, J. (1997) Submillisecond protein folding kinetics studied by ultrarapid mixing, *Proc Natl Acad Sci USA 94*, 1779-1784.

55. Bilsel, O., Kayatekin, C., Wallace, L. A., and Matthews, C. R. (2005) A microchannel solution mixer for studying microsecond protein folding reactions, In *Rev Sci Instrum*, p 014302.

56. Doyle, S. M., Bilsel, O., and Teschke, C. M. (2004) SecA folding kinetics: a large dimeric protein rapidly forms multiple native states, *J Mol Biol 341*, 199-214.

57. Purcell, E. (1977) Life at low Reynolds number, *American Journal of Physics 45*, 3-11.

58. Brody, J. P., Yager, P., Goldstein, R. E., and Austin, R. H. (1996) Biotechnology at low Reynolds numbers, *Biophys J 71*, 3430-3441.

59. Bakajin, O., Brody, J. P., Chou, C., Chan, S., Duke, T. A. J., Knight, J. B., Sohn, L., Vishwanath, A., Austin, R. H., and Cox, E. C. (1999) Polymer dynamics and fluid flow in microfabricated devices, *Proc. Soc. Photo-Opt. Instru. Eng 3258*, 100-113.

60. Hertzog, D. E., Michalet, X., Jäger, M., Kong, X., Santiago, J. G., Weiss, S., and Bakajin, O. (2004) Femtomole mixer for microsecond kinetic studies of protein folding, *Anal Chem 76*, 7169-7178.

61. Hertzog, D. E., Ivorra, B., Mohammadi, B., Bakajin, O., and Santiago, J. G. (2006) Optimization of a microfluidic mixer for studying protein folding kinetics, *Anal Chem 78*, 4299-4306.

62. Ivorra, B., Hertzog, D. E., Mohammadi, B., and Santiago, J. G. (2006) Semi-deterministic and genetic algorithms for global optimization of microfluidic protein-folding devices, *Int. J. Numer. Meth. Eng. 66*, 319-333.

63. Berger, S. A., Talbot, L., and Yao, L. S. (1983) Flow in Curved Pipes, *Annual Review of Fluid Mechanics 15*, 461-512.

64. Yao, S., and Bakajin, O. (2007) Improvements in mixing time and mixing uniformity in devices designed for studies of protein folding kinetics, *Anal Chem 79*, 5753-5759.

65. Aref, H. (1984) Stirring by chaotic advection, *Journal of Fluid Mechanics 143*, 21.

66. Aref, H. (2002) The development of chaotic advection, *Physics of Fluids 14*, 1315-1325.

67. Stroock, A. D., Dertinger, S. K., Ajdari, A., Mezic, I., Stone, H. A., and Whitesides, G. M. (2002) Chaotic mixer for microchannels, *Science 295*, 647-651.

68. Yi, M., and Bau, H. H. (2003) The kinematics of bend-induced mixing in micro-conduits, *International Journal of Heat and Fluid Flow 24*, 645-656.

69. Jen, C. P., Wu, C. Y., Lin, Y. C., and Wu, C. Y. (2003) Design and simulation of the micromixer with chaotic advection in twisted microchannels, *Lab on a chip 3*, 77-81.

70. Kim, D. S., Lee, S. H., Kwon, T. H., and Ahn, C. H. (2005) A serpentine laminating micromixer combining splitting/recombination and advection, *Lab on a chip 5*, 739-747.

71. Xia, H. M., Shu, C., Wan, S. Y. M., and Chew, Y. T. (2006) Influence of the Reynolds number on chaotic mixing in a spatially periodic micromixer and its characterization using dynamical system techniques, *Journal of Micromechanics and Microengineering 16*, 53-61.

72. Chamarthy, P., and Wereley, S. (2004) Mixing Characteristics in a Serpentine Micro-Channel, *Proceedings of the IMECE'04*.

73. Hoffmann, A., Kane, A. S., Nettels, D., Hertzog, D. E., Baumgärtel, P., Lengefeld, J., Reichardt, G., Horsley, D. A., Seckler, R., Bakajin, O., and Schuler, B. (2007) Mapping protein collapse with single-molecule fluorescence and kinetic synchrotron radiation circular dichroism spectroscopy, *Proc Natl Acad Sci USA 104*, 105-110.

74. Kane, A. S., Hoffmann, A., Baumgärtel, P., Seckler, R., Reichardt, G., Horsley, D. A., Schuler, B., and Bakajin, O. (2008) Microfluidic Mixers for the Investigation of Rapid Protein Folding Kinetics Using Synchrotron Radiation Circular Dichroism Spectroscopy, *Anal Chem 80*, 9534-9541.

75. Ghosh, A., and Ryszytiwskyj, W. (1994) Removal of Glass Particles from Glass Surfaces: A Review, *Particles on surfaces [4]: detection*, 353-362.

76. Spierings, G. A. C. M., Haisma, J., and Michelsen, T. M. (1995) Surface-related phenomena in the direct bonding of silicon and fused-silica wafer pairs, *Philips Journal of Research 49*, 47-63.

77. Lapidus, L. J., Yao, S., McGarrity, K. S., Hertzog, D. E., Tubmann, E., and Bakajin, O. (2007) Protein hydrophobic collapse and early folding steps observed in a microfluidic mixer, *Biophys J 93*, 218-224.

78. Waldauer, S. A., Bakajin, O., Ball, T., Chen, Y., Decamp, S. J., Kopka, M., Jäger, M., Singh, V. R., Wedemeyer, W. J., Weiss, S., Yao, S., and Lapidus, L. J. (2008) Ruggedness in the folding landscape of protein L, *HFSP J 2*, 388-395.

79. Decamp, S. J., Naganathan, A. N., Waldauer, S. A., Bakajin, O., and Lapidus, L. J. (2009) Direct observation of downhill folding of lambda-repressor in a microfluidic mixer, *Biophys J 97*, 1772-1777.

80. Henry, E. R., and Hofrichter, J. (1992) Singular Value Decomposition: Application to Analysis of Experimental Data, *Meth Enzymol 210*, 129-192.

81. Golub, G., and Kahan, W. (1965) Calculating the singular values and pseudo-inverse of a matrix, *Journal of the Society for Industrial and Applied Mathematics: Series B, Numerical Analysis 2*, 205-224.

82. Li, P., Oliva, F. Y., Naganathan, A. N., and Muñoz, V. (2009) Dynamics of one-state downhill protein folding, *Proceedings of the National Academy of Sciences of the United States of America 106*, 103-108.

83. Singh, V. R., and Lapidus, L. J. (2008) The intrinsic stiffness of polyglutamine peptides, *J. Phys. Chem. B 112*, 13172-13176.

84. Plaxco, K. W., Simons, K. T., and Baker, D. (1998) Contact order, transition state placement and the refolding rates of single domain proteins, *J Mol Biol 277*, 985-994.

85. Plaxco, K. W., Simons, K. T., Ruczinski, I., and Baker, D. (2000) Topology, Stability, Sequence, and Length: Defining the Determinants of Two-State Protein Folding Kinetics, *Biochemistry 39*, 11177-11183.

86. Scalley, M. L., and Baker, D. (1997) Protein folding kinetics exhibit an Arrhenius temperature dependence when corrected for the temperature dependence of protein stability, *Proc Natl Acad Sci USA 94*, 10636-10640.

87. Eaton, W. A., Muñoz, V., Hagen, S. J., Jas, G. S., Lapidus, L. J., Henry, E. R., and Hofrichter, J. (2000) Fast kinetics and mechanisms in protein folding, *Annual review of biophysics and biomolecular structure 29*, 327-359.

88. Gruebele, M. (2002) Protein folding: the free energy surface, *Curr Opin Struct Biol 12*, 161-168.

89. Kubelka, J., Eaton, W. A., and Hofrichter, J. (2003) Experimental tests of villin subdomain folding simulations, *J Mol Biol 329*, 625-630.

90. Qiu, L., Pabit, S. A., Roitberg, A. E., and Hagen, S. J. (2002) Smaller and faster: the 20-residue Trp-cage protein folds in 4 micros, *J Am Chem Soc 124*, 12952-12953.

91. Yang, W. Y., and Gruebele, M. (2003) Folding at the speed limit, *Nature 423*, 193-197.

92. Knight, J. B., Vishwanath, A., Brody, J. P., and Austin, R. H. (1998) Hydrodynamic Focusing on a Silicon Chip: Mixing Nanoliters in Microseconds, *Phys Rev Lett 80*, 3863-3866.

93. Yi, Q., and Baker, D. (1996) Direct evidence for a two-state protein unfolding transition from hydrogen-deuterium exchange, mass spectrometry, and NMR, *Protein Sci 5*, 1060-1066.

94. Plaxco, K. W., Millett, I. S., Segel, D. J., Doniach, S., and Baker, D. (1999) Chain collapse can occur concomitantly with the rate-limiting step in protein folding, *Nat. Struct. Biol. 6*, 554-556.

95. Yi, Q., Scalley-Kim, M. L., Simons, K. T., Gladwin, S. T., and Baker, D. (1997) Characterization of the free energy spectrum of peptostreptococcal protein L, *Folding & design 2*, 271-280.

96. Gu, H., Yi, Q., Bray, S. T., Riddle, D. S., Shiau, A. K., and Baker, D. (1995) A phage display system for studying the sequence determinants of protein folding, *Protein Sci 4*, 1108-1117.

97. Singh, V. R., Kopka, M., Chen, Y., Wedemeyer, W. J., and Lapidus, L. J. (2007) Dynamic Similarity of the Unfolded States of Proteins L and G, *Biochemistry*.

98. Ratner, V., Kahana, E., Eichler, M., and Haas, E. (2002) A general strategy for site-specific double labeling of globular proteins for kinetic FRET studies, *Bioconjug Chem 13*, 1163-1170.

99. Jäger, M., Michalet, X., and Weiss, S. (2005) Protein-protein interactions as a tool for site-specific labeling of proteins, *Protein Sci 14*, 2059-2068.

100. O'Neill, J. W., Kim, D. E., Baker, D., and Zhang, K. Y. (2001) Structures of the B1 domain of protein L from Peptostreptococcus magnus with a tyrosine to tryptophan substitution, *Acta Crystallogr D Biol Crystallogr 57*, 480-487.

101. Berman, H. M., Westbrook, J., Feng, Z., Gilliland, G., Bhat, T. N., Weissig, H., Shindyalov, I. N., and Bourne, P. E. (2000) The Protein Data Bank, *Nucleic Acids Res 28*, 235-242.

102. Nettels, D., Gopich, I. V., Hoffmann, A., and Schuler, B. (2007) Ultrafast dynamics of protein collapse from single-molecule photon statistics, *Proc Natl Acad Sci USA 104*, 2655-2660.

103. Sadqi, M., Lapidus, L. J., and Muñoz, V. (2003) How fast is protein hydrophobic collapse?, *Proc Natl Acad Sci USA 100*, 12117-12122.

104. Ma, H., and Gruebele, M. (2005) Kinetics are probe-dependent during downhill folding of an engineered lambda6-85 protein, *Proc Natl Acad Sci USA 102*, 2283-2287.

105. Creighton, T. E. (1992) *Protein folding*, W.H. Freeman and Co., New York.

106. Naganathan, A. N., Doshi, U., and Muñoz, V. (2007) Protein folding kinetics: barrier effects in chemical and thermal denaturation experiments, *J Am Chem Soc 129*, 5673-5682.

107. Zwanzig, R. (1988) Diffusion in a rough potential, *Proc Natl Acad Sci USA 85*, 2029-2030.

108. Wikstrom, M., Drakenberg, T., Forsen, S., Sjobring, U., and Bjorck, L. (1994) Three-dimensional solution structure of an immunoglobulin light chain-binding domain of protein L. Comparison with the IgG-binding domains of protein G, *Biochemistry 33*, 14011-14017.

109. Sherman, E., and Haran, G. (2006) Coil-globule transition in the denatured state of a small protein, *Proc Natl Acad Sci USA 103*, 11539-11543.

110. Merchant, K. A., Best, R. B., Louis, J. M., Gopich, I. V., and Eaton, W. A. (2007) Characterizing the unfolded states of proteins using single-molecule FRET spectroscopy and molecular simulations, *Proc Natl Acad Sci USA 104*, 1528-1533.